Design and Analysis of a Shock Absorber with a Variable Moment of Inertia Flywheel for Passive Vehicle Suspension

A thesis submitted to
the Faculty of Graduate and Postdoctoral Studies
in partial fulfillment of the requirements for the
degree of Master of Applied Science in
Mechanical Engineering

by
Tongyi Xu

Ottawa-Carleton Institute for Mechanical and Aerospace Engineering
University of Ottawa
Ottawa, Ontario, Canada, K1N 6N5
August 2013

Abstract

Conventional vehicle suspensions consist of a spring and a damper, while mass is rarely used. A mass, if properly used, can also create a damping-like effect. However, a mass has only one terminal which makes it difficult to be incorporated into a suspension. In order to use a mass to achieve the damping-like effect, a two-terminal mass (TTM) has to be designed. However, most of the reported TTMs are of fixed moment of inertia (TTM-CMI), which limits the further improvement of the suspension performance and responsiveness to changes in environment and driving conditions.

In this study, a TTM-based vibration absorber with variable moment of inertia (TTM-VMI) is proposed. The main component of the proposed TTM absorber contains a hydraulic-driven flywheel with sliders. The moment of inertia changes with the positions of the sliders in response to the driving conditions. The performance of the proposed TTM-VMI absorber has been analyzed via dynamics modeling and simulation and further examined by experiments. The analysis results indicate that the TTM-VMI absorber outperforms the TTM-CMI design in terms of body displacement; and ride comfort, tire grip and suspension deflection for zero and impulse inputs with comparable performance for sinusoidal input.

Acknowledgements

I would like to express my very great appreciation to Dr. M. Liang, my research supervisor for his valuable suggestions and patient guidance during this research work. I would also like to thank Dr. C. Li for providing me with the prototype and for machining some crucial parts for this research.

My grateful thanks are also extended to other graduate students in my laboratory for their good suggestions and great help in the area I am not familiar with, to the technicians working at the machine shop at the University of Ottawa, and to Professor John Hayes and Mr. Steve Truttmann of Carleton University for kindly arranging the tests and the detailed training.

Table of Content

List of Figures

List of Tables

Nomenclature

A	Cross-sectional area of the cylinder
A_{su}	Base area of the support
A_{tr}	Base area of the sliders
a_e	Transport acceleration
a_r	Relative acceleration
a_c	Coriolis acceleration
a_{et}	Tangential acceleration of transport acceleration
a_{rt}	Tangential acceleration of relative acceleration
a_x	Tangential acceleration of absolute acceleration
a_{en}	Normal acceleration of transport acceleration
a_{rn}	Normal acceleration of relative acceleration
a_w	Weighted root mean square (r.m.s.) acceleration
a_y	Normal acceleration of absolute acceleration
b	Inertance
C	Capacitance
CMI	Constant moment of inerita
c	Damping coefficient
c_1	Damping coefficient of the tire
c_2	Damping coefficient of the suspension
c_s	Damping coefficient of the hydraulic system
D_w	Suspension deflection for VMI suspension
d	Diameter of the sliders

d_p	Distance between the mass center of the tracks and the rotation center of the flywheel
F	Force
F_1	Force on terminal one
F_2	Force on terminal two
F_l	Force loss
F_p	Pressure between the sliders and the track
f	Friction between the sliders and tracks
f_p	Friction of the piston
$G_q(n_0)$	Road roughness parameter
H	Height of the VMI flywheel
$\|H(s)\|_2$	H_2-norm of $H(s)$
h	Height of the sliders
I	Current
J	Moment of inertia
J_c	Ideal moment of inertia of the flywheel excluding the sliders
J_d	Moment of inertia of the support without the tracks
J_f	Actual moment of inertia of the VMI flywhee
J_s	Moment of inertia of the sliders
J_{fmin}	Minimum moment of inertia of the VMI flywheel
J_{fmax}	Maximum moment of inertia of the VMI flywheel
J_{su}	Moment of inertia of the support
J_{tr}	Moment of inertia of four tracks
k	stiffness
k_1	Stiffness of the tire
k_2	Stiffness of the suspension

k_e	Stiffness of the hydraulic system
k_s	Stiffness of the springs connecting the sliders
L	Inductance
M_1	Ride comfort criterion
M_2	Road handling and safety (tire grip) criterion
M_3	Suspension deflection criterion
M_c	Mass of the flywheel without the sliders
M_s	Total mass of the sliders
M_{op1}	Optimal ride comfort criterion
M_{op2}	Optimal road handling and safety (tire grip) criterion
M_{op3}	Optimal suspension deflection criterion
m	Mass
m_1	Unsprung mass
m_2	Vehicle body mass
m_f	Mass of the CMI flywheel
m_p	Mass of the piston
m_s	Mass of the sliders
m_{su}	Mass of the support
m_{ri}	Mass of the flywheel ring
m_{tr}	Mass of the tracks
N	Number of the sliders
n	Displacement of the hydraulic motor
p	Pressure acting on the piston
p_l	Pressure loss
Q	Total flow rate from one chamber to another chamber
R	Resistance
r	Radius of the flywheel

r_i	Inner radius of the VMI flywheel ring
r_o	Outer radius of the VMI flywheel ring
r.m.s.	Root mean square
S	Relative displacement between two terminals
$\dot{S}$	Relative velocity between two terminals
$\ddot{S}$	Relative acceleration between two terminals
S_{sum}	Sum of the elastic displacement
T	Torque of the motor
t	Time
TT	Two-terminal
TTM	Two-terminal mass
VMI	Variable moment of inertia
V	Voltage
V_{su}	Volume of the support
V_{wa}	Weighted r.m.s. acceleration vector
$V_{w\eta}$	Weighted road handling index vector
V_{wD}	Weighted suspension deflection vector
v	Velocity
v_r	Relative velocity
$X(s)$	Input of a system
x_1	Displacement of the vehicle body
$\dot{x}_1$	Velocity of the vehicle body
$\ddot{x}_1$	Acceleration of the vehicle body
x_2	Displacement of the unsprung mass
$\dot{x}_2$	Velocity of the unsprung mass

$\ddot{x}_2$	Acceleration of the unsprung mass
x_e	Elastic displacement of the hydraulic system
x_g	Displacement excitation from the road
x_n	Actual displacement between two terminals
$\dot{x}_n$	Actual velocity between two terminals
$Y(s)$	Output of a system
$Z(s)$	Impedance of a network
α	Mass amplification coefficient
θ	Angular displacement of the flywheel
$\dot{\theta}$	Angular velocity of the flywheel
$\ddot{\theta}$	Angular acceleration of the flywheel
ζ	Damping ratio
ζ_{op1}	Optimal damping ratio for ride comfort
ζ_{op2}	Optimal damping ratio for tire grip
ζ_{op3}	Optimal damping ratio for suspension deflection
ω	Angular velocity of the flywheel
η_m	Mechanical efficiency of the hydraulic system
η_v	Volumetric efficiency of the hydraulic system
η_{RS}	Road handling index for VMI suspension
η_w	Weighted road handling index
μ	Friction coefficient between the sliders and the guide tracks
ρ	Density of the flywheel material
γ	Distance between the sliders and rotational center of the flywheel
$\dot{\gamma}$	Velocity of the sliders
$\ddot{\gamma}$	Acceleration of the sliders

γ_0	Original distance between the sliders and rotational center of the flywheel
^	Laplace transform
*	Complex conjugation

Chapter 1.Introduction

1.1 Background

Vehicle suspension is a system composed of springs, shock absorbers (dampers) and linkages that connect a vehicle to its wheels and allows relative motion between the two. Suspension systems serve a dual purpose — contributing to the vehicle's road holding, handling and braking for good active safety and driving pleasure, and keeping vehicle occupants comfortable and reasonably well isolated from road noise, bumps, and vibrations, etc.

Vehicle suspension can be looked as a mechanical network which is only composed of spring, damper and mass. All three elements have two terminals in mechanical networks, but one terminal of the mass is the ground and another terminal is the position of the center of mass itself because Newton’s Second Law relates the acceleration of the mass relative to a fixed point in the inertial frame, which is an important restriction for making use of mass in suspensions and vibration absorbers.

When a wheel of the vehicle hits a bump which compresses the suspension, this part of vibration energy generated by hitting the bump is stored in the suspension. After the bump, the stored energy needs to flow back. As a result, if the vehicle is not equipped with a shock absorber, the suspension would continue to go up and down after hitting the bump. In other words, this part of energy leads to vehicle oscillation which is obviously undesirable. The shock absorber dissipates or absorbs the energy generated by the vehicle oscillation and prevents the suspension from oscillating for a prolonged time.

Most of the existing shock absorbers are of hydraulic type dampers which damp the oscillations by dissipating the vibration energy into heat. Hence, the energy is wasted. As such, this study is directed towards the development of a new mass-based shock absorber to suppress the oscillation without energy waste and in the meantime improves the suspension performance.

1.2 Objective

The study aims to design a passive two-terminal (TT) variable moment of inertia (VMI) hydraulic-flywheel system which can be used in a conventional vehicle suspension to improve its performance, namely less displacement, faster response and less vehicle body oscillations. To achieve this objective, the following will be carried out:

1. *Design of the TT-VMI hydraulic-flywheel system*. This involves:
    a) Structural design, and
    b) Dynamics modeling.

2. *Simulation analysis*. The simulation is done by embedding the TT-VMI system into a traditional two-degree-of-freedom vehicle suspension model and comparing it with a two-terminal constant moment of inertia (CMI) hydraulic-flywheel model in terms of
    a) Vehicle body displacement,
    b) Response time to input vibrations, and
    c) Force transmitted to vehicle body.

    The comparisons are conducted for different input excitations and different masses of the vehicle body. These properties are important for a suspension because they are

related to comfort level and handling.

3. *Experimental tests*. As it is impossible to perform two-degree-of-freedom tests due to the limited experimental facilities, one-degree-of-freedom tests of the TT-VMI hydraulic-flywheel system is conducted on a MTS 810 test machine. More specifically, the tasks include:
   a) Examining the performance of the system under different excitation conditions,
   b) Comparing the force responses of the prototype with the flywheel configurations, i.e. maximum moment of inertia, minimum moment of inertia and variable moment of inertia.
   c) Testing the angular displacement of the flywheel by a tachometer, and
   d) Calculating the actual displacement of the flywheel and then compare it to ideal one.

1.3 Contribution of the Study

The main contribution of this study is the design, modeling and testing of a TT-VMI flywheel to be used in a shock absorber. The main component of the proposed TTM is a hydraulic-driven flywheel with sliders. The variable moment of inertia of the system is achieved by motion of the sliders embedded in the hydraulic driven flywheel. The moment of inertia of the flywheel changes with the positions of the sliders in response to the vehicle driving conditions. The flywheel is designed in such a way that, the moment of inertia increases in reaction to strong vertical vehicle oscillations (in terms of frequency and displacement), and decreases in the case of weak vertical oscillations. The hydraulic mechanism in the system converts the relative linear motion between the two terminals of suspension into the rotating motion of the flywheel. In the case of stronger

vehicle vertical oscillation, the sliders inside the flywheel move away from the center of the flywheel because of the centrifugal force, hence yielding higher moment of inertia. The opposite is true in the case of weaker vehicle oscillation. As such, the moment of inertia adjusts itself automatically in response to the road conditions. This is the main contribution of this study. In addition, the proposed VMI system has the following advantages as compared to its CMI counterpart:

1. Faster response,
2. Better road handling and safety, and
3. Improved ride comfort and reduced suspension deflection except in the case of sinusoidal excitations.

Chapter 2. Literature Review

2.1. Review of Electrical and Mechanical Passive Network Synthesis

Passive network synthesis is a classical subject in electrical circuit theory. It was developing rapidly from the 1930s to the 1960s (Chen and Smith 2008). Brune (1931) found the condition that was necessary and sufficient for a rational function to be an impedance function for a circuit includes inductors (including ideal transformers), capacitors and resistors. He showed that a circuit with a rational positive real function can be realized as the input impedance. Then a realization of a positive real function as the impedance of a circuit including only resistors, capacitors and inductors was found (Wing Omar 2008). This is the brief history of electrical network synthesis.

2.1.1. Electrical and Mechanical Passive Network

An electrical network is passive if a network has the following properties (Anderson and Vongpanitlerd 1973):

(1) The energy delivered to the network is non-negative for any arbitrary excitation, and

(2) No voltages or currents appear between any two terminals before an excitation is applied.

A network is defined to be passive if it cannot supply energy to the environment (Willem 2010). If a one-port (one-terminal) mechanical network has an impedance $Z(s)$ which is real-rational, it is passive if and only if $Z(s)$ is analytic and $Z(s)+Z(s)^* \geqslant 0$ in $\mathrm{Re}(s) > 0$, where * denotes complex conjugation (Smith and Wang 2004).

2.2.2. Analogy between Mechanical and Electrical Systems

If a group of physical concepts or quantities are related to each other following a similar rule or have equations similar to another group of concepts or quantities, then an analogy

might exist between these two groups (Firestone 1933). Obviously, an analogy exists between mechanical system and electrical system because of the similarities between them in terms of action and relevance principles.

The first analogy used between mechanical and electrical systems is the force-voltage analogy, which can be found in the early electromotive force analysis. In this analogy, the spring, damper and mass in mechanical system are compared to the capacitor, resistor and inductor in electrical system respectively. Firestone (1933) developed the force-current analogy between mechanical and electrical systems. In this analogy, the spring, damper and mass in a mechanical system corresponded to the inductor, resistor and capacitor in an electrical system respectively. Table 1 shows the circuit symbols and correspondences with defining equations of force-voltage analogy and the circuit symbols and correspondences of equations with defining equations of force-current analogy are shown in Table 2.2.

In fact, there is a mass restriction in both force-voltage and force-current analogy since one terminal of the mass is its mass center and another terminal must be the ground (the velocity of the ground is zero). The details of the mass restriction and a new two-terminal mass system developed for solving this restriction will be discussed next.

Table 2.1. Circuit symbols and correspondences with defining equations of force-voltage analogy (Brune 1931)

Electrical System	**Mechanical System**
Current (I)	Velocity (v)
Voltage (V)	Force (F)
Electrical ground (The voltage of the ground=0)	Mechanical ground (The velocity of the ground=0)
Inductor 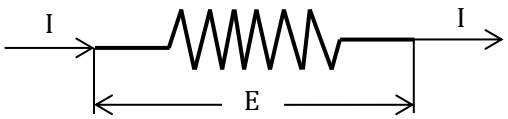 $E = L\frac{dI}{dt}$	Mass 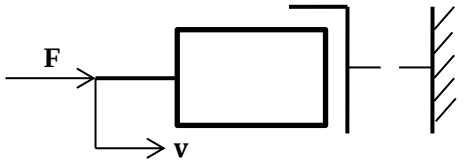 $F = m\frac{dv}{dt}$
Capacitor 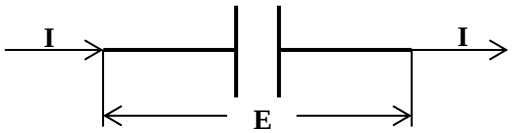 $E = \frac{1}{C}\int Idt$	Spring 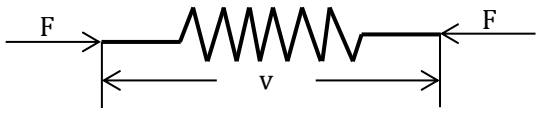 $F = k\int vdt$
Resistor 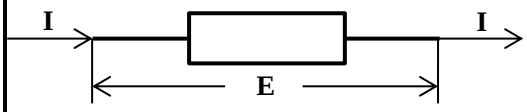 $E = RI$	Damper 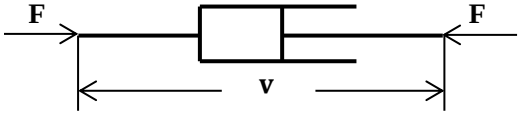 $F = cv$
Electrical energy $\frac{1}{2}CE^2$	Potential energy $\frac{1}{2}\frac{1}{k}F^2$
Magnetic energy $\frac{1}{2}LI^2$	Kinetic energy $\frac{1}{2}mv^2$

Table 2.2. Circuit symbols and correspondences with defining equations of force-current analogy (Firestone 1933)

Electrical System	**Mechanical System Ⅱ**
Current (I)	Force (F)
Voltage (E)	Velocity (v)
Electrical ground (The voltage of the ground=0)	Mechanical ground (The velocity of the ground=0)
Inductor  $\frac{dI}{dt}=\frac{1}{L}(V_1-V_2)$	Spring  $\frac{dF}{dt}=k(v_1-v_2)$
Capacitor 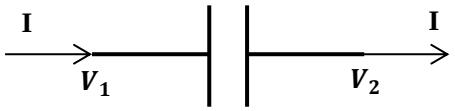 $I=C\frac{d(V_1-V_2)}{dt}$	Mass 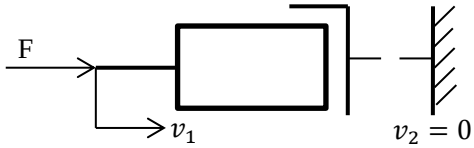 $F=m\frac{d(v_1-v_2)}{dt}$
Resistor 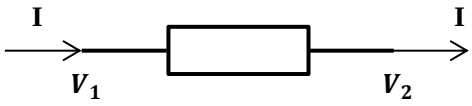 $I=\frac{1}{R}(V_1-V_2)$	Damper 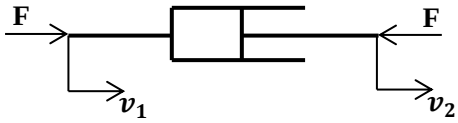 $F=c(v_1-v_2)$
Electrical energy (in capacitor) $\frac{1}{2}C(V_1-V_2)^2$	Kinetic energy (in mass) $\frac{1}{2}m(v_1-v_2)^2$
Magnetic energy (in inductor) $\frac{1}{2}LI^2$	Potential energy (in spring) $\frac{1}{2}\frac{1}{k}F^2$

2.2. Review of the Two-terminal Mass System

As described in section 2.1, the first analogy used between mechanical and electrical systems was the force-voltage analogy, which can be seen in the early electromotive force analysis. Firestone (1933) developed a new analogy between mechanical and electrical systems, which is known as force-current analogy. In this analogy, the spring, damper and mass corresponded to the inductor, resistor and capacitor respectively. However, there were some problems in this correspondence which are solved perfectly by two-terminal mass system.

2.2.1. Two-terminal Mass System

The force-current analogy works well in the case of spring and damper, but the restriction for mass cannot be ignored based on the Newton's Second Law because the acceleration of the mass is relative to a fixed point in the inertial frame (Smith 2002). More precisely, the typical mass has only one genuine terminal and another terminal is the position of the center of mass. Mass interacts the position and force with the environment through this ground terminal (Li *et al* 2010). The problem is that an electrical circuit may have a direct spring–mass-damper mechanical analog only if one terminal of the capacitor in this electrical circuit is grounded (Smith 2002).

Another drawback of the mass element as the analog of the capacitor is the mechanical impedances of the system. It may be important to assume that the mechanical device associated with the "black-box impedance" has negligible mass compared to other masses in the system. For example, a suspension strut for a vehicle compares to the sprung and unsprung masses. Obviously, this is a non-negligible problem if large masses are required for its realization (Smith 2002). A new two-terminal mass device-the inerter is invented and developed for solving the above problems (Smith 2002).

2.2.1.1. The Inerter

Smith (2002) defines the (ideal) inerter as a mechanical two-node (two-terminal), one-port device with the property that the equal and opposite forces applied at the nodes are proportional to the relative acceleration between the nodes. Namely, $F = b(\ddot{x}_1 - \ddot{x}_2)$, where *b* is called the inertance and has unit of kilogram. A free-body diagram of the inerter is shown in Figure 2.1. The stored energy in the inerter is equal to $\frac{1}{2}b(\ddot{x}_1 - \ddot{x}_2)^2$ (Smith 2002).

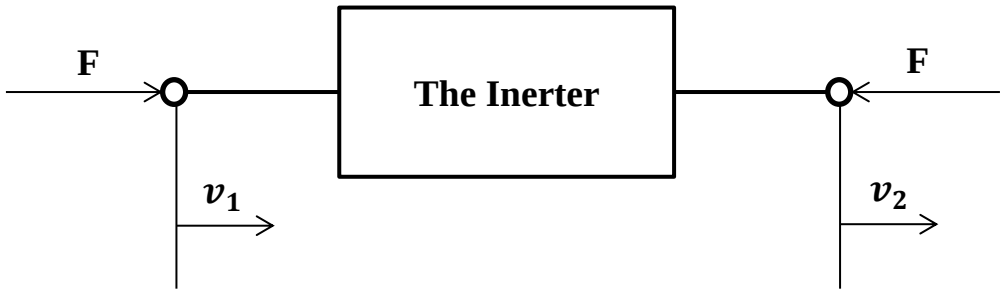

Figure 2.1. A free-body diagram of a one-port (two-terminal) inerter

The properties of the inerter are as follows：

1. It can be used as mass in mechanical networks, which has two manipulation terminals like spring and damper. Hence the mass can be used for parallel connection instead of series connection only in a vibration system.
2. The capacitor without the ground terminal in the electrical circuit can have a direct mechanical analogy by releasing the ground terminal of the mass (Li *et al* 2010).
3. It can realize very large inertial mass if the inertance α is big enough even if the real (gravitational) mass of the system is small. For example, 400-time virtual (inertial) mass was realized in a single-degree-of-freedom vibration isolation system (Zhu *et al* 2006); the inertial mass up to 1000 times of a flywheel's gravitational mass was achieved in a hydraulic two-terminal mass system (Li *et al* 2011).

The elementary diagram of the two-terminal mass is shown in Figure 2.2. It has two

manipulation terminals like spring and damper do.

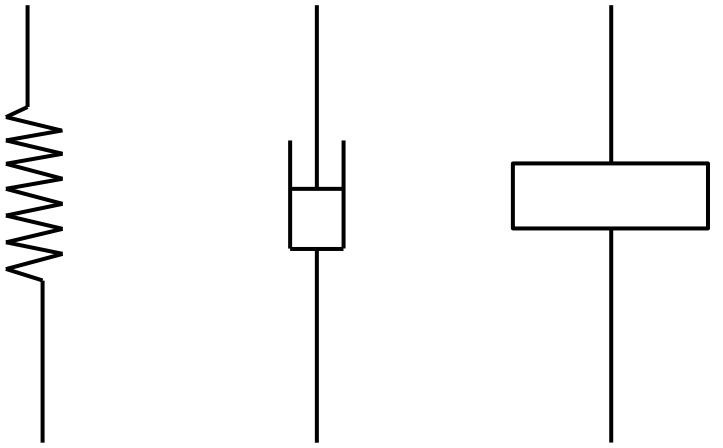

Figure 2.2. The elementary diagram of spring, damper and two-terminal mass

2.2.1.2. Different Two-terminal Mass Systems

Different kinds of two-terminal mass systems can be created based on different mass core and transmission combinations (Li *et al* 2010) which are shown in Table 2.3.

Table 2.3. Typical mass core transmissions for two-terminal mass systems

Relative motion of external terminals	Mass core	Motion transformation	Transmission mechanism
Rectilinear motion	Mass block	Rectilinear-Rectilinear	Lever
Rectilinear motion	Mass block	Rectilinear-Rectilinear	Hydraulic
Rotary motion	Mass block	Rotary-Rectilinear	Screw
Rotary motion	Mass block	Rotary-Rectilinear	Gear-Rack
Rectilinear motion	Flywheel	Rectilinear- Rotary	Hydraulic
Rectilinear motion	Flywheel	Rectilinear- Rotary	Rack-Gear
Rotary motion	Flywheel	Rotary- Rotary	Gear
Rotary motion	Flywheel	Rotary- Rotary	Hydraulic

For example, Figure 2.3 shows a two-terminal mass system with a combination of the flywheel and screw transmission (Li *et al* 2010). A two-terminal mass system, i.e., an inerter with combination of a rack and a gear transmission (Smith and Wang 2004) is shown in Figure 2.4. Li and Liang (2011) developed a two-terminal electro-hydraulic variable mass system, a combination of flywheel and hydraulic transmission as displayed in Figure 2.5.

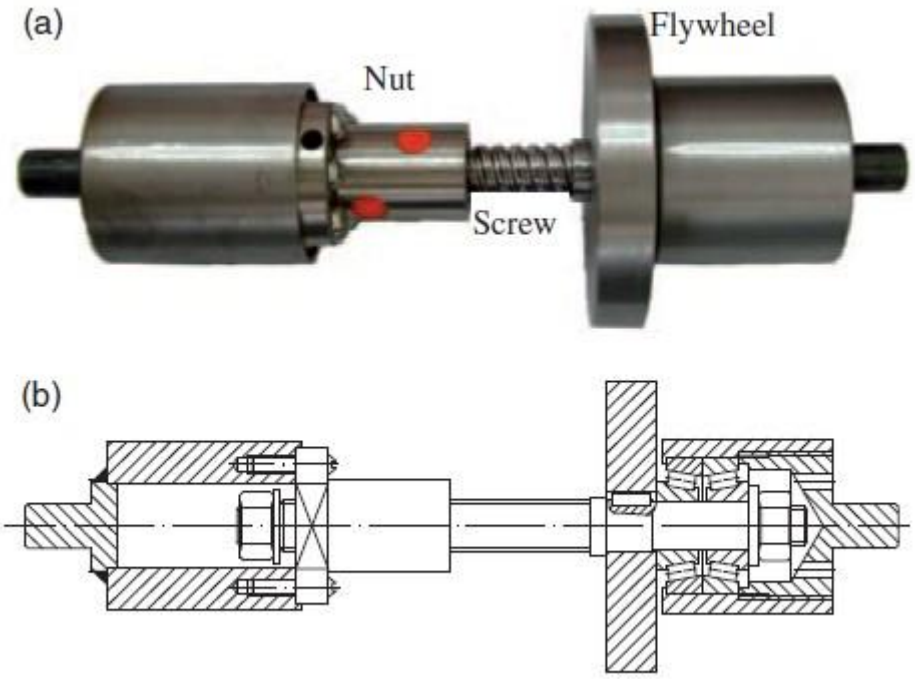

Figure 2.3. Prototype device of a two-terminal mass system developed by Li et al (2010): (a) Picture of the prototype, and (b) Structure schematic diagram of the prototype

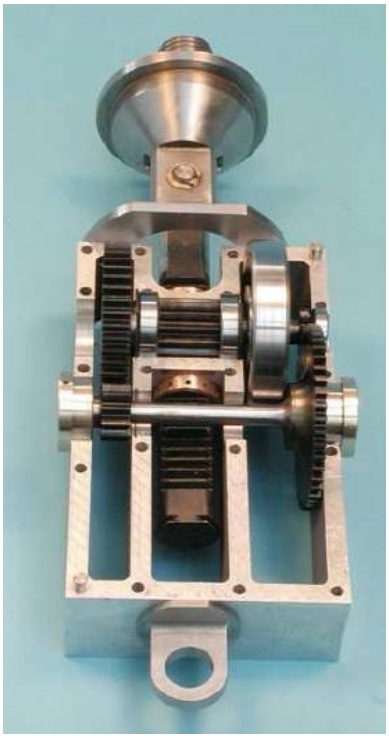

(a)

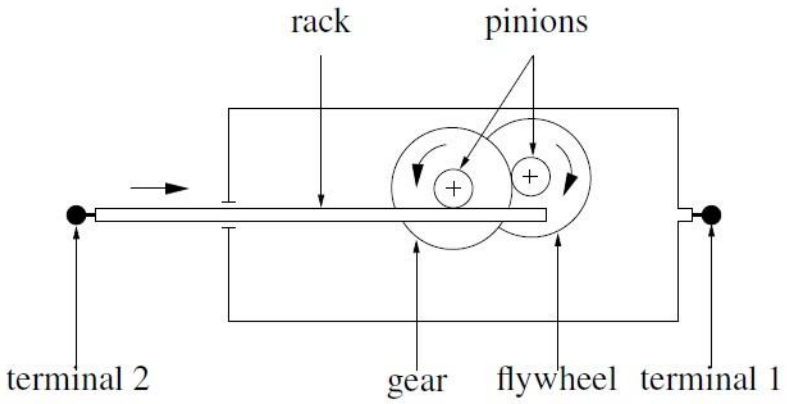

(b)

Figure 2.4. Prototype device of a two-terminal mass system developed by Smith and Wang (2004): (a) Picture of the prototype inerter, and (b) Schematic of the mechanical model of the prototype inerter

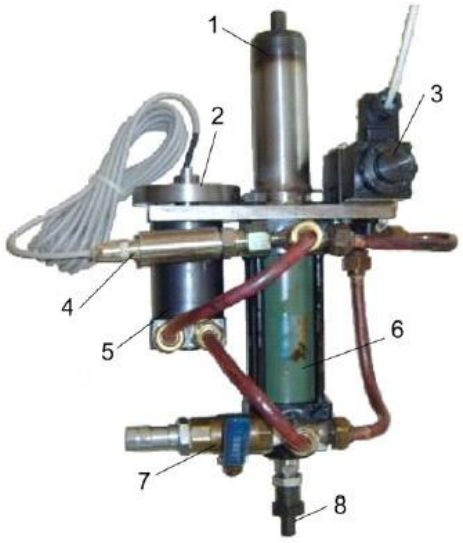

(a) 1—terminal 1, 2—flywheel, 3—electro-hydraulic proportional valve, 4—pressure transducer, 5—hydraulic motor, 6—hydraulic cylinder, 7—release valve, 8—terminal 2 (rod).

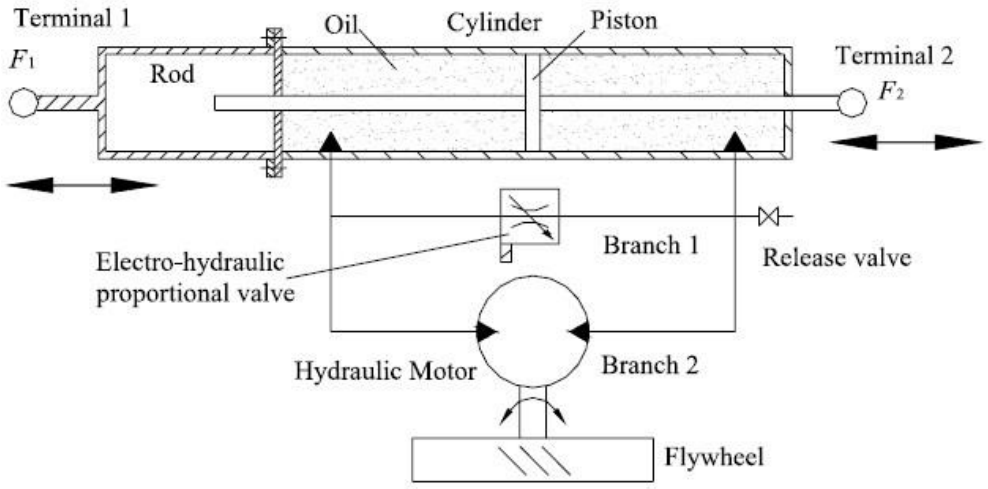

(b)

Figure 2.5. Prototype device of a two-terminal electro-hydraulic system developed by Li and Liang (2011): (a) Picture of the prototype, and (b) Schematic diagram of the electro-hydraulic variable two-terminal mass

2.2.2. Two-terminal Mass System Used for Vibration Absorption and Vehicle

Suspension

Though active or semi-active suspensions may perform better in terms of vibration absorption, passive suspensions still have the largest market share because of their acceptable performance, lower cost and simple strut structure (Yim *et al.*, 2010).

The main advantage of using a two-terminal mass system in a passive vehicle suspension is that it contributes to vibration absorption without consuming energy (Zuo 2012).

The conventional vehicle suspensions shown in Figure 2.6(a) have only two elements, i.e., a spring and a damper. Now, the new two-terminal mass system shown in Figure 2.6(b) is used into the vehicle suspension.

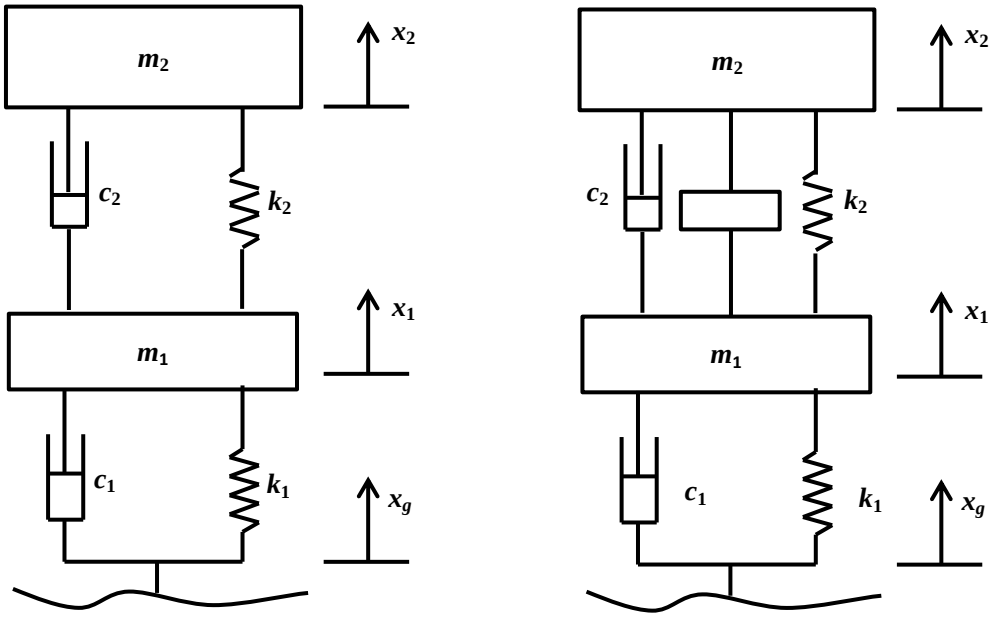

Figure 2.6. A passive two-degree-of-freedom vehicle suspension model: (a) Conventional passive vehicle suspension model, and (b) The same passive vehicle suspension model with a two-terminal mass system

Many other kinds of configurations of vehicle struts are proposed by Smith and Wang (2004) which are shown in Figure 2.7. All the parameters (stiffness of the springs, damping ratio of the dampers and the inertance of the two-terminal mass) can be changed in different cases. Each of the configurations in Figure 2.7 has its own merits. Some of them have better performance when used for heavy vehicles while some are more suited to lighter vehicles. Some of them perform better with stiffer tires while some may perform better for less stiff tires.

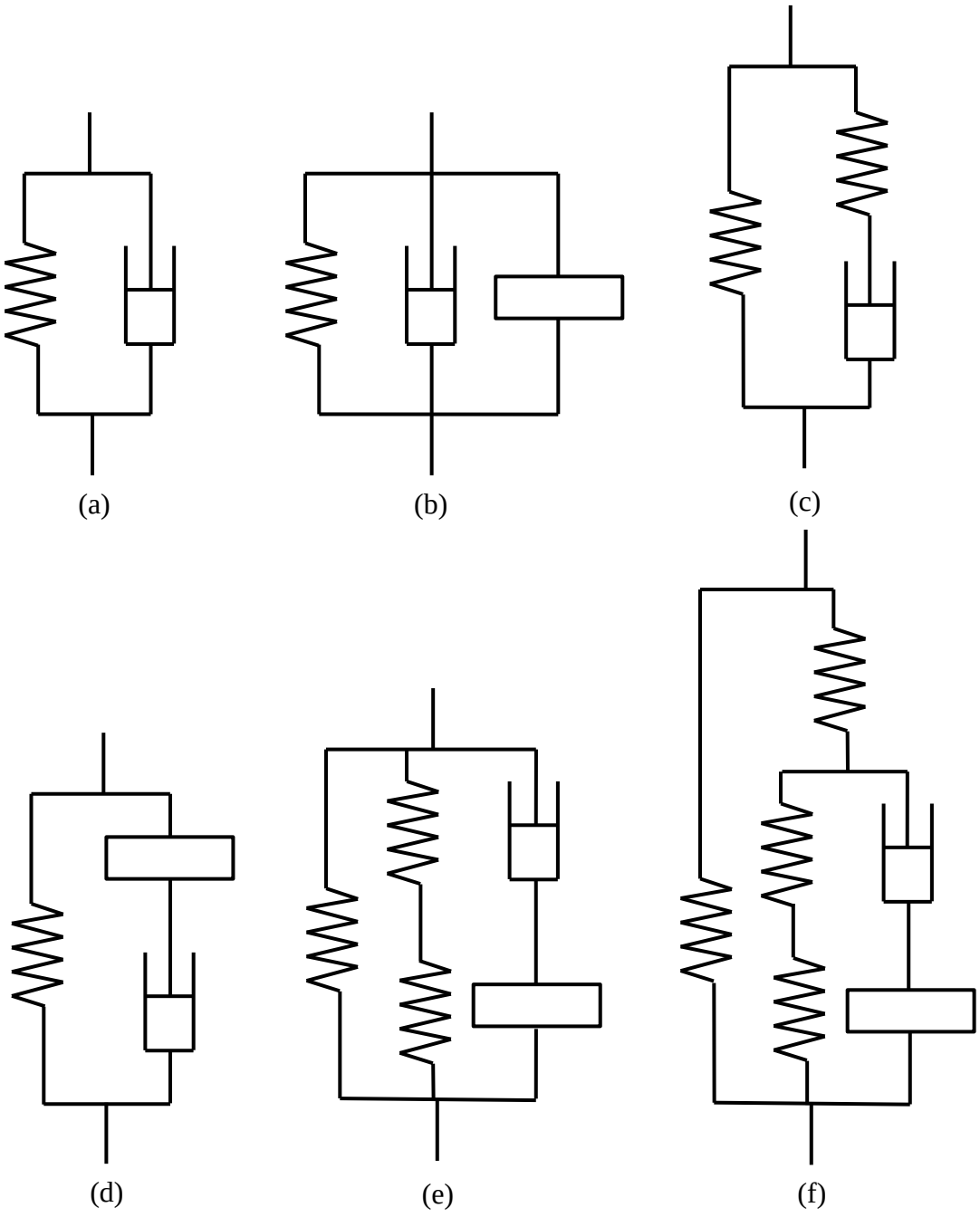

Figure 2.7. Six kinds of layouts of the vehicle suspension struts ((a) is the conventional vehicle suspension strut)

When a two-terminal mass system with combination of the flywheel and screw

transmission shown in Figure 2.3 is connected to the conventional vehicle suspension strut as Figure 2.7(b), it performs better than the conventional vehicle suspension in terms of passenger comfort, tire grip and suspension deflection (Li *et al* 2011).

Based on extensive experiments, it was concluded that the two-terminal mass system has many applications and provides better control performance in vibration systems (Li *et al* 2010).

The details about how the two-terminal mass system works for vibration absorption and vehicle suspension will be discussed in Chapter 3.

2.3. Review of Conventional Suspensions

A conventional suspension plus vehicle body and chassis (unsprung mass) include three different elements, i.e., mass, spring and damper, which constitute a mechanical network.

2.3.1. Conventional suspension model

The quarter-car model of a conventional two-degree-of-freedom vehicle suspension model is shown in Figure 2.6 (a). The force analysis is shown in Figure 2.8.

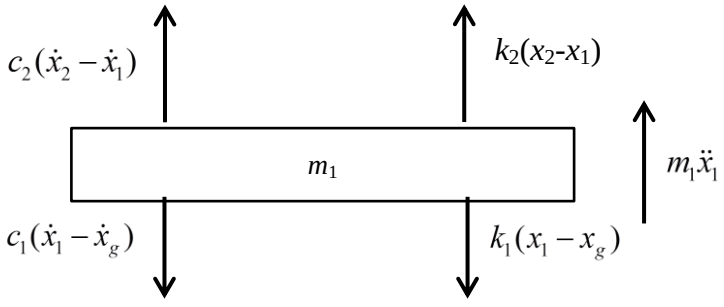

(a)

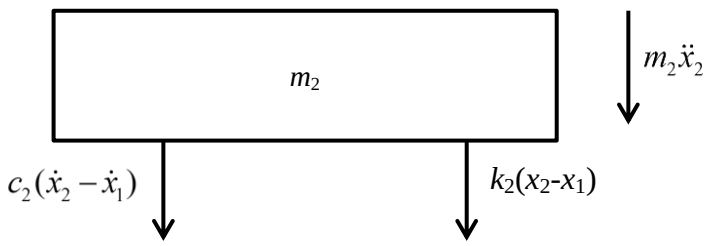

(b)

Figure 2.8. The force analysis of conventional suspension

The equations of motion are given by

$$\begin{cases} m_1\ddot{x}_1 + c_1(\dot{x}_1 - \dot{x}_g) + c_2(\dot{x}_1 - \dot{x}_2) + k_1(x_1 - x_g) + k_2(x_1 - x_2) = 0 \\ m_2\ddot{x}_2 + c_2(\dot{x}_2 - \dot{x}_1) + k_2(x_2 - x_1) = 0 \end{cases} \tag{2.1}$$

or

$$\begin{bmatrix} m_1 & 0 \\ 0 & m_2 \end{bmatrix}\begin{bmatrix} \ddot{x}_1 \\ \ddot{x}_2 \end{bmatrix} + \begin{bmatrix} c_1 + c_2 & -c_2 \\ -c_2 & c_2 \end{bmatrix}\begin{bmatrix} \dot{x}_1 \\ \dot{x}_2 \end{bmatrix} + \begin{bmatrix} k_1 + k_2 & -k_2 \\ -k_2 & k_2 \end{bmatrix}\begin{bmatrix} x_1 \\ x_2 \end{bmatrix} = \begin{bmatrix} k_1 x_g + c_1 \dot{x}_g \\ 0 \end{bmatrix} \tag{2.2}$$

where x_1 and x_2 are deflections measured from the undisturbed state, c_1 and c_2 are the viscous damping coefficients, k_1 and k_2 are the stiffness of the springs. In many publications, for example (Kuznetsov *et al* 2011), the tire of the wheel is considered as a structure with no damping properties, i.e. c_1=0. Then, Equation (2.1) becomes

$$\begin{cases} m_1\ddot{x}_1 + c_2(\dot{x}_1 - \dot{x}_2) + k_1(x_1 - x_g) + k_2(x_1 - x_2) = 0 \\ m_2\ddot{x}_2 + c_2(\dot{x}_2 - \dot{x}_1) + k_2(x_2 - x_1) = 0 \end{cases} \tag{2.3}$$

The Laplace Transform of Equation (2.3) can be written as

$$\begin{cases} s^2 m_1\hat{x}_1 + sc_2(\hat{x}_1 - \hat{x}_2) + k_1(\hat{x}_1 - \hat{x}_g) + k_2(\hat{x}_1 - \hat{x}_2) = 0 \\ s^2 m_2\hat{x}_2 + sc_2(\hat{x}_2 - \hat{x}_1) + k_2(\hat{x}_2 - \hat{x}_1) = 0 \end{cases} \tag{2.4}$$

Therefore, one obtains

$$\begin{cases} s^2\hat{x}_2 + \dfrac{2\zeta\omega_2}{\alpha}s(\hat{x}_2 - \hat{x}_1) + \dfrac{\omega_2^2}{\alpha}(\hat{x}_2 - \hat{x}_1) + \omega_1^2(\hat{x}_1 - \hat{x}_g) = 0 \\ s^2\hat{x}_2 + 2\zeta\omega_2 s(\hat{x}_2 - \hat{x}_1) + \omega_2^2(\hat{x}_2 - \hat{x}_1) = 0 \end{cases} \tag{2.5}$$

where ' ^ ' represents the Laplace transform of the corresponding variables, $\alpha = \frac{m_1}{m_2}$, $\zeta = \frac{c_2}{2\sqrt{m_2 k_2}}$, $\omega_1 = \sqrt{\frac{k_1}{m_1}}$, and $\omega_2 = \sqrt{\frac{k_2}{m_2}}$.

2.3.2. Performance Criteria

The road disturbance is a white noise whose spectrum densities are expressed as (Hazra and Ghosh 2009).

$$G_q(f) = \frac{1}{v} G_q(n_0)(10n)^{-2} \tag{2.6}$$

where v is driving velocity of the vehicle, $G_q(n_0)$ is the road roughness parameter, $f = \frac{\omega}{2\pi}$ is the motion frequency, and $n = \frac{f}{v}$ is the wave number.

2.3.2.1. Ride Comfort

The passenger comfort related to the body vertical acceleration is defined as (Fleury and Mistrop 2006)

$$M_1 = \left(\frac{1}{2\pi}\int_{-\infty}^{\infty} \left|\frac{s^2 \hat{x}_2}{\hat{x}_0}\right|^2 G_q(f)\, d\omega\right)^{\frac{1}{2}} \tag{2.7}$$

Substituting $f = \frac{\omega}{2\pi}$ into $n = \frac{f}{v}$ leads to

$$n = \frac{\omega}{2\pi v}$$

Therefore

$$G_q(f) = \frac{1}{v} G_q(n_0)\left(\frac{\omega}{2\pi v}\right)^{-2} = G_q(n_0)\omega^{-2}(0.2\pi)^2 v \tag{2.8}$$

Substituting Equation (2.7) and $s=j\omega$ into M_1, where $j = \sqrt{-1}$, one has

$$M_1 = (\frac{1}{2\pi}\int_{-\infty}^{\infty}\left|\frac{-\omega^2\hat{x}_2}{\hat{x}_0}\right|^2 G_q(n_0)\omega^{-2}(0.2\pi)^2 v)^{\frac{1}{2}} \tag{2.9}$$

Taking the constants out of the integral yields

$$M_1 = [\frac{1}{2\pi}(0.2\pi)^2 G_q(n_0)v\int_{-\infty}^{\infty}\frac{\omega^2\hat{x}_2^2}{\hat{x}_0^2}d\omega]^{\frac{1}{2}} \tag{2.10}$$

Suppose

$$H_1(s) = \frac{s\hat{x}_2}{\hat{x}_0} \tag{2.11}$$

As we know the H_2-norm of $H_1(s)$ is

$$\|H_1(s)\|_2 = (\frac{1}{2\pi}\int_{-\infty}^{\infty}\left|\frac{s\hat{x}_2}{\hat{x}_0}\right|^2 d\omega)^{\frac{1}{2}} = (\frac{1}{2\pi}\int_{-\infty}^{\infty}\frac{\omega^2\hat{x}_2^2}{\hat{x}_0^2}d\omega)^{\frac{1}{2}} \tag{2.12}$$

The ride comfort expression can be recast by substituting Equation (2.11) into Equation (2.9) as

$$M_1 = 0.2\pi(G_q(n_0)v)^{\frac{1}{2}}\|H_1(s)\|_2 \tag{2.13}$$

where $H_1(s)$ can be obtained from Equation (2.4).

2.3.2.2. Tire Grip

The tire grip related to the gravity center of the unspung mass, which decides the road handling and safety, is defined as (Fleury and Mistrop 2006)

$$M_2 = (\frac{1}{2\pi}\int_{-\infty}^{\infty}\left|\frac{\hat{x}_1 - \hat{x}_g}{\hat{x}_{0^2}}\right|^2 G_q(f)d\omega)^{\frac{1}{2}} \tag{2.14}$$

Similar to the method used for ride comfort, suppose

$$H_2(s) = \frac{\hat{x}_1 - \hat{x}_g}{s\hat{x}_0} \tag{2.15}$$

then one obtains

$$M_2 = 0.2\pi (G_q(n_0)v)^{\frac{1}{2}} \left\| H_2(s) \right\|_2 \tag{2.16}$$

2.3.2.3. Suspension Deflection

The suspension deflection is related to the vehicle center of gravity which decides the suspension life. It is given by (Fleury and Mistrop 2006)

$$M_3 = (\frac{1}{2\pi} \int_{-\infty}^{\infty} \left| \frac{\hat{x}_2 - \hat{x}_1}{\hat{x}_0} \right|^2 G_q(f) d\omega)^{\frac{1}{2}} \tag{2.17}$$

Again, like the method used for ride comfort and tire grip. Suppose

$$H_3(s) = \frac{\hat{x}_2 - \hat{x}_1}{s\hat{x}_0} \tag{2.18}$$

The deflection criterion can be expressed as

$$M_3 = 0.2\pi (G_q(n_0)v)^{\frac{1}{2}} \left\| H_3(s) \right\|_2 \tag{2.19}$$

In many publications, for example (Li *et al* 2010) and (Smith and Wang 2004), these three criteria are used to measure the performance of the vehicle suspensions. The details of this method will be discussed in Chapter 3 for the two-terminal hydraulic-flywheel system used in a vehicle suspension.

2.4. Limitations of Previous Studies and Motivation of Proposed Study

For conventional vehicle suspensions and vibration system, the mass has only one terminal. In other words, one terminal is the gravity center of the mass and another terminal is the ground. Other limitations of the conventional suspension have already been discussed in subsection 2.2.1. Now, a new kind of passive suspensions using two-terminal mass system has been introduced and used in formula one racing car. This new system described in 2.2 also has some limitations as follows.

1. A flywheel has to be used in the system to restore a part of kinetic energy for controlling the force. Obviously, this system makes the vehicle suspension heavier than before. The performances of such suspensions deteriorate when the mass ratio between the mass of the suspension and the car body increases because the mass of suspension is assumed to be small and neglected in the design stage.

2. During the design of a vehicle suspension, some parameters such as the mass of the vehicle body and the tire stiffness are assumed to be constant. However, the mass of the vehicle body changes depending on the number of passengers or the cargo load. The stiffness of the tire also changes when, e.g., the ambient temperature changes.

3. Once such suspensions are put in use, their performance may not be up to the design specifications due to the changing environment and driving conditions.

The first limitation, i.e., the unwanted mass increase, cannot be resolved using the traditional solid disc-like flywheel. Hence this study proposes a flywheel design to obtain the same moment of inertia with less mass than the conventional flywheel.

To mitigate the difficulties caused by the second and third limitations, this research proposes a flywheel configuration with moment of inertia that is variable in response to environment and driving conditions. This is an inexpensive approach to maintain or improve suspension performance under variable conditions as compared with the active suspensions.

As such, the main focus of this thesis is on the design, analysis and testing of a two-terminal variable mass flywheel module for application in passive vehicle suspensions.

Chapter 3. Design of a Two-terminal Variable Moment of Inertia Hydraulic-flywheel Module for Passive Vehicle Suspensions

At the beginning of this chapter, the passive two-terminal constant moment of inertia hydraulic-flywheel vehicle suspension, which is called CMI suspension system in this thesis, will be discussed. Since this system is a linear system, the transfer function is used to analyze it and examine its performance in terms of the three criteria in ***frequency*** domain. The performance of this new kind of suspension is better than the conventional suspension, but as mentioned before, some limitations of this system remain to be addressed.

In this chapter, a new system, two-terminal variable moment of inertia hydraulic-flywheel system which will be called VMI system hereafter, is proposed to mitigate the limitation of two-terminal CMI system. Due to the non-linearity of the VMI system, it is difficult to analyze it using a system transfer function in the frequency domain. As such, a new method will be developed for system analysis and performance evaluation in the ***time*** domain for some excitation inputs of interest. The numerical solutions of the equations of motion will be obtained using MATLAB.

The application optimizations and performance comparisons between passive two-terminal hydraulic-flywheel suspension and two-terminal variable-mass hydraulic-flywheel suspension will be discussed in the last part of this chapter. The one-degree vibration system for experiment will also be discussed in this chapter.

3.1. Structure of Two-terminal CMI Hydraulic-flywheel System Used in Vehicle Suspension

As mentioned in Chapter 2, there are ten different kinds of typical mass core transmissions for two-terminal mass systems. In this thesis, the last one (i.e., the one whose relative motion of external terminals is “rotary motion”, mass core is “flywheel”, motion transformation is “rotary-rotary” and transmission mechanism is “hydraulic”) in Table 2.3 is selected. The reason is that the rotary relative motion of external terminals can save the space and the hydraulic transmission mechanism can support a heavy vehicle body. Its prototype shown in Figure 3.1 is provided by Dr. Chuan Li of the Chongqing Technology and Business University, China. The schematic diagram of the prototype is shown in Figure 2.5(b) without Branch 1 (Electro-hydraulic proportional valve and release valve). Table 3.1 shows the main constituent parts of the prototype device and Table 3.2 shows the technical specifications of the prototype. This information is provided by Dr. Chuan Li.

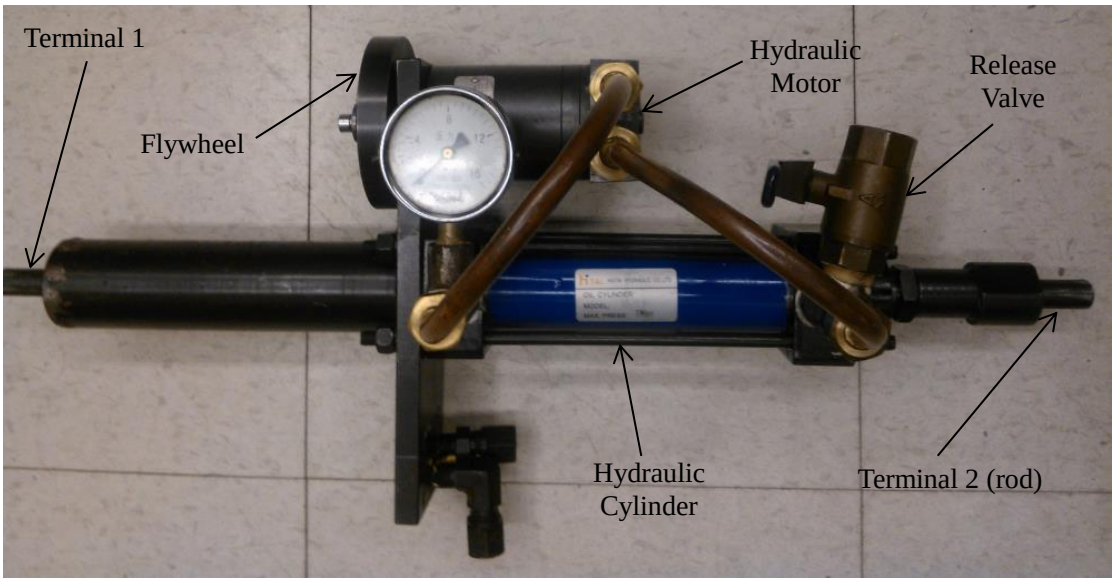

Figure 3.1. Prototype device of a two-terminal CMI Hydraulic-flywheel system

Table 3.1. List of the main components of the prototype

Name	Type	Manufacturer
Hydraulic cylinder	MOD 50×70	AHSHUN
Hydraulic motor	BMM8-MAE	ZY
Release valve	DN15	AMICO

Table 3.2. Technical specifications of the prototype device

Name	Notation	Specification
Cross-sectional area of the cylinder	A	$0.0012566 m^2$
Displacement of the motor	n	$1.30607 \times 10^{-6} m^3/rad$
Radius of the flywheel	r	0.045m
Gravitational mass of the flywheel	m	0.725kg
Travel of the rod		
Total mass of the device		
Inertance	b	679.5kg
Amplification coefficient	α	937.3

In the following derivations, A (in m^2) is defined as the cross-sectional area of the hydraulic cylinder, n (in m^3/rad) the displacement of the hydraulic motor, the $S=x_1-x_2$ the relative displacement caused by the external force $F=F_1-F_2$, between terminal 1 and 2. This relative displacement leads to the flywheel angular displacement θ given by

$$\theta = \frac{SA}{n} \tag{3.1}$$

Let $p=F/A$ represent the pressure acting on the piston, $Q = n\dot{\theta}$ the total flow rate from one chamber to another chamber, $T = n\dot{\theta}$ the torque of the motor and J the moment of inertia of the flywheel. As the flywheel is a cylindrical, its moment of inertia is

$$J = \frac{1}{2} mr^2 \tag{3.2}$$

where r is the radius of the flywheel and m is the gravitational mass.

Suppose there are no non-ideal factors, e.g., stiffness of the system is not infinity and the damping coefficient is not zero. The input power caused by F must be equal to the output power of the motor, then one obtains

$$pQ = T\dot{\theta} \tag{3.3}$$

From Equation (3.1), it is obvious that

$$\dot{\theta} = \frac{A}{n}\dot{S} \tag{3.4}$$

and

$$\ddot{\theta} = \frac{A}{n}\ddot{S} \tag{3.5}$$

Substituting p, Q, T and $\dot{\theta}$ into Equation (3.3) leads to

$$\frac{F}{A} \cdot n\dot{\theta} = J\ddot{\theta} \cdot \dot{\theta} \tag{3.6}$$

i.e.,

$$\frac{Fn}{A} = J\ddot{\theta} \tag{3.7}$$

Substitute Equations (3.2) and (3.5) into Equation (3.6) yields

$$\frac{Fn}{A} = \frac{1}{2} mr^2 \cdot \frac{A}{n}\ddot{S} \tag{3.8}$$

Therefore

$$F = m\frac{r^2 A^2}{2n^2}\ddot{S} \tag{3.9}$$

According to the Newton's Second Law, the acceleration a of a body is directly proportional to the net force F acting on the body, is in the direction of the net force, and is inversely proportional to the mass m of the body, i.e., $F=ma$. Hence the ratio $r^2A^2/2n^2$ in Equation (3.9) is a non-dimensional number which amplifies the gravitational mass of the flywheel. Based on Smith (2002), in which if the net force F is proportional to

acceleration a and a property b which has the unit of mass, b can be called "inertance", and hence $mr^2A^2/2n^2$ is inertance of the flywheel and is denoted as b.

From Table 3.2, the mass of the flywheel is 0.725kg, but the inertance is 679.5kg. It amplifies the mass of the flywheel about 900 times. The benefit is that the effect of a very large mass can be achieved using a small mass if the inertance b is big enough.

In fact, some non-ideal factors, which will be discussed in Section 3.3, also affect the performance of the prototype. They are as follows

1. The leakage between two chambers,
2. The dissipation of part of the energy generated by the motor due to the mechanical friction,
3. The compressible hydraulic oil, and
4. The limited stiffness (not infinity) of the rod.

Although this new two-terminal mass device has some non-ideal factors, it provides more important roles for masses and leads to better control performance in vibration systems as mentioned in Chapter 2.

3.2. Dynamic Model of the Two-terminal CMI Hydraulic-flywheel System

In this section, the mechanical characteristics of the two-terminal CMI hydraulic system are analyzed.

3.2.1. Governing Equation of the Cylinder

For the prototype shown in Figure 3.1, the inner leakage between two chambers can be neglected. The governing equation of the cylinder is then given by

$$F - f_p = Ap + m_p\ddot{s} \tag{3.10}$$

where A represents the piston area, p the pressure on the piston, m_p the mass of the piston, F the force between two terminals, f_p the friction of the piston, and s the relative displacement between two terminals as explained in Section 3.1.

3.2.2. Mechanical Analysis of the Hydraulic Motor

As mentioned in Section 3.1, the flow rate Q is the product of the flywheel angular velocity $\dot{\theta}$ and the displacement of the motor n. However, part of the energy or pressure is dissipated because of the friction. The relationship between the pressure loss p_l and the flow rate Q is given as

$$p_l = c_m Q \tag{3.11}$$

where c_m is a scale factor. In other word, the energy loss in this way is the same as that lost by a damper with a damping ratio $c_m A^2$ because substituting $Q = A\dot{x}_n$ into Equation (3.11) gives

$$p_1 = c_m A \dot{x}_n \tag{3.12}$$

Here, x_n is not the ideal relative displacement between two terminals (s) in Equation (3.1). The difference will be discussed next.

Therefore the reduced force due to pressure loss is

$$F_l = p_l A = c_m A^2 \dot{x}_n \tag{3.13}$$

Based on the energy conservation law, the input energy is equal to the output energy, i.e.

$$\eta_m (p - p_l) Q = T\dot{\theta} \tag{3.14}$$

where η_m<1 is the mechanical efficiency, and $T = J\ddot{\theta}$ the torque of the hydraulic motor as defined in Section 3.1.

In fact, the volumetric efficiency is less than one, i.e. η_v<1. It means that the inner leakage in the hydraulic motor is unavoidable. Then Equation (3.5) becomes

$$\ddot{\theta} = \eta_v \frac{A}{n} \ddot{x}_n \tag{3.15}$$

Considering Equations (3.10) to (3.13), Equation (3.9) becomes

$$F = m\frac{r^2 A^2 \eta_v}{2n^2 \eta_m}\ddot{x}_n + c_m AQ + f_p \tag{3.16}$$

3.2.3. Mechanical Model Formulation

Before the mechanical model is built, the stiffness of the system (the compressibility of the hydraulic oil and the elasticity of the rod) should be taken into consideration. In other words, the stiffness of the system is not infinity (ideal model). Assuming the stiffness of the system is k_e and the elastic displacement of the system is x_e, the elastic force of the system is given by

$$F = k_e x_e \tag{3.17}$$

The mechanical model of this system is shown in Figure 3.2(a) and the ideal model is shown in Figure 3.2(b).

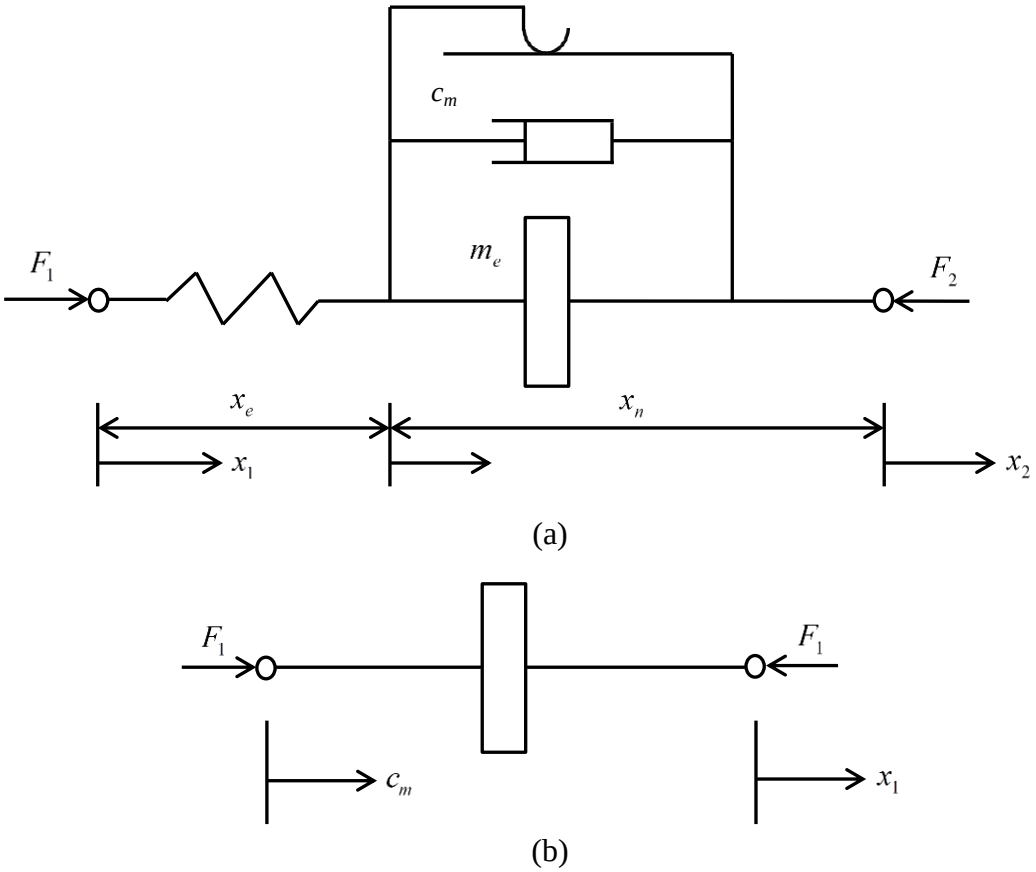

Figure 3.2. Mechanical model of the two-terminal constant-mass hydraulic-flywheel system: (a) actual model, and (b) ideal model

As mentioned above, the ideal relative displacement between two terminals (S) in Equation (3.1) (Here S is used to distinguish it from s in the Laplace transform) is the sum of the elastic displacement (x_e) and the displacement of the motor (x_n), i.e.

$$S_{sum} = x_e + x_n \tag{3.18}$$

According to the analyses above, the equations to illustrate the dynamic characteristics of the system can be written as

$$\begin{cases} F = k_e x_e \\ F = m_e \ddot{x}_n + c_m A^2 \dot{x}_n + f \\ S_{sum} = x_e + x_n \\ f = \left| f \right| \mathrm{sgn}(\dot{x}_n) \end{cases} \tag{3.19}$$

where $m_e = \dfrac{r^2 A^2 m \eta_v}{2n^2 \eta_m}$.

Equation (3.19) can be rewritten in Laplace's domain, i.e.

$$\hat{F} = k_e \hat{x}_e \tag{3.20}$$

$$\hat{F} = m_e \hat{x}_n s^2 + c_m A^2 \hat{x}_n s + \hat{f} \tag{3.21}$$

$$\hat{S}_{sum} = \hat{x}_e + \hat{x}_n \tag{3.22}$$

$$\hat{f} = \left| \hat{f} \right| \mathrm{sgn}(\hat{x}_n) \tag{3.23}$$

where ^ denotes the Laplace transform.

Suppose $X(s) = \hat{s}$ is the input and $Y(s) = \hat{F} - \hat{f}$ the output. Substituting Equation (3.22) into Equation (3.21) yields

$$\hat{F} = m_e (\hat{S}_{sum} - \hat{x}_e) s^2 + c_m A^2 (\hat{S}_{sum} - \hat{x}_e) s + \hat{f} \tag{3.24}$$

Substituting Equation (3.20) into Equation (3.24), one obtains

$$\hat{F} = m_e (\hat{S}_{sum} - \frac{\hat{F}}{k_e}) s^2 + c_m A^2 (\hat{S} - \frac{\hat{F}}{k_e}) s + \hat{f} \tag{3.25}$$

Equation (3.25) can be recast as

$$k_e(\hat{F}-\hat{f})(k_s+m_e s^2+c_m A^2 s)=m_e\hat{S}_{sum}s^2+c_m A^2\hat{S}_{sum}s-(m_e\frac{\hat{f}}{k_e}s^2+c_m A^2\frac{\hat{f}}{k_e}s) \quad (3.26)$$

Since the stiffness (k_e) is very large and the friction (f) is very small, i.e.

$$k_e \gg f \quad (3.27)$$

the last term of Equation (3.26) is negligible, i.e.,

$$m_e\frac{\hat{f}}{k_e}s^2+c_m A^2\frac{\hat{f}}{k_e}s\approx 0 \quad (3.28)$$

Therefore Equation (3.26) can be approximated as

$$\frac{1}{k_e}(\hat{F}-\hat{f})(k_e+m_e s^2+c_m A^2 s)=m_e\hat{S}s^2+c_m A^2\hat{S}s \quad (3.29)$$

The transfer function of the system is hence

$$\frac{Y(s)}{X(s)}=\frac{\hat{F}-\hat{f}}{\hat{S}}=\frac{k_e(m_e s^2+c_m A^2 s)}{k_e+m_e s^2+c_m A^2 s} \quad (3.30)$$

3.3. Passive Two-terminal VMI Hydraulic-flywheel System

In this thesis, a new two-terminal VMI hydraulic-flywheel system is designed using the prototype shown in Figure 3.1 as a platform. This design features a new flywheel with variable moment of inertia when it is rotating, which leads to the change of the inertance of the whole system, hence the name two-terminal variable moment of inertia (VMI) hydraulic-flywheel system. In this subsection, the details of this flywheel will be discussed.

The structure diagram of the flywheel is shown in Figure 3.3. In this diagram, only four sliders are in the flywheel. More sliders can be put into the flywheel if higher variable moment of inertia is needed. The changes of the moment of inertia of the flywheel is caused by position changes of the sliders while the flywheel is rotating (the effect of the changing length of the spring is ignorable).

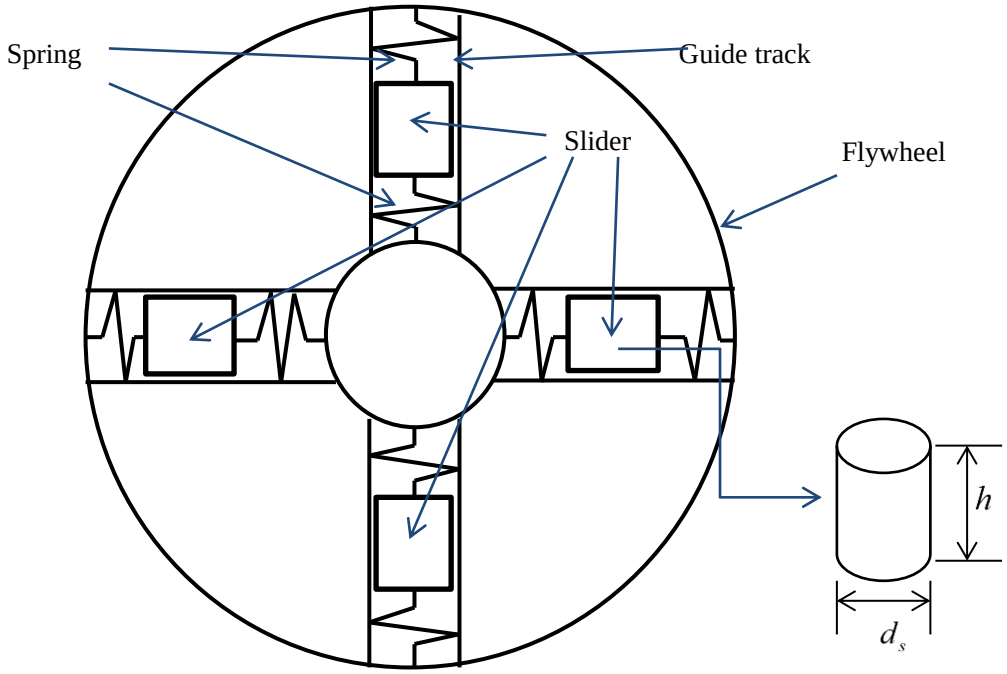

Figure 3.3. Structure diagram of the flywheel

The dynamics modeling of this VMI flywheel will be discussed next. When the flywheel is rotating at an angular velocity ω which is a function of time, the sliders will oscillate in the guide tracks, which are shown in Figure 3.4.

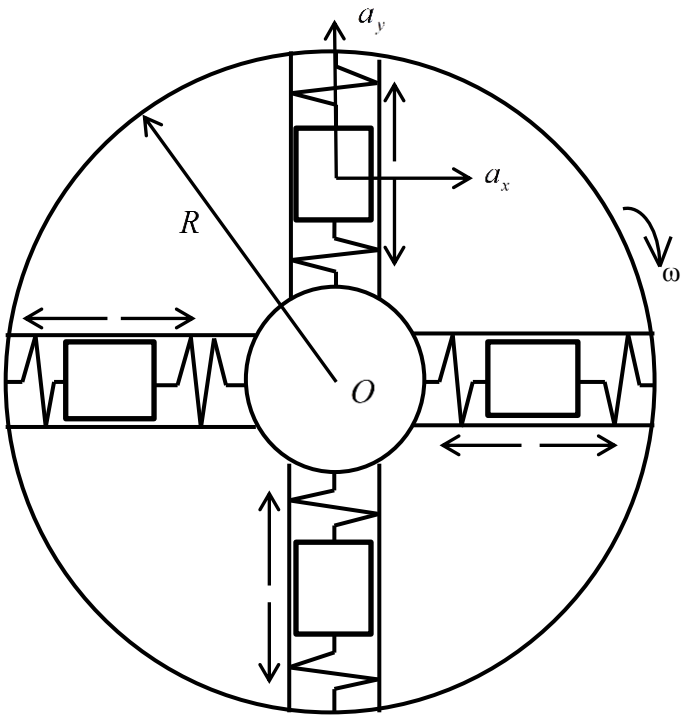

Figure 3.4. Structure diagram of the flywheel when it is rotating

The analysis of motion of the sliders is shown in Figure 3.5. The absolute acceleration is the vector sum of transport acceleration, relative acceleration and Coriolis acceleration, i.e.

$$a = a_e + a_r + a_c \tag{3.31}$$

where a represents the absolute acceleration of the sliders, a_e transport acceleration, a_r relative acceleration, and a_c Coriolis acceleration. Based on the geometric principle of the vector addition, the resultant acceleration can be divided into tangential acceleration and normal acceleration. In a Cartesian coordinate system, where tangential accelerations are in x axis direction and normal accelerations in the y axis direction, one has

$$a = a_x + a_y \tag{3.32}$$

$$a_e = a_{et} + a_{en} \tag{3.33}$$

$$a_r = a_{rt} + a_{rn} \tag{3.34}$$

Where a_x, a_{et}, a_{rt} are respectively the tangential acceleration of absolute acceleration, transport acceleration and relative acceleration and a_y, a_{en}, a_{rn} are their normal counterparts. Therefore

$$a_x + a_y = a_{et} + a_{en} + a_{rt} + a_{rn} + a_c \tag{3.35}$$

If the gaps between sliders and guide tracks are ignorable (a_{rt}=0), there will be no relative displacement between sliders and guide tracks in the x axis direction. If the friction between sliders and guide tracks are neglected (The modeling with frictions will be discussed in Section 3.3). Because there is no displacement in x axis between the sliders and the guide tracks, only accelerations in y axis are discussed in the following. The accelerations can be written as

$$\begin{cases} a_x = a_{et} + a_c \\ a_y = a_{en} + a_r \end{cases} \tag{3.36}$$

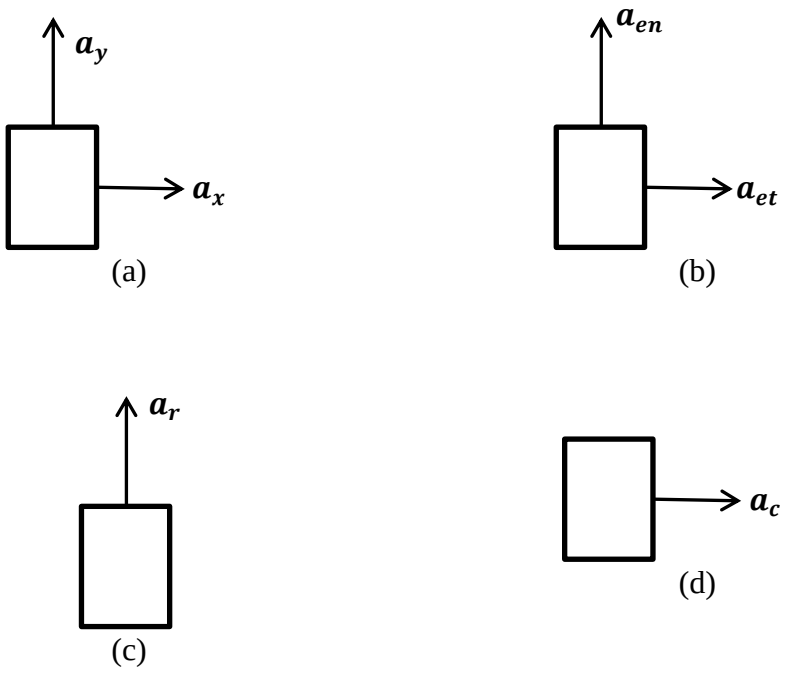

Figure 3.5. Analysis of slider motion: (a) absolute acceleration, (b) transport acceleration, (c) relative acceleration, and (d) Coriolis acceleration

The force analysis is based on Figure 3.6 where only part of the flywheel and one slider is shown. As mentioned above, the force analysis is carried out only for *y* direction because there is no acceleration in *x* direction. In Figure 3.6, *O* represents the rotational center of the flywheel, k_s the stiffness of the spring connecting the sliders, γ the distance between the sliders and the rotational center of the flywheel, γ_0 the distance between the sliders and the rotational center of the flywheel when it is static, m_s the mass of the sliders. Therefore

$$m_s a_y + k_s(\gamma - \gamma_0) = 0 \tag{3.37}$$

Substituting the *y* direction part of Equation (3.36) into Equation (3.37) leads to

$$m_s(a_{en} + a_r) + k_s(\gamma - \gamma_0) = 0 \tag{3.38}$$

Since

$$a_{en} = \gamma\omega^2 \tag{3.39}$$

$$a_r = \ddot{\gamma} \tag{3.40}$$

then one has

$$m_s(\gamma\omega^2 + \ddot{\gamma}) + k_s(\gamma - \gamma_0) = 0 \tag{3.41}$$

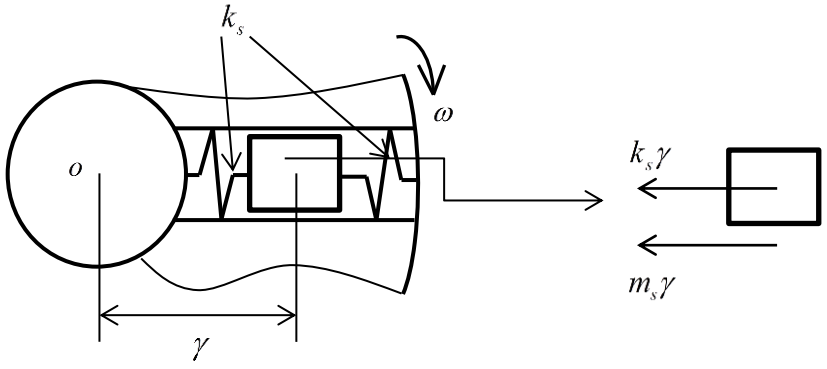

Figure 3.6. Force analysis of the flywheel

The moment of inertia of a cylinder rotating around *z* axis shown in Figure 3.7 (a) is

$$I_z = \frac{1}{12} m(\frac{3}{4} d^2 + h^2) \tag{3.42}$$

where d and h are the diameter and height of the cylinder respectively, m is the mass of the cylinder. According to Parallel Axis Theorem, the moment of inertia of a cylinder rotating around z' shown in Figure 3.7 (b) is

$$I_{z'} = \frac{1}{12} m(\frac{3}{4} d^2 + h^2) + ml^2 \tag{3.43}$$

where z axis and z' axis are parallel, l is the distance between z axis and z' axis.

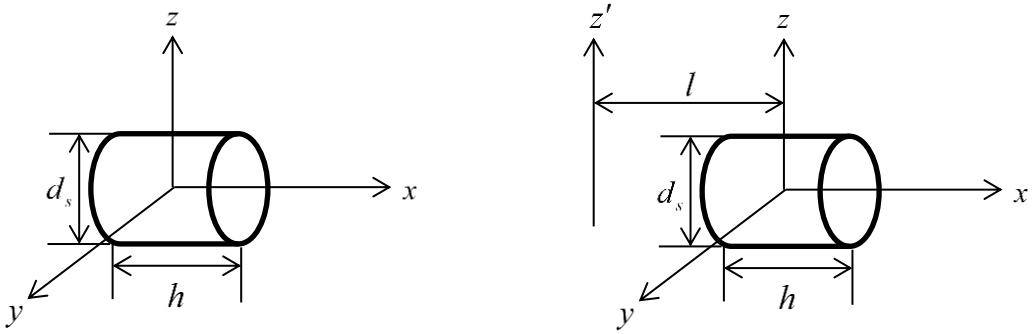

(a) (b)

Figure 3.7. Moment of inertia of a cylinder

Suppose the total mass of the sliders is

$$M_s = Nm_s \tag{3.44}$$

where N is the number of the sliders (here N=4). The moment of inertia of the sliders is

$$J_s = \frac{1}{12} M_s(\frac{3}{4} d_s^{\,2} + h^2) + M_s\gamma^2 \tag{3.45}$$

If the flywheel without the sliders is treated a cylinder, and the mass of the flywheel without the sliders is M_c, the moment of inertia of the flywheel (excluding the sliders) is given by

$$J_c = \frac{1}{2} M_c r^2 \tag{3.46}$$

where r is the radius of the flywheel. Then the total moment of inertia of the flywheel assembly is

$$J = J_s + J_c \tag{3.47}$$

i.e.,

$$J = \frac{1}{12} M_s (\frac{3}{4} d_s^2 + h^2) + M_s \gamma^2 + \frac{1}{2} M_c r^2 \tag{3.48}$$

Now, the conventional flywheel in the two-terminal hydraulic-flywheel system is replaced by this VMI flywheel, whose elementary diagram is shown in Figure 3.8 (a).

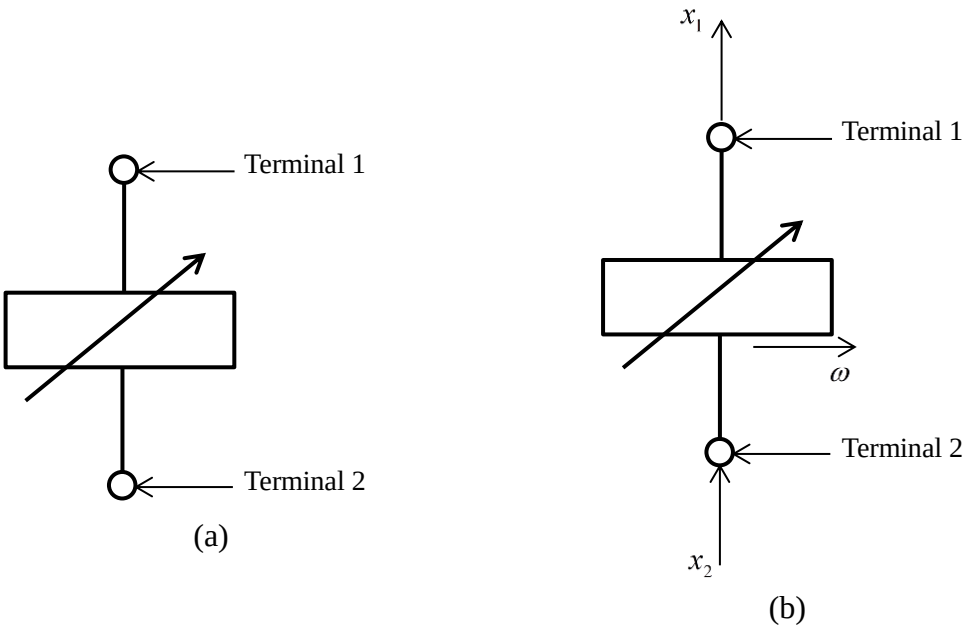

Figure 3.8. Elementary diagram and motion analysis of the two-terminal VMI hydraulic-flywheel systems: (a) elementary diagram of the two-terminal VMI hydraulic-flywheel system, and (b) motion analysis of the two-terminal VMI hydraulic-flywheel system.

The motion analysis is shown in Figure 3.8 (b), where x_1 represents the displacement of terminal 1, x_2 the displacement of terminal 2, ω the angular velocity of the flywheel. As it is known,

$$\omega = \dot{\theta} \tag{3.49}$$

where θ is the angular displacement of the flywheel. Substituting Equation (3.1) into Equation (3.28) yields

$$\omega = \frac{A}{n}(\dot{x}_1 - \dot{x}_2) \tag{3.50}$$

Equations (3.41), (3.48) and (3.50) are the equations of motion of this system, i.e.

$$\begin{cases} m_s(\gamma\omega^2 + \ddot{\gamma}) + k_s(\gamma - \gamma_0) = 0 \\ J = \frac{1}{12}M_s(\frac{3}{4}d_s^2 + h^2) + M_s\gamma^2 + \frac{1}{2}M_c r^2 \\ \omega = \frac{A}{n}(\dot{x}_1 - \dot{x}_2) \end{cases} \tag{3.51}$$

Following the above analysis, a prototype VMI flywheel is designed and fabricated. The components and the assembled VMI flywheel are shown in Figure 4.9.

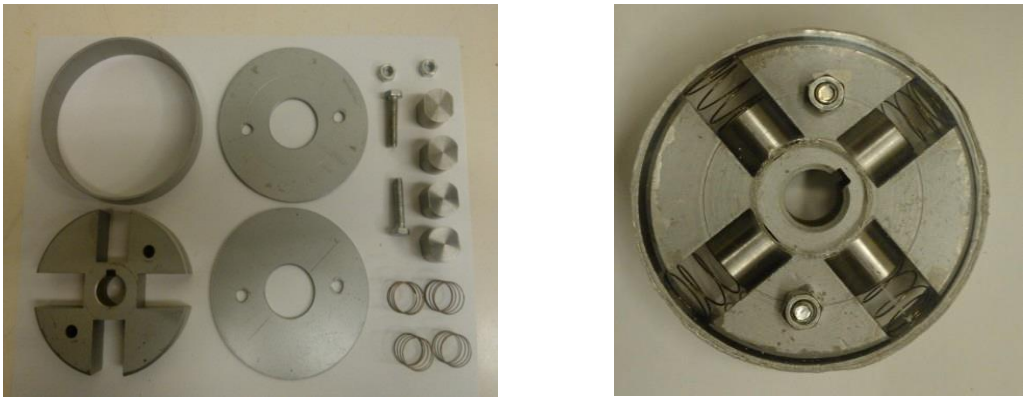

(a) (b)

Figure 3.9. VMI flywheel

3.4. Two-terminal Constant-mass Hydraulic-flywheel System Used in Vehicle Suspension

The two-terminal CMI hydraulic-flywheel system shown in Figure 3.1 will be discussed in this section in a vehicle suspension before describing the two-terminal VMI suspension system.

3.4.1. Equation of Motion

The methods for analysis are the same as the methods for conventional suspension mentioned in Chapter 2. The two-degree-of-freedom quarter-car model is shown in Figure 2.6 (b). Figure 3.10 shows the force analysis of the two-degree-of-freedom quarter-car model.

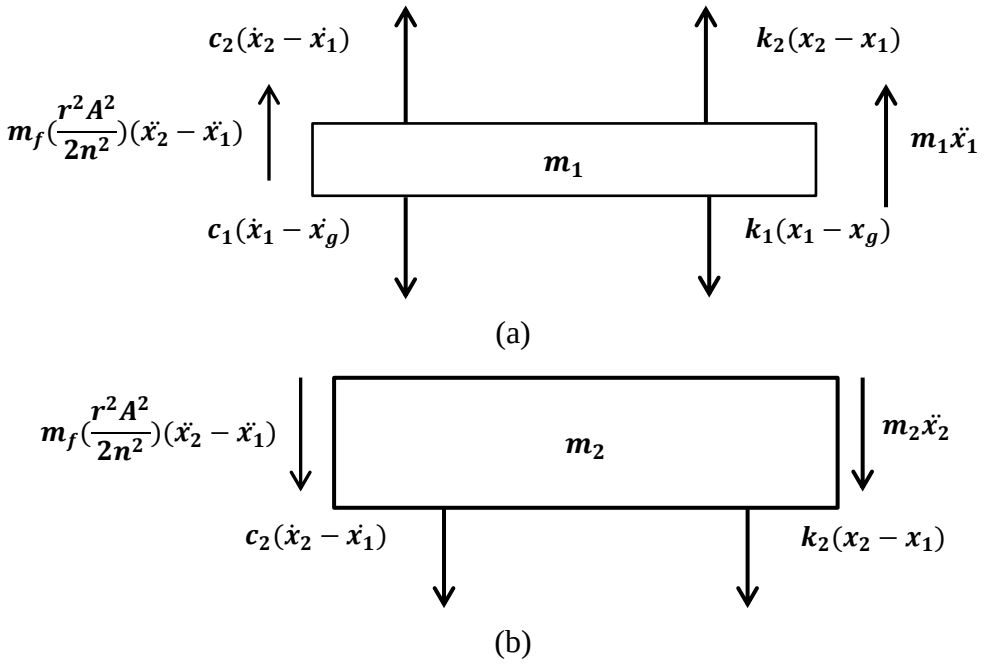

Figure 3.10. Force analysis of the vehicle suspension using a two-terminal constant-mass hydraulic-flywheel system, where mf represents the mass of the flywheel: (a) force analysis of the vehicle unsprung mass, and (b) force analysis of the vehicle body

The equations of motion are given by

$$\begin{cases} m_1\ddot{x}_1 + m_f\dfrac{r^2A^2}{2n^2}(\ddot{x}_1 - \ddot{x}_2) + (c_1 + c_2)\dot{x}_1 - c_2\dot{x}_2 + (k_1 + k_2)x_1 - k_2x_2 - k_1x_g - c_1x_g = 0 \\ m_2\ddot{x}_2 + m_f\dfrac{r^2A^2}{2n^2}(\ddot{x}_2 - \ddot{x}_1) - c_2\dot{x}_1 + c_2\dot{x}_2 - k_2x_1 + k_2x_2 = 0 \end{cases} \quad (3.52)$$

or

$$\begin{bmatrix} m_1 + m_f \dfrac{r^2A^2}{2n^2} & -m_f \dfrac{r^2A^2}{2n^2} \\ -m_f \dfrac{r^2A^2}{2n^2} & m_2 + m_f \dfrac{r^2A^2}{2n^2} \end{bmatrix} \begin{bmatrix} \ddot{x}_1 \\ \ddot{x}_2 \end{bmatrix} + \begin{bmatrix} c_1 + c_2 & -c_2 \\ -c_2 & c_2 \end{bmatrix} \begin{bmatrix} \dot{x}_1 \\ \dot{x}_2 \end{bmatrix} + \begin{bmatrix} k_1 + k_2 & -k_2 \\ -k_2 & k_2 \end{bmatrix} \begin{bmatrix} x_1 \\ x_2 \end{bmatrix} = \begin{bmatrix} k_1 x_g + c_1 \dot{x}_g \\ 0 \end{bmatrix} \tag{3.53}$$

As mentioned in Chapter 2, the damping of the tire of a wheel, c_1, is relatively small compared to other components in the quarter-car system. If c_1=0 as assumed in Li *et al* (2011) and Smith and Wang (2004), Equation (3.52) then becomes

$$\begin{cases} m_1 \ddot{x}_1 + m_f \dfrac{r^2A^2}{2n^2} (\ddot{x}_1 - \ddot{x}_2) + c_2 (\dot{x}_1 - \dot{x}_2) + (k_1 + k_2) x_1 - k_2 x_2 - k_1 x_g = 0 \\ m_2 \ddot{x}_2 + m_f \dfrac{r^2A^2}{2n^2} (\ddot{x}_2 - \ddot{x}_1) - c_2 \dot{x}_1 + c_2 \dot{x}_2 - k_2 x_1 + k_2 x_2 = 0 \end{cases} \tag{3.54}$$

Then the Laplace Transform of Equation (3.54) can be written as

$$\begin{cases} m_1 s^2 \hat{x}_1 + m_f \dfrac{r^2A^2}{2n^2} s^2 (\hat{x}_1 - \hat{x}_2) + c_2 s (\hat{x}_1 - \hat{x}_2) + k_1 (\hat{x}_1 - \hat{x}_g) + k_2 (\hat{x}_1 - \hat{x}_2) = 0 \\ m_2 s^2 \hat{x}_2 + m_f \dfrac{r^2A^2}{2n^2} s^2 (\hat{x}_2 - \hat{x}_1) - c_2 s (\hat{x}_1 - \hat{x}_2) - k_2 (\hat{x}_1 - \hat{x}_2) = 0 \end{cases} \tag{3.55}$$

The inertance is given by

$$b = m_f \frac{r^2A^2}{2n^2} \tag{3.56}$$

Substituting Equation (3.56) into Equation (3.55), then Equation (3.55) can be recast as

$$\begin{cases} m_1 s^2 \hat{x}_1 + b s^2 (\hat{x}_1 - \hat{x}_2) + c_2 s (\hat{x}_1 - \hat{x}_2) + k_1 (\hat{x}_1 - \hat{x}_g) + k_2 (\hat{x}_1 - \hat{x}_2) = 0 \\ m_2 s^2 \hat{x}_2 - b s^2 (\hat{x}_1 - \hat{x}_2) - c_2 s (\hat{x}_1 - \hat{x}_2) - k_2 (\hat{x}_1 - \hat{x}_2) = 0 \end{cases} \tag{3.57}$$

or

$$\begin{cases} s^2 \hat{x}_1 + \dfrac{b}{m_1} s^2 (\hat{x}_1 - \hat{x}_2) + \dfrac{c_2}{m_1} s (\hat{x}_1 - \hat{x}_2) + \dfrac{k_1}{m_1} (\hat{x}_1 - \hat{x}_g) + \dfrac{k_2}{m_1} (\hat{x}_1 - \hat{x}_2) = 0 \\ s^2 \hat{x}_2 - \dfrac{b}{m_2} s^2 (\hat{x}_1 - \hat{x}_2) - \dfrac{c_2}{m_2} s (\hat{x}_1 - \hat{x}_2) - \dfrac{k_2}{m_2} (\hat{x}_1 - \hat{x}_2) = 0 \end{cases} \tag{3.58}$$

Some variables are now introduced: tire natural frequency ω_1, body natural frequency ω_2, suspension damping ratio ζ, tire body mass ratio α and inertial mass ration β, i.e.

$$\begin{cases} \omega_1 = \sqrt{\dfrac{k_1}{m_1}} \\ \omega_2 = \sqrt{\dfrac{k_2}{m_2}} \\ \zeta = \dfrac{c_2}{2\sqrt{k_2 m_2}} \\ \alpha = \dfrac{m_1}{m_2} \\ \beta = \dfrac{b}{m_2} \end{cases} \tag{3.59}$$

Similar to Equation (2.4), incorporating Equation (3.59) into Equation (3.58) gives

$$\begin{cases} s^2\hat{x}_1 + \dfrac{\beta}{\alpha}s^2(\hat{x}_1 - \hat{x}_2) + \dfrac{2\zeta\omega_2}{\alpha}s(\hat{x}_1 - \hat{x}_2) + \omega_1^2(\hat{x}_1 - \hat{x}_g) + \dfrac{\omega_2^2}{\alpha}(\hat{x}_1 - \hat{x}_2) = 0 \\ s^2\hat{x}_2 - \beta s^2(\hat{x}_1 - \hat{x}_2) - 2\zeta\omega_2 s(\hat{x}_1 - \hat{x}_2) - \omega_2^2(\hat{x}_1 - \hat{x}_2) = 0 \end{cases} \tag{3.60}$$

where ‘ ^ ’ represents the Laplace transform of the corresponding variables.

3.4.2. Performance Criteria

The performance of a suspension system is evaluated based on a set of criteria. In this thesis, three of the most important criteria, i.e., ride comfort, road handling/safety (tire grip), and suspension deflection are considered. To facilitate discussions, some important methods for analysis of the suspension performance are reviewed for a passive two-terminal constant moment of inertia suspension in the following.

3.4.2.1. Ride Comfort

As mentioned in Chapter 2, the passenger comfort related to the body vertical acceleration is defined as (Li *et al* 2011)

$$M_1 = \left(\frac{1}{2\pi}\int_{-\infty}^{\infty}\left|\frac{s^2\hat{x}_2}{\hat{x}_0}\right|^2 G_q(f)d\omega\right)^{\frac{1}{2}} \tag{3.61}$$

After certain mathematic derivations, it can be written as

$$M_1 = 0.2\pi (G_q(n_0)v)^{\frac{1}{2}} \left\| H_1(s) \right\|_2 \tag{3.62}$$

where $H_1(s) = \dfrac{s\hat{x}_2}{\hat{x}_0}$.

The tire grip is expressed by

$$M_2 = (\frac{1}{2\pi}\int_{-\infty}^{\infty} \left| \frac{\hat{x}_1 - \hat{x}_g}{\hat{x}_{0^2}} \right|^2 G_q(f) d\omega)^{\frac{1}{2}} \tag{3.63}$$

which leads to

$$M_2 = 0.2\pi (G_q(n_0)v)^{\frac{1}{2}} \left\| H_2(s) \right\|_2 \tag{3.64}$$

where $H_2(s) = \dfrac{\hat{x}_1 - \hat{x}_g}{s\hat{x}_0}$.

The suspension deflection is described by

$$M_3 = (\frac{1}{2\pi}\int_{-\infty}^{\infty} \left| \frac{\hat{x}_2 - \hat{x}_1}{\hat{x}_0} \right|^2 G_q(f) d\omega)^{\frac{1}{2}} \tag{3.65}$$

or

$$M_3 = 0.2\pi (G_q(n_0)v)^{\frac{1}{2}} \left\| H_3(s) \right\|_2 \tag{3.66}$$

where $H_3(s) = \dfrac{\hat{x}_2 - \hat{x}_1}{s\hat{x}_0}$.

According to Li *et al* (2011), and Smith and Wang (2004), $H_1(s)$, $H_2(s)$ and $H_3(s)$ can be derived from Equation (3.60). $H_1(s)$ is given by

$$H_1(s) = \frac{s\omega_1^2(\beta s^2 + 2\zeta\omega_2 s + \omega_2^2)}{(\beta s^2 + 2\zeta\omega_2^2 + \omega_2^2)(s^2 + \omega_1^2) + s^2(s^2 + \dfrac{\beta}{\alpha}s^2 + \dfrac{2\zeta\omega_2}{\alpha}s + \dfrac{\omega_2^2}{\alpha} + \omega_1^2)} \tag{3.67}$$

It is known that

$$\left\| H_1(s) \right\|_2 = (\frac{1}{2\pi}\int_{-\infty}^{\infty} \left| H_1(j\omega) \right|^2 d\omega)^{\frac{1}{2}} \tag{3.68}$$

Substituting Equation (3.67) into Equation (3.68) with $s=j\omega$, one obtains (Li *et al* 2011)

$$\left\|H_1(s)\right\|_2 = (a_1\zeta + \frac{a_2\beta^3 + a_3\beta^2 + a_4\beta + a_5}{\zeta(a_6\beta) + a_7})^{\frac{1}{2}} \tag{3.69}$$

where

$$\begin{cases} a_1 = \alpha\omega_1^2\omega_2 \\ a_2 = \omega_1^4\alpha^2 \\ a_3 = \alpha^2\omega_1^4 - 2\alpha^2\omega_1^2\omega_2^2 - 2\alpha\omega_1^2\omega_2^2 \\ a_4 = \alpha^2\omega_2^4 - 2\alpha^2\omega_1^2\omega_2^2 + 2\alpha\omega_2^4 + \omega_2^4 \\ a_5 = \alpha^2\omega_2^4 + \alpha\omega_2^4 \\ a_6 = 4\alpha\omega_2 + \alpha\omega_2^4 \\ a_7 = 4\alpha\omega_2 \end{cases} \tag{3.70}$$

It is easy to verify that $\left\|H_1(s)\right\|_2$ is a concave function related to ζ. Therefore, the optimal damping ratio ζ_{op1} is what satisfies the equation below.

$$\frac{d\left\|H_1(s)\right\|_2}{d\zeta} = 0 \tag{3.71}$$

As a result,

$$\zeta_{op1} = (\frac{a_2\beta^3 + a_3\beta^2 + a_4\beta + a_5}{a_1a_7 + a_1a_6\beta})^{\frac{1}{2}} \tag{3.72}$$

$\left\|H_1(s)\right\|_2$ is also a concave function related to β, and hence the optimal inertial mass ratio β_{op1} can be obtain by

$$\frac{d\left\|H_1(s)\right\|_2}{d\beta} = 0 \tag{3.73}$$

i.e.,

$$\frac{d\left\|H_1(s)\right\|_2}{d\beta} = \frac{3a_2\beta^2 + 2a_3\beta + a_4}{\zeta(a_7 + a_6\beta)} - \frac{a_6(a_2\beta^3 + a_3\beta^2 + a_4\beta + a_5)}{\zeta(a_7 + a_6\beta)^2} = 0 \tag{3.74}$$

Equation (3.74) can be rewritten under the condition that $\zeta(a_7 + a_6\beta) \neq 0$. The reason is as follow:

If $\zeta(a_7+a_6\beta)=0$, one of ζ and $a_7+a_6\beta$ must be zero.

1. If ζ=0, then according to Equation (3.59) c_2=0 because $k_2 \neq 0$ and $m_2 \neq 0$. It means the system has no damping effect, which does not make sense.
2. According to the physical meanings of a_7, a_6 and β, they must be positive or zero. Hence $a_7+a_6\beta=0$ implies that a_7=0 and one of a_6 and β is also zero which further implies α=0 or ω_2=0 based on Equation (3.70). However $\alpha=m_1/m_2=0$ is equivalent to say m_1=0; then the system becomes a one-degree-of-freedom system, which is obviously not the case here. On other hand, if ω_2=0, then k_2 must be zero based on Equation (3.59). Again this is not true because the stiffness of the system is not zero.

The above confirms that the $\zeta(a_7 + a_6\beta) \neq 0$ condition assumed in Equation (3.74) is valid. Then Equation (3.74) leads to

$$2a_2a_6\beta^3 + (3a_2a_7 + a_3a_6)\beta^2 + 2a_3a_7\beta + a_4a_7 - a_5a_6 = 0 \tag{3.75}$$

Only one of three solutions of Equation (3.75) is real and positive. Based on Cardano's Formula, Equation (3.75) can be simplified

$$\beta^3 + \frac{3a_2a_7 + a_3a_6}{2a_2a_6}\beta^2 + \frac{a_3a_7}{a_2a_6}\beta + \frac{a_4a_7 - a_5a_6}{2a_2a_6} = 0 \tag{3.76}$$

Define

$$\begin{cases} k = \dfrac{3a_2a_7 + a_3a_6}{2a_2a_6} \\ m = \dfrac{a_3a_7}{a_2a_6} \\ n = \dfrac{a_4a_7 - a_5a_6}{2a_2a_6} \end{cases} \tag{3.77}$$

Then Equation (3.76) becomes

$$\beta^3 + k\beta^2 + m\beta + n = 0 \tag{3.78}$$

The solution process can be further simplified by defining

$$\beta = x - \frac{k}{3} \tag{3.79}$$

Hence Equation (3.78) can be recast as

$$x^3 + px + q = 0 \tag{3.80}$$

where

$$\begin{cases} p = -\dfrac{k^2}{3} + m \\ q = \dfrac{2k^3}{27} - \dfrac{km}{3} + n \end{cases} \tag{3.81}$$

Equation (3.80) has three solutions but only one of them is real and positive.

As an illustrative example, one can assume m_1=30kg, m_2=300kg, k_1=100000N/m and k_2=80000N/m for a typical vehicle suspension. Accordingly

$$\begin{cases} \alpha = \dfrac{m_1}{m_2} = 0.1 \\ \omega_1 = \sqrt{\dfrac{k_1}{m_1}} = \sqrt{\dfrac{100000}{30}} \\ \omega_2 = \sqrt{\dfrac{k_2}{m_2}} = \sqrt{\dfrac{80000}{300}} \end{cases} \tag{3.82}$$

According to Cardano's Formula, the discriminant of this cubic function is

$$\Delta = (\frac{q}{2})^2 + (\frac{p}{3})^3 > 0 \tag{3.83}$$

Therefore this cubic function has only one real root, i.e.

$$x = [-\frac{q}{2} + \sqrt{(\frac{q}{2})^2 + (\frac{p}{3})^3}]^{\frac{1}{3}} + [-\frac{q}{2} - \sqrt{(\frac{q}{2})^2 + (\frac{p}{3})^3}]^{\frac{1}{3}} \tag{3.84}$$

Consequently from Equation (3.79)

$$\beta_{op1} = x - \frac{k}{3} = [-\frac{q}{2} + \sqrt{(\frac{q}{2})^2 + (\frac{p}{3})^3}]^{\frac{1}{3}} + [-\frac{q}{2} - \sqrt{(\frac{q}{2})^2 + (\frac{p}{3})^3}]^{\frac{1}{3}} - \frac{k}{3} \tag{3.85}$$

Substituting Equation (3.72) and (3.85) into Equation (3.69), the 2-norm of $H_1(s)$ is

$$\|H_1(s)\|_2 = 64.84 \tag{3.86}$$

Therefore

$$M_{op1} = 0.2\pi (G_q(n_0)v)^{\frac{1}{2}} \|H_1(s)\|_2 = 0.2\pi (G_q(n_0)v)^{\frac{1}{2}} \times 64.84 \tag{3.87}$$

3.4.2.2. Road Handling and Safety (tire grip)

The road handling and safety performance can be examined based on Equation (3.60). According to (Li *et al* 2011) and (Smith and Wang 2004), H_2 in the road handling and safety criterion is expressed as

$$H_2(s)=\frac{\omega_1^2(s^2+\beta s^2+2\zeta\omega_2 s+\omega_2^2)}{s^3(s^2+\frac{\beta}{\alpha}s^2+\frac{2\zeta\omega_2}{\alpha}s+\frac{\omega_2^2}{\alpha}+\omega_1^2)+s(s^2+\omega_1^2)(\beta s^2+2\zeta\omega_2 s+\omega_2^2)}-1 \quad (3.88)$$

It is known that

$$\left\|H_2(s)\right\|_2=(\frac{1}{2\pi}\int_{-\infty}^{\infty}\left|H_2(j\omega)\right|^2 d\omega)^{\frac{1}{2}} \quad (3.89)$$

As $s=j\omega$, the above two equations lead to

$$\left\|H_2(s)\right\|_2=(b_1\zeta+\frac{b_2\beta^2+b_3\beta+b_4}{\zeta})^{\frac{1}{2}} \quad (3.90)$$

where

$$\begin{cases} b_1=\dfrac{\alpha^2\omega_2+2\alpha\omega_2+\omega_2}{\alpha\omega_1^2} \\ b_2=\dfrac{1+\alpha}{4\omega_2} \\ b_3=\dfrac{2\alpha^2\omega_1^2+\alpha\omega_1^2-2\alpha^2\omega_2^2-4\alpha\omega_2^2-2\omega_2^2}{4\alpha\omega_1^2\omega_2} \\ b_4=\dfrac{\alpha^3\omega_1^4-2\alpha^3\omega_1^2\omega_2^2-2\alpha^2\omega_1^2\omega_2^2+\alpha^3\omega_2^4+3\alpha^2\omega_2^4+3\alpha\omega_2^4+\omega_2^4}{4\alpha^2\omega_1^4\omega_2} \end{cases} \quad (3.91)$$

Like the method used in Section 3.4.2.1, the optimal damping ratio ζ_{op2} should satisfy

$$\frac{d\left\|H_2(s)\right\|_2}{d\zeta}=0 \quad (3.92)$$

Then one has

$$\zeta_{op2}=(\frac{b_2\beta^2+b_3\beta+b_4}{b_1})^{\frac{1}{2}} \quad (3.93)$$

Similarly, the optimal inertial mass ratio β can be obtained by

$$\frac{d\left\|H_2(s)\right\|_2}{d\beta}=0 \tag{3.94}$$

i.e.,

$$\frac{1}{2}(b_1\zeta+\frac{b_2\beta^2+b_3\beta+b_4}{\zeta})^{-\frac{1}{2}}\cdot\frac{2b_2\beta+b_3}{\zeta}=0 \tag{3.95}$$

It is clear that

$$(b_1\zeta+\frac{b_2\beta^2+b_3\beta+b_4}{\zeta})^{-\frac{1}{2}}\neq 0 \tag{3.96}$$

Therefore in Equation (3.95)

$$\frac{2b_2\beta+b_3}{\zeta}=0 \tag{3.97}$$

i.e.,

$$\beta_{op2}=-\frac{b_3}{2b_2} \tag{3.98}$$

By definition, β cannot be negative. Therefore

$$\beta_{op2}=\begin{cases}0, & b_3\geq 0\\ -\dfrac{b_3}{2b_2}, & b_3<0\end{cases} \tag{3.99}$$

Substituting Equations (3.99) and (3.93) into Equation (3.90), one obtains

$$\left\|H_2(s)\right\|_2=\begin{cases}(\dfrac{4b_1b_2b_4-b_1b_3^2}{b_2})^{\frac{1}{4}}, & b_3<0\\ (4b_1b_4)^{\frac{1}{4}}, & b_3\geq 0\end{cases} \tag{3.100}$$

Therefore from Equation (3.64)

$$M_{op2}=\begin{cases}0.2\pi(G_q(n_0)v)^{\frac{1}{2}}\cdot(\dfrac{4b_1b_2b_4-b_1b_3^2}{b_2})^{\frac{1}{4}}, & b_3<0\\ 0.2\pi(G_q(n_0)v)^{\frac{1}{2}}\cdot(4b_1b_4)^{\frac{1}{4}}, & b_3\geq 0\end{cases} \tag{3.101}$$

For illustration, if the parameters of the suspension expressed in Equation (3.82) are used, one has

$$\left\|H_2(s)\right\|_2 = 0.0487 \tag{3.102}$$

Hence

$$M_{op2} = 0.2\pi(G_q(n_0)v)^{\frac{1}{2}}\left\|H_2(s)\right\|_2 = 0.2\pi(G_q(n_0)v)^{\frac{1}{2}} \times 0.0487 \tag{3.103}$$

3.4.2.3. Suspension deflection

Similar to the approaches applied to ride comfort and tire grip in the above, the suspension deflection performance can also be examined based on Equation (3.60). From Equation (3.60),

$$H_3(s) = \frac{-s\omega_1^2}{s^2(s^2 + \frac{\beta}{\alpha}s^2 + \frac{2\zeta\omega_2}{\alpha}s + \frac{\omega_2^2}{\alpha} + \omega_1^2) + (s^2 + \omega_1^2)(\beta s^2 + 2\zeta\omega_2 s + \omega_2^2)} \tag{3.104}$$

It is known that (Li *et al* 2011)

$$\left\|H_3(s)\right\|_2 = (\frac{1}{2\pi}\int_{-\infty}^{\infty}\left|H_3(j\omega)\right|^2 d\omega)^{\frac{1}{2}} \tag{3.105}$$

Substituting Equation (3.104) into Equation (3.105) with $s=j\omega$, then one has

$$\left\|H_3(s)\right\|_2 = (\frac{\alpha\omega_1^2}{4\zeta\omega_2})^{\frac{1}{2}} \tag{3.106}$$

Equation (3.106) is different from Equation (3.90) and (3.69). It is a monotone increasing function of ζ and is not affected by β. Therefore the optimal $\left\|H_3(s)\right\|_2$ is itself. As a result

$$M_{op3} = 0.2\pi(G_q(n_0)v)^{\frac{1}{2}}\left\|H_3(s)\right\|_2 = 0.2\pi(G_q(n_0)v)^{\frac{1}{2}}(\frac{\alpha\omega_1^2}{4\zeta\omega_2})^{\frac{1}{2}} \tag{3.107}$$

According to Li *et al* (2011), and Smith and Wang (2004), the performance of the vehicle suspension with this two-terminal CMI hydraulic system can be better than the conventional suspension. The comparison between the two-terminal CMI hydraulic-flywheel system and the two-terminal VMI hydraulic-flywheel system will be carried out.

3.5. Passive Two-terminal VMI Hydraulic-flywheel System Used in Vehicle Suspension

As mentioned in Section 3.3, a new variable moment of inertia flywheel has been proposed to replace the conventional constant moment of inertia flywheel in this thesis. In this section, the details of this new system used in a vehicle suspension will be discussed.

3.5.1. Equations of Motion

The associated two-degree-of-freedom quarter car model is shown in Figure 3.11 and the force analysis is shown in Figure 3.12.

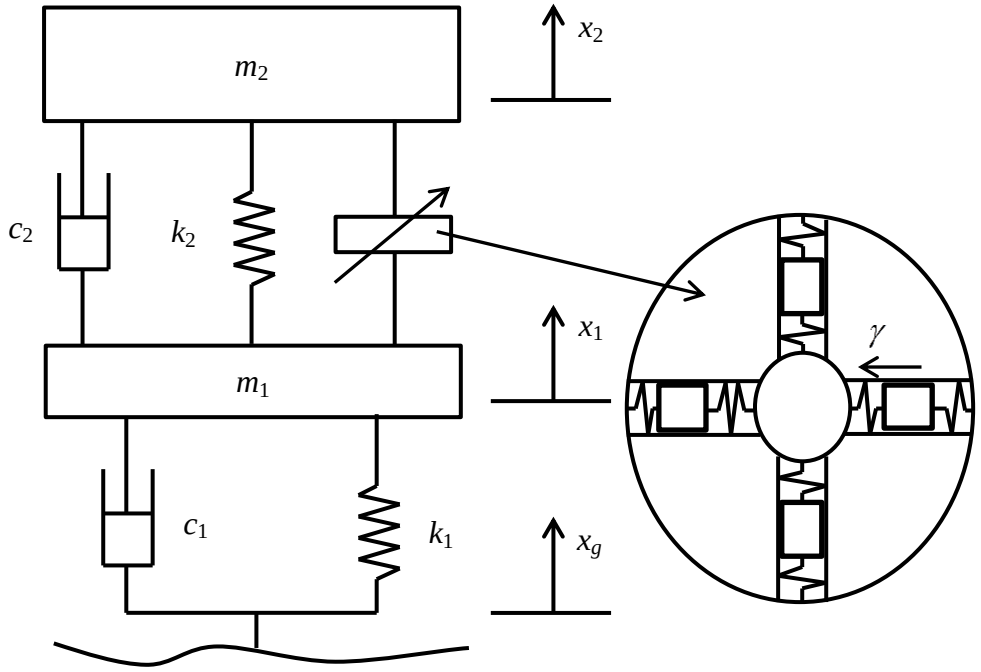

Figure 3.11. Two-degree-of-freedom quarter-car model with a two-terminal variable-mass hydraulic-flywheel system

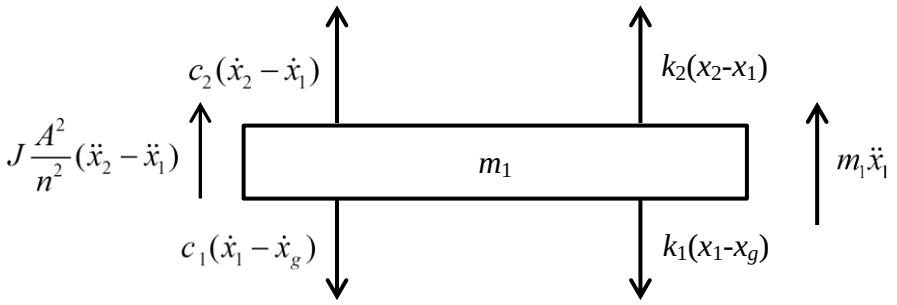

(a)

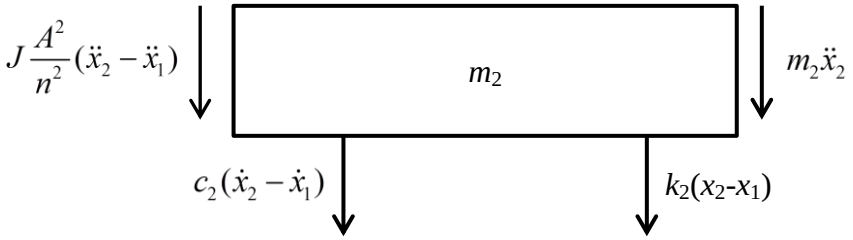

(b)

Figure 3.12. Force analysis of the vehicle suspension using a two-terminal VMI hydraulic-flywheel system, where J represents the moment of inertia of the flywheel

The equation of motion is given by

$$\begin{cases} m_1\ddot{x}_1 + J\frac{A^2}{n^2}(\ddot{x}_1-\ddot{x}_2)+(c_1+c_2)\dot{x}_1-c_2\dot{x}_2+(k_1+k_2)x_1-k_2x_2-k_1x_g-c_1\dot{x}_g=0 \\ m_2\ddot{x}_2 + J\frac{A^2}{n^2}(\ddot{x}_2-\ddot{x}_1)-c_2\dot{x}_1+c_2\dot{x}_2-k_2x_1+k_2x_2=0 \end{cases} \tag{3.108}$$

or

$$\begin{bmatrix} m_1+J\frac{A^2}{n^2} & -J\frac{A^2}{n^2} \\ -J\frac{A^2}{n^2} & m_2+J\frac{A^2}{n^2} \end{bmatrix}\begin{bmatrix}\ddot{x}_1\\ \ddot{x}_2\end{bmatrix}+\begin{bmatrix} c_1+c_2 & -c_2 \\ -c_2 & c_2\end{bmatrix}\begin{bmatrix}\dot{x}_1\\ \dot{x}_2\end{bmatrix}+\begin{bmatrix} k_1+k_2 & -k_2 \\ -k_2 & k_2\end{bmatrix}\begin{bmatrix}x_1\\ x_2\end{bmatrix} = \begin{bmatrix} k_1x_g+c_1\dot{x}_g \\ 0\end{bmatrix} \tag{3.109}$$

where

$$\begin{cases} m_s(\gamma\omega^2+\ddot{\gamma})+k_s(\gamma-\gamma_0)=0 \\ J=\dfrac{1}{12}M_s(\dfrac{3}{4}d_s^2+h^2)+M_s\gamma^2+\dfrac{1}{2}M_c r^2 \\ \omega=\dfrac{A}{n}(\dot{x}_1-\dot{x}_2) \end{cases} \tag{3.110}$$

Equation (3.110) is the same as Equation (3.51). It is rewritten again here since it is important to the whole system. The equation of motion is similar to that of the constant-mass system. However, it is a non-linear system according to Equation (3.110). The new methods used for analyzing this non-linear system will be introduced next.

3.5.2. Performance Criteria

In some references, e.g., Li *et al* (2011), and Smith and Wang (2004) referred to in Section 3.4, three important performance metrics, namely, ride comfort, road handling/safety (tire grip) and suspension deflection are calculated in frequency domain and the transfer function of the system is used for optimization. For example, in (Li *et al* 2011), the ride comfort is defined as

$$M_1=(\frac{1}{2\pi}\int_{-\infty}^{\infty}\left|\frac{s^2\hat{x}_2}{\hat{x}_0}\right|^2 G_q(f)d\omega)^{\frac{1}{2}}=0.2\pi(G_q(n_0)v)^{\frac{1}{2}}\left\|H_1(s)\right\|_2 \tag{3.111}$$

where $\dfrac{s^2\hat{x}_2}{\hat{x}_0}$ is the transfer function from the excitation to the vertical acceleration of the vehicle body and it is the function of the input frequency $\dfrac{\omega}{2\pi}$, which has a very important physical meaning.

To reduce the vertical acceleration of the vehicle body, it is desirable for a suspension system to absorb more vibration energy. For an excitation with only one frequency, the smaller transfer function, the better ride comfort. For ride comfort (M_1), all the input frequencies are considered from -∞ to ∞, then each weighted value for them can be

calculated. The summation of them is the ride comfort (M_1). The smaller M_1, the better ride comfort the vehicle suspension can provide.

However, there is no transfer function for a non-linear system, which means the methods used in the literature no longer work. A better way to analyze a non-linear system is using Matlab to obtain the numerical solutions of the non-linear equations of motion in time domain. Because a non-linear system performs differently for different inputs, every different excitation has to be calculated respectively in the time domain. Though this is more complicated than analyzing the linear system in the frequency domain by a transfer function, the method discussed below has some advantages over a linear system.

3.5.2.1. Ride Comfort

According to ISO 2631-1, the weighted root mean square (r.m.s.) acceleration is expressed in meters per second squared (m/s^2) for translational vibration. The weighted r.m.s. acceleration shall be calculated in accordance with the following equation:

$$a_w = \left(\frac{1}{T}\int_0^T a(t)^2 dt\right)^{\frac{1}{2}} \tag{3.112}$$

Equation (3.112) indicates that in the time domain, there is a weighted r.m.s. acceleration (a_w) for every system input. In this thesis, Matlab is used to solve the non-linear equations of motion, obtain the acceleration vector $a(t)$, and hence the weighted r.m.s. acceleration a_w. As many a_w as required can be obtained by providing sufficient inputs. Suppose we obtain n a_w's, i.e., a_{w1}, a_{w2}, a_{w3}, $\cdots$, a_{wn}. They compose a vector V_{wa} (weighted r.m.s. acceleration vector), i.e.

$$V_{wa} = [a_{w1} \quad a_{w2} \quad a_{w3} \quad \cdots \quad a_{wn}] \tag{3.113}$$

The ride comfort metric is calculated by

$$J_1 = \left[\frac{1}{n}\sum_0^n (a_{w1}{}^2 + a_{w2}{}^2 + a_{w3}{}^2 + \cdots + a_{wn}{}^2)\right]^{\frac{1}{2}} \tag{3.114}$$

Or equivalently

$$J_1 = \left(\frac{1}{n}\right)^{\frac{1}{2}} \left\| V_{wa} \right\|_2 \tag{3.115}$$

For example, if the suspension system is subjected to four different kinds of excitations e_1, e_2, e_3 and e_4 whose corresponding weighted r.m.s. accelerations are a_{w1}=1, a_{w2}=2, a_{w3}=3, a_{w4}=4, then

$$J_1 = (\frac{1}{n})^{\frac{1}{2}} \left\| V_{wa} \right\|_2 = (\frac{1}{4})^{\frac{1}{2}} \times (1^2 + 2^2 + 3^2 + 4^2)^{\frac{1}{2}} = 2.74 \tag{3.116}$$

3.5.2.2. Road Handling and Safety (tire grip)

According to Zuo and Zhang (2012), the road handling index is defined as the ratio between dynamic loads to static load, i.e.

$$\eta_{RS} = \frac{k_1(x_1 - x_0)}{(m_1 + m_2)g} \tag{3.117}$$

where k_1 is the stiffness of the tire, x_1-x_0 is the vertical displacement of the tire (or the compress value of the tire), m_1+m_2 is the total mass of the vehicle, and g is the acceleration of gravity. η_{RS} is a function of time. Just like the method for ride comfort, the weighted road handling index can be defined as

$$\eta_w = (\frac{1}{T}\int_0^T \eta_{RS}(t)^2 dt)^{\frac{1}{2}} \tag{3.118}$$

Similar to the discussions in Section 3.5.2.1, a desired number of η_w's, e.g., η_{w1}, η_{w2}, η_{w3},$\cdots$, η_{wn} can be obtained for a sufficient number of different inputs. The associated weighted road handling index vector $V_{w\eta}$ is

$$V_{w\eta} = [\eta_{w1} \quad \eta_{w2} \quad \eta_{w3} \quad \cdots \quad \eta_{wn}] \tag{3.119}$$

Accordingly, the road handling and safety (tire grip) metric is given by

$$J_2 = [\frac{1}{n}\sum_0^n (\eta_{w1}{}^2 + \eta_{w2}{}^2 + \eta_{w3}{}^2 + \cdots \eta_{wn}{}^2)]^{\frac{1}{2}} \tag{3.120}$$

or

$$J_2 = (\frac{1}{n})^{\frac{1}{2}} \left\| V_{w\eta} \right\|_2 \tag{3.121}$$

3.5.2.3. Suspension Deflection

The suspension deflection is related to the vehicle center of gravity and the suspension life and is expressed as

$$D(t) = x_2 - x_1 \tag{3.122}$$

where D(t) is the suspension deflection which is the function of time, x_2 is the displacement of the vehicle body, and x_1 is the displacement of the unsprung mass (the mass of the chassis).

Like the method above, the weighted suspension deflection is

$$D_w = (\frac{1}{T}\int_0^T D(t)^2 dt)^{\frac{1}{2}} \tag{3.123}$$

Again, from a sufficient number of inputs, a weighted suspension deflection vector can be obtained

$$V_{wD} = [D_{w1} \quad D_{w2} \quad D_{w3} \quad \cdots \quad D_{wn}] \tag{3.124}$$

The suspension deflection criterion is

$$J_3 = [\frac{1}{n}\sum_0^n (D_{w1}{}^2 + D_{w2}{}^2 + D_{w3}{}^2 + \cdots + D_{wn}{}^2)]^{\frac{1}{2}} \tag{3.125}$$

i.e.,

$$J_3 = (\frac{1}{n})^{\frac{1}{2}} \|V_{wD}\|_2 \tag{3.126}$$

The advantages of this method are as follows:

1. This method is in time domain and hence can be used for a non-linear system.
2. All the desirable responses can be obtained from different excitations.
3. Undesirable responses can be excluded or avoided.

3.6. Performance Comparisons

In this section, the two-terminal CMI hydraulic-flywheel and two-terminal VMI hydraulic-flywheel systems in a vehicle suspension will be compared against the three

criteria mentioned above. Some observations will be also made based on the comparisons.

The numerical methods discussed in Section 3.5 will be used in this section to calculate three performance metrics, i.e., ride comfort, road handling and safety, and suspension deflection for different kinds of excitations shown in Figure 3.13.

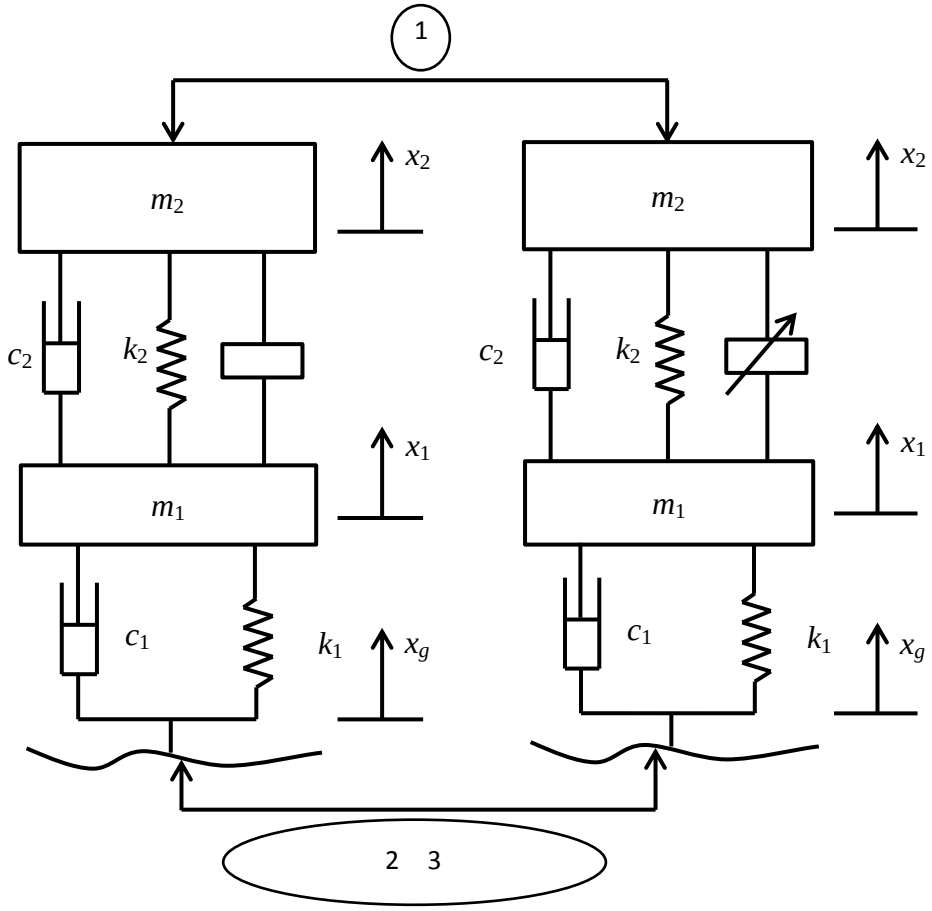

Figure 3.13. Three different kinds of excitations to the suspension system (1-zero input, 2-impulse excitation and 3-sinusoidal excitation)

The equations of motion of this suspension system can be obtained by combining Equations (3.109) and (3.111) as follows:

$$\begin{cases} m_1\ddot{x}_1 + J\dfrac{A^2}{n^2}(\ddot{x}_1 - \ddot{x}_2) + (c_1 + c_2)\dot{x}_1 - c_2\dot{x}_2 + (k_1 + k_2)x_1 - k_2x_2 - k_1x_g - c_1\dot{x}_g = 0 \\ m_2\ddot{x}_2 + J\dfrac{A^2}{n^2}(\ddot{x}_2 - \ddot{x}_1) - c_2\dot{x}_1 + c_2\dot{x}_2 - k_2x_1 + k_2x_2 = 0 \\ m_s(\gamma\omega^2 + \ddot{\gamma}) + k_s(\gamma - \gamma_0) = 0 \\ J = \dfrac{1}{12}M_s(\dfrac{3}{4}d_s^2 + h^2) + M_s\gamma^2 + \dfrac{1}{2}M_cr^2 \\ \omega = \dfrac{A}{n}(\dot{x}_1 - \dot{x}_2) \end{cases} \tag{3.127}$$

The motion of a slider along its track leads to friction (assumed to be constant). The friction is determined by the pressure between the slider and the track. According to Equation (3.36), this pressure is given by

$$F_p = a_x m_s = (a_{et} + a_c)m_s \tag{3.128}$$

where μ is the friction coefficient between the sliders and the guide tracks. If the sliders and tracks are made of steel, μ=0.02.

In Equation (3.128),

$$\begin{cases} a_{et} = \dot{\omega} \\ a_c = 2\omega v_r \end{cases} \tag{3.129}$$

where v_r ($v_r = \dot{\gamma}$) is the relative velocity between a slider and a track. The friction is given by

$$f = F_p\mu \tag{3.130}$$

Substituting Equations (3.128) and (3.129) into Equation (3.130), the friction force contributed by all the *n* slider-track pairs is obtained by

$$f = N\mu(\dot{\omega} + 2\omega v_r)m_s \tag{3.131}$$

As mentioned before, ω and $\dot{\omega}$ can be obtained by

$$\begin{cases} \omega = \dfrac{A}{n}(\dot{x}_1 - \dot{x}_2) \\ \dot{\omega} = \dfrac{A}{n}(\ddot{x}_1 - \ddot{x}_2) \end{cases} \tag{3.132}$$

For our system, A=0.0012566m^2, n=1.30607$\times 10^{-6}$m^3/rad. Assuming m_s=0.1kg, μ=0.02, $\overline{\dot{\gamma}} = 0.4\text{m/s}$, $\overline{\dot{x}_1 - \dot{x}_2} = 0.05\text{m/s}$ and $\overline{\ddot{x}_1 - \ddot{x}_2} = 1.2\text{m/s}^2$ (The upper bar means average), the average friction force caused by all the n slider-track pairs is

$$\overline{f} = N\mu(\dot{\omega} + 2\omega v_r)m_s \approx 9.5\,\text{N} \tag{3.133}$$

As the angular velocity increases, this friction also increases. This leads to a damping effect in the system with the damping coefficient c_s, i.e.

$$\overline{f} = c_s \overline{\dot{\gamma}} \tag{3.134}$$

For the proposed design

$$c_s = \frac{\overline{f}}{\overline{\dot{\gamma}}} \approx 24\text{N s/m} \tag{3.135}$$

By taking into account of the friction, Equation (3.128) is expanded to

$$\begin{cases} m_1\ddot{x}_1 + J\dfrac{A^2}{n^2}(\ddot{x}_1 - \ddot{x}_2) + (c_1 + c_2)\dot{x}_1 - c_2\dot{x}_2 + (k_1 + k_2)x_1 - k_2x_2 - k_1x_g - c_1\dot{x}_g = 0 \\ m_2\ddot{x}_2 + J\dfrac{A^2}{n^2}(\ddot{x}_2 - \ddot{x}_1) - c_2\dot{x}_1 + c_2\dot{x}_2 - k_2x_1 + k_2x_2 = 0 \\ m_s(\gamma\omega^2 + \ddot{\gamma}) + k_s(\gamma - \gamma_0) + c_s\dot{\gamma} = 0 \\ J = \dfrac{1}{12}M_s(\dfrac{3}{4}d_s^2 + h^2) + M_s\gamma^2 + \dfrac{1}{2}M_cr^2 \\ \omega = \dfrac{A}{n}(\dot{x}_1 - \dot{x}_2) \end{cases} \tag{3.136}$$

where $c_s = 24\,\text{N s/m}$.

Equation (3.136) will be used as the equation of motion of the suspension system for the remaining part of this thesis.

According to Table 3.1, for our CMI prototype, the mass of the flywheel is 0.725kg and the radius of the flywheel is 0.045m and hence the moment of inertia is

$$J = \frac{1}{2} \times 0.725\text{kg} \times (0.045\text{m})^2 = 7.34 \times 10^{-4}\,\text{kg m}^2 \tag{3.137}$$

Suppose there are four sliders, each weighs 0.14kg, in the VMI flywheel, i.e. M_s=4×0.14kg=0.56kg, d_s=h=0.02m, γ_0=0.03m, r=0.045m and M_c=0.2kg. When the flywheel is static (γ=γ_0), the moment of inertia of the flywheel is given by

$$J = \frac{1}{12} M_s (\frac{3}{4} d_s^2 + h^2) + M_s \gamma^2 + \frac{1}{2} M_c r^2 = 7.34 \times 10^{-4} \text{kg m}^2 \qquad (3.138)$$

It means the moment of inertia of the VMI flywheel is equal to that of the constant one when it is static. The performance criteria will be discussed next based on Equation (3.136) by numerical methods. However, before the discussion, all the parameters of the suspension system should be known. For a common quarter-car model shown in Figure 3.11, the parameters can be assumed to be

$$\begin{cases} m_1 = 30\text{kg} \\ m_2 = 300\text{kg} \\ k_1 = 100000\text{N/m} \\ k_2 = 80000\text{N/m} \\ c_1 = 1000\text{N s/m} \\ c_2 = 4000\text{N s/m} \end{cases} \qquad (3.139)$$

It should be noted that m_2 is the mass of the vehicle body including passengers and cargo load, which may not be constant depending on the number of passengers and the quantity of the cargo. The performance evaluations for different vehicle body mass ranging from 250kg to 350kg and different excitations will be discussed next.

3.6.1. Ride Comfort

(1) Zero input

Now, an initial displacement x_0=0.03m is given to the vehicle body (m_2). According to the methods mentioned in Section 3.5, the weighted acceleration of the vehicle body can be calculated by the function ode45 in Matlab. For example, if m_2=300kg, the vehicle body displacements and acceleration responses of both the CMI and VMI systems are plotted in Figure 3.14.

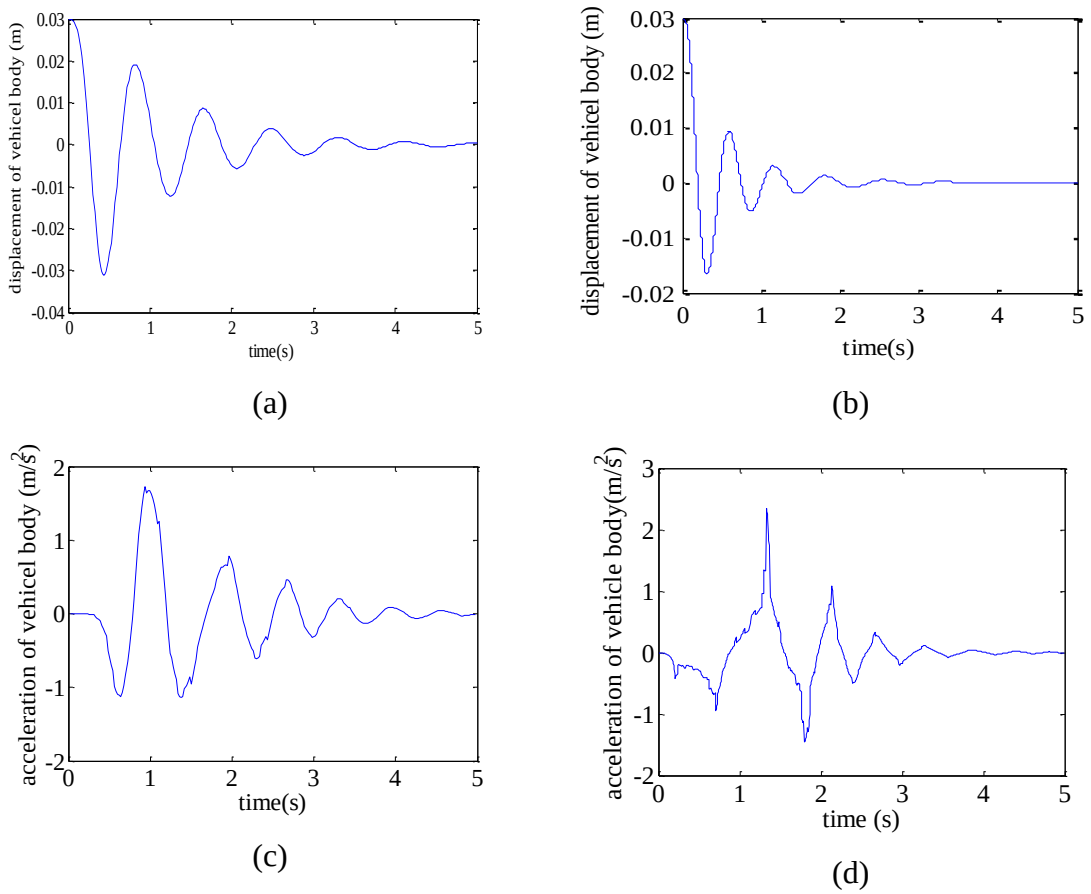

Figure 3.14. Comparison of zero input response between the CMI and VMI suspension systems for m_2=300kg: (a), (c) are the displacements of the vehicle body with a CMI suspension system; and (b), (d) are the displacements of the vehicle body with a VMI suspension system

The relationship between response and vehicle body mass can be obtained by changing vehicle body mass from 250kg to 350kg (in this section all the vehicle body mass are from 250kg to 350kg). The responses are similar to those shown in Figure 3.14 and are not presented in this thesis. The weighted accelerations of the vehicle body are considered based on Equation (3.112), which is shown in Table 3.3 and Figure 3.15.

Table 3.3. Comparison of the weighted acceleration of the vehicle body for zero input excitation between CMI and VMI suspension systems

Vehicle body mass m_2 (kg)	**Weighted accelerations of CMI suspension system**	**Weighted accelerations of VMI suspension system**

	a_w(m/s^2)	a_w(m/s^2)
250	0.5736	0.4349
260	0.5605	0.4360
270	0.5515	0.4227
280	0.5418	0.4226
290	0.5346	0.4247
300	0.5255	0.4360
310	0.5153	0.4287
320	0.5091	0.4245
330	0.5031	0.4162
340	0.5071	0.4134
350	0.4971	0.4156

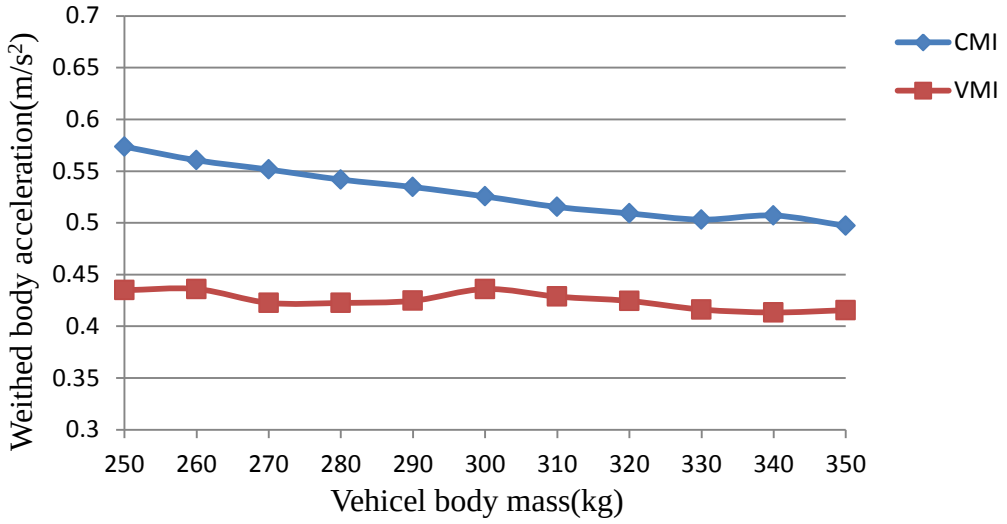

Figure 3.15. Comparison of the weighted accelerations of the vehicle body for zero input excitation between CMI and VMI suspension system

(2) Impulse excitation

If an impulse excitation shown in Figure 3.16 from the road is given to the tire, the vehicle body displacement and acceleration responses of both CMI and VMI system are shown in Figure 3.17.

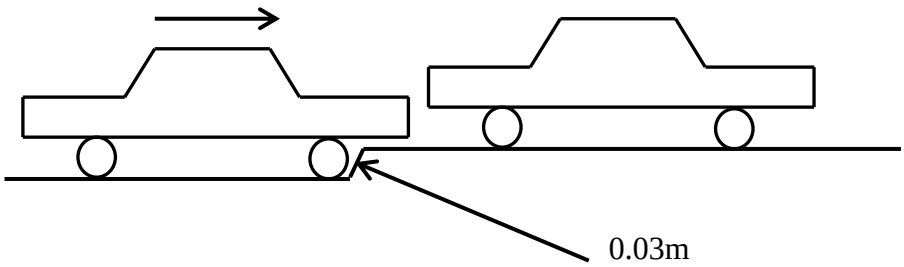

Figure 3.16. Impulse excitation from the road

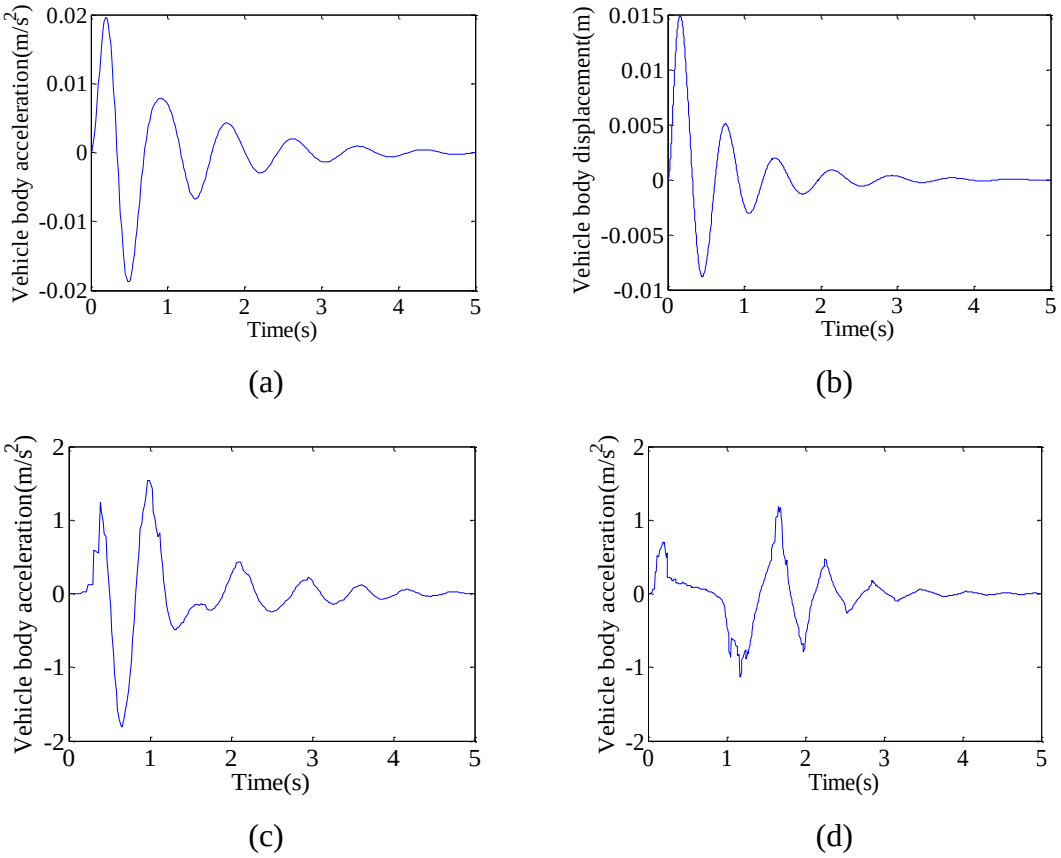

Figure 3.17. Comparison of impulse excitation responses between the CMI and VMI suspension systems for m_2=300kg: (a), (c) are the displacements of the vehicle body with a CMI suspension system; and (b), (d) are the displacements of the vehicle body with a VMI suspension system

The weighted accelerations of the vehicle body for different vehicle body mass based on Equation (3.112) are shown in Table 3.4 and Figure 3.18.

Table 3.4. Comparison of the weighted acceleration of the vehicle body for impulse excitation between CMI and VMI suspension systems

Vehicle body mass m_2 (kg)	**Weighted accelerations of CMI suspension system a_w(m/s^2)**	**Weighted accelerations of VMI suspension system a_w(m/s^2)**
250	0.5957	0.3889
260	0.5738	0.3784
270	0.5649	0.3740
280	0.5481	0.3645
290	0.5396	0.3573
300	0.5239	0.3501
310	0.5129	0.3395
320	0.4985	0.3340
330	0.4918	0.3324
340	0.4820	0.3228
350	0.4721	0.3177

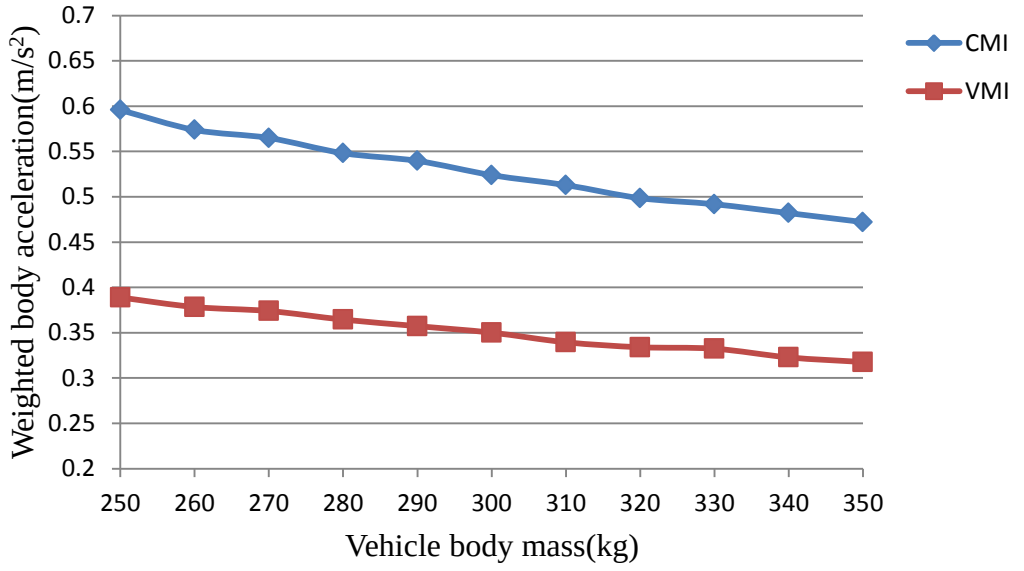

Figure 3.18. Comparison of the weighted accelerations of the vehicle body for impulse excitation between CMI and VMI suspension systems

(3) Sinusoidal excitation

When a sine wave shown in Figure 3.19 from the road is given to the tire, the vehicle body displacements and acceleration responses of both CMI system and VMI system are shown in Figure 3.20.

Suppose the sine wave is $A\sin(\omega t)$, the wavelength of the sine wave is λ=4m, the amplitude of the sine wave is A=0.02m, and the driving speed of the vehicle is v_d=10m/s. The frequency of the input f is given by

$$f = \frac{v_d}{\lambda} = 2.5Hz \tag{3.140}$$

Hence

$$\begin{cases} A = 0.02\,\mathrm{m} \\ \omega = 2\pi f = 5\pi\,\mathrm{rad/s} \end{cases} \tag{3.141}$$

and

$$A\sin(\omega t) = 0.02\sin(5\pi t) \tag{3.142}$$

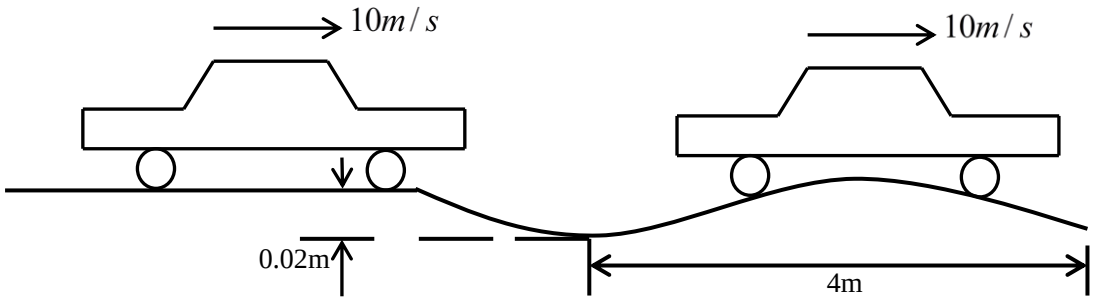

Figure 3.19. Sinusoidal excitation from the road

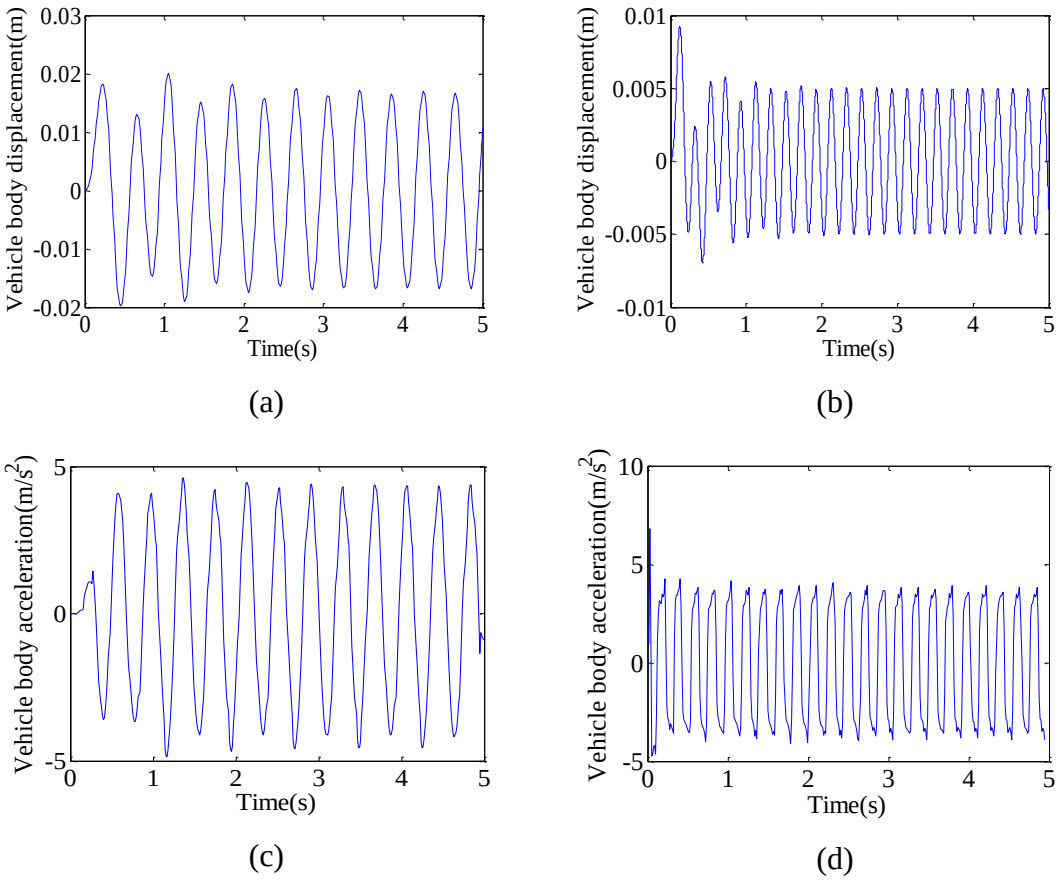

Figure 3.20. Comparison of sinusoidal excitation responses between the CMI and VMI suspension systems for m_2=300kg: (a), (c) are the displacements of the vehicle body with a CMI suspension system; and (b), (d) are the displacements of the vehicle body with a VMI suspension system

The weighted accelerations of the vehicle body for different vehicle body mass calculated based on Equation (3.112) are shown in Table 3.5 and Figure 3.21.

Table 3.5. Comparison of the weighted acceleration of the vehicle body for sinusoidal excitation between the CMI and VMI suspension systems

Vehicle body mass m_2 (kg)	**Weighted accelerations of CMI suspension system a_w(m/s^2)**	**Weighted accelerations of VMI suspension system a_w(m/s^2)**
250	3.1006	6.3081
260	3.0519	6.0064
270	3.0071	5.7810
280	2.9618	5.3393
290	2.9172	5.2009
300	2.8865	4.9043
310	2.8454	4.6827
320	2.8049	4.5805
330	2.7772	4.4129
340	2.7359	4.2090
350	2.6988	4.1454

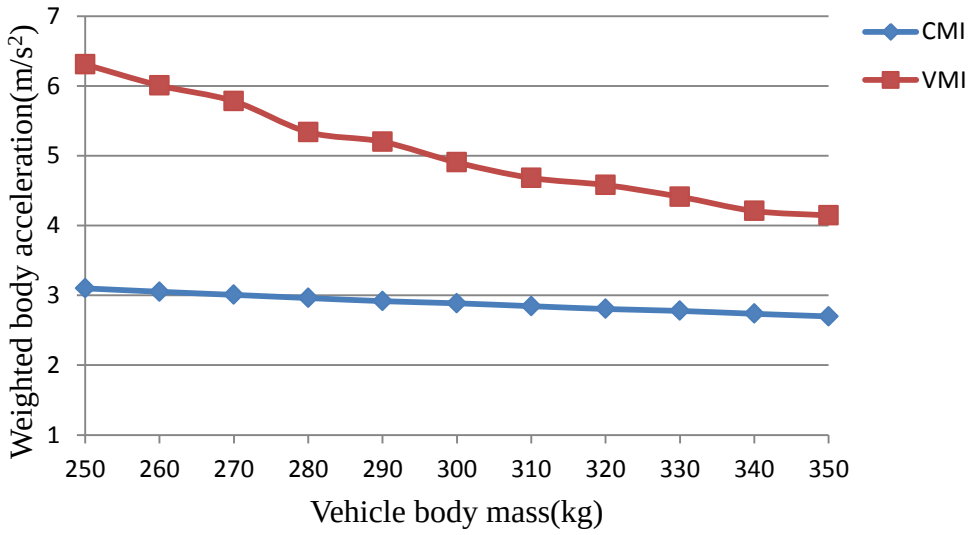

Figure 3.21 Comparison of the weighted accelerations of the vehicle body for sinusoidal excitation between the CMI and VMI suspension systems

3.6.2. Road Handling and Safety (tire grip)

In this section, the road handling and safety of the CMI and VMI suspension systems will be calculated for different vehicle body masses and different excitations.

(1) Zero input

According to Equations (3.117) and (3.118), the weighted road handling indices for zero input excitation of both suspension systems for different vehicle body masses are listed in Table 3.6 and plotted in Figure 3.22.

Table 3.6. Comparison of the weighted road handling index for zero input excitation between the CMI and VMI suspension systems

Vehicle body mass m_2 (kg)	**Weighted road handling index of CMI suspension system η_{RS}**	**Weighted road handling index of VMI suspension system η_{RS}**
250	0.2179	0.0735
260	0.2090	0.0720
270	0.2010	0.0706
280	0.1934	0.0691
290	0.1865	0.0680
300	0.1800	0.0668
310	0.1741	0.0656
320	0.1685	0.0645
330	0.1631	0.0634
340	0.1581	0.0624
350	0.1536	0.0615

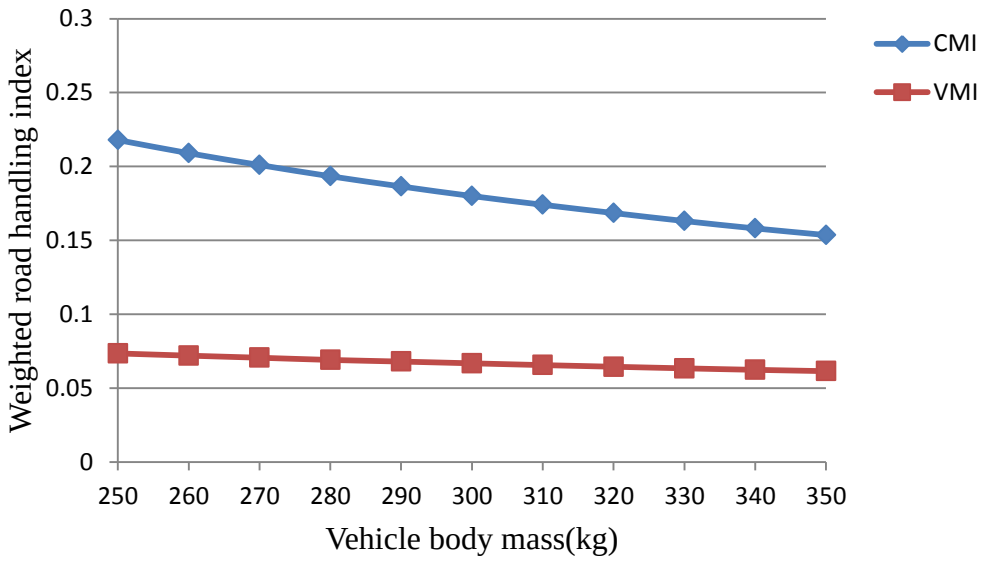

Figure 3.22. Comparison of the weighted road handling index for zero input excitation between the CMI and VMI suspension systems

(2) Impulse excitation

In parallel to the zero input excitation, the weighted road handling index for impulse excitation of both suspension systems for different vehicle body masses can be obtained using Equations (3.117) and (3.118). The results are summarized in Table 3.7 and displayed in Figure 3.23.

Table 3.7. Comparison of the weighted road handling index for impulse excitation between the CMI and VMI suspension systems

Vehicle body mass m_2 (kg)	**Weighted road handling index of CMI suspension system η_{RS}**	**Weighted road handling index of VMI suspension system η_{RS}**
250	0.2463	0.1099
260	0.2352	0.1060
270	0.2250	0.1024
280	0.2156	0.0990
290	0.2069	0.0958
300	0.1987	0.0928
310	0.1912	0.0899
320	0.1842	0.0872
330	0.1778	0.0847
340	0.1714	0.0823
350	0.1657	0.0801

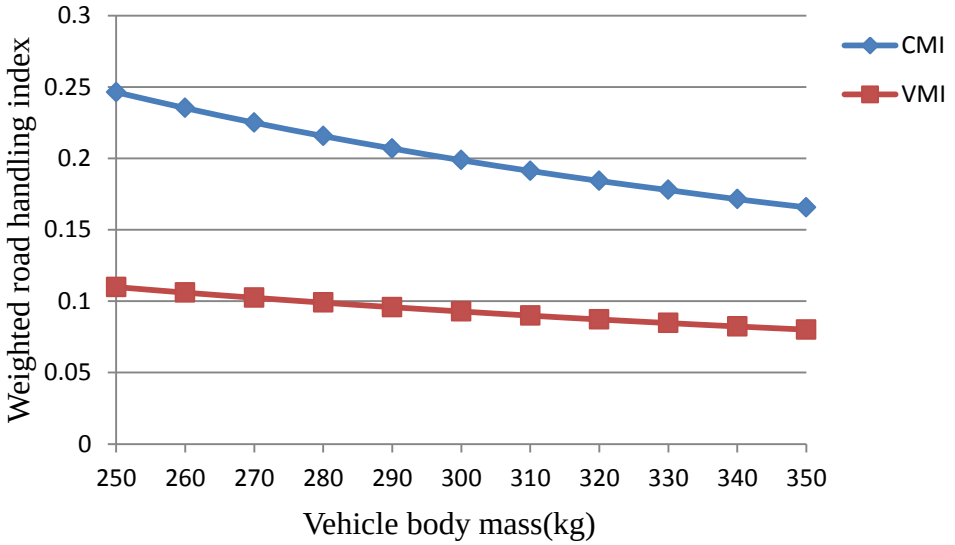

Figure 3.23. Comparison of the weighted road handling index for impulse excitation between the CMI and VMI suspension systems

(3) Sinusoidal excitation

According to Equations (3.117) and (3.118), the weighted road handling indices for sine wave excitation of both suspension systems associated with different vehicle body mass are shown in Table 3.8 and Figure 3.24.

Table 3.8. Comparison of the weighted road handling index for sinusoidal excitation between the CMI and VMI suspension systems

Vehicle body mass m_2 (kg)	**Weighted road handling index of CMI suspension system η_{RS}**	**Weighted road handling index of VMI suspension system η_{RS}**
250	0.6734	0.5839
260	0.6495	0.5314
270	0.6273	0.4855
280	0.6065	0.4452
290	0.5870	0.4100
300	0.5687	0.3792
310	0.5515	0.3520
320	0.5353	0.3281
330	0.5200	0.3070
340	0.5055	0.2882
350	0.4918	0.2716

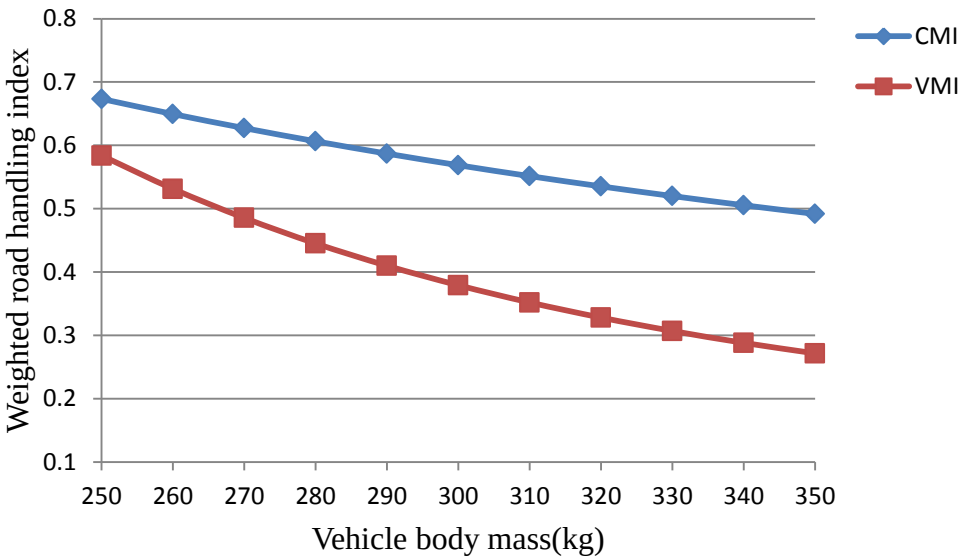

Figure 3.24. Comparison of the weighted road handling index for sinusoidal excitation between the CMI and VMI suspension systems

3.6.3. Suspension Deflection

In this section, the suspension deflection of CMI and VMI suspension system will be calculated for different vehicle body masses and different excitations.

(1) Zero input

The range of the vehicle body mass is also from 250kg to 350kg. According to Equations (3.122) and (3.123), the weighted suspension deflections for zero input excitation of both suspension systems for different vehicle body masses are shown in Table 3.9 and plotted in Figure 3.25.

Table 3.9. Comparison of the weighted suspension deflections for zero input excitation between the CMI and VMI suspension systems

Vehicle body mass m_2 (kg)	**Weighted suspension deflections of CMI suspension system D_w(m)**	**Weighted suspension deflections of VMI suspension system D_w(m)**
250	0.0048	0.0037
260	0.0048	0.0038
270	0.0048	0.0038
280	0.0048	0.0038
290	0.0049	0.0038
300	0.0049	0.0039
310	0.0049	0.0039
320	0.0049	0.0039
330	0.0049	0.0039
340	0.0050	0.0040
350	0.0050	0.0040

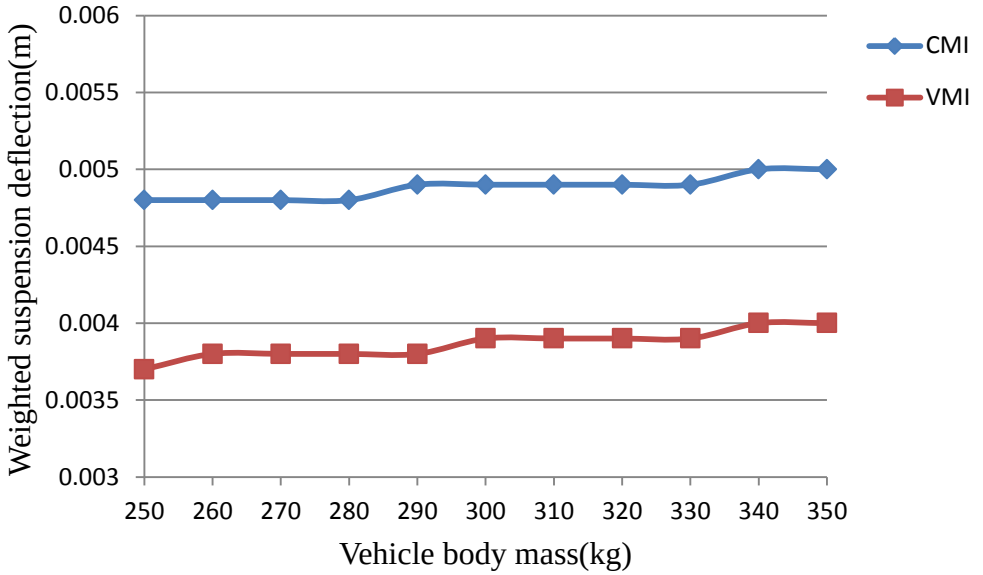

Figure 3.25. Comparison of the weighted suspension deflections for zero input excitation between the CMI and VMI suspension systems

(2) Impulse excitation

The weighted suspension deflections for impulse excitation of both suspension systems for different vehicle body masses are determined according to Equations (3.122) and (3.123). The results are listed in Table 3.10 and also presented in Figure 3.26.

Table 3.10. Comparison of the weighted suspension deflections for impulse excitation between the CMI and VMI suspension systems

Vehicle body mass m_2 (kg)	**Weighted suspension deflections of CMI suspension system D_w(m)**	**Weighted suspension deflections of VMI suspension system D_w(m)**
250	0.0041	0.0031
260	0.0041	0.0031
270	0.0041	0.0031
280	0.0041	0.0031
290	0.0041	0.0031
300	0.0041	0.0031
310	0.0041	0.0031
320	0.0041	0.0031
330	0.0041	0.0031
340	0.0041	0.0031
350	0.0041	0.0031

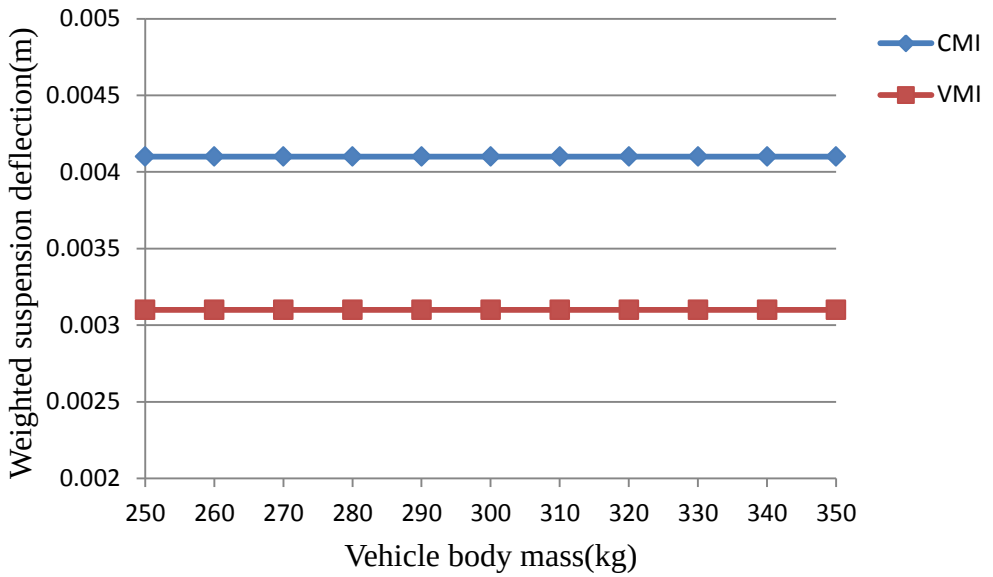

Figure 3.26. Comparison of the weighted suspension deflections for impulse excitation between the CMI and VMI suspension systems

(3) Sinusoidal excitation

Following the same procedure illustrated above, the weighted suspension deflections for sine wave excitation of both suspension systems for different vehicle body mass are shown in table 3.11 and Figure 3.27, based on Equations (3.122) and (3.123).

Table 3.11. Comparison of the weighted suspension deflections for sin wave excitation between the CMI and VMI suspension systems

Vehicle body mass m_2 (kg)	**Weighted suspension deflections of CMI suspension system D_w(m)**	**Weighted suspension deflections of VMI suspension system D_w(m)**
250	0.0072	0.0154
260	0.0074	0.0151
270	0.0076	0.0149
280	0.0077	0.0146
290	0.0079	0.0143
300	0.0081	0.0141
310	0.0082	0.0139
320	0.0084	0.0136
330	0.0085	0.0134
340	0.0086	0.0132
350	0.0088	0.0130

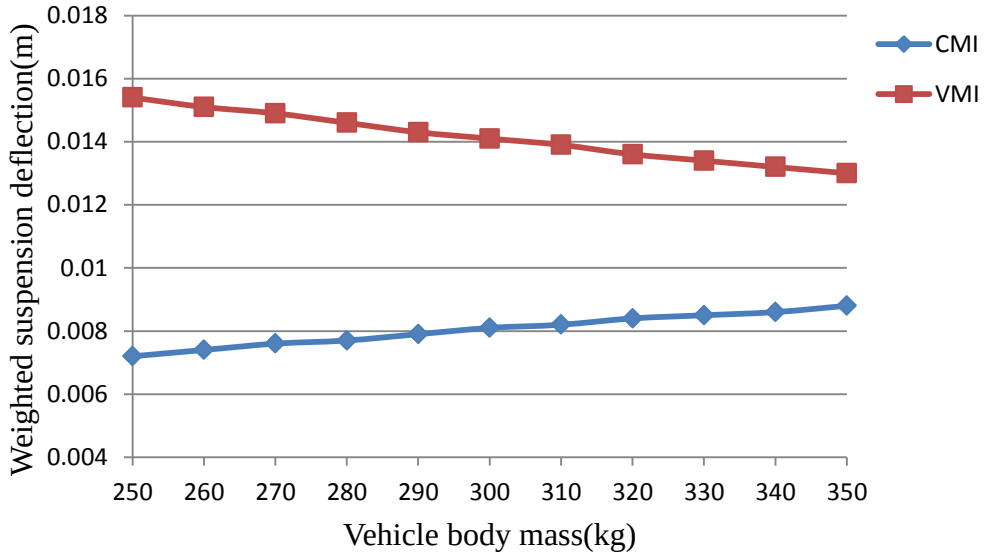

Figure 3.27. Comparison of the weighted suspension deflections for sinusoidal excitation between the CMI and VMI suspension systems

From the above results, the following can be observed:

1. For zero input and impulse input,
    a) The VMI suspension system outperforms the CMI suspension system in terms of all the three criteria, i.e., ride comfort, road handling and safety, and suspension deflection (Figures 3.15, 3.18, 3.22, 3.23, 3.25 and 3.26).
    b) The response time of the VMI suspension system is shorter than that of the CMI suspension system (Figures 3.14 and 3.17).

2. For three different excitations, the average vehicle body displacements of the VMI suspension system are all smaller than those of the CMI suspension system (Figures 3.14, 3.17 and 3.20).

3. For the sinusoidal excitation, the CMI system performs better than the VMI system in terms of ride comfort and suspension deflection, but falls short in terms of road handling and safety (Figures 3.21, 3.24 and 3.27).

Chapter 4. Experimental Studies

This chapter presents the one-degree-of-freedom experimental design and the associated tests to examine the two-terminal hydraulic prototype with different kinds of flywheels. It should be noted that even though it is ideal to carry out two-degree-of-freedom tests, it is not feasible to do so due to the lack of the required test facility (i.e., the quarter-car model). As such, the test focus is placed on examining the two-terminal hydraulic prototype, the comparison between the CMI flywheel and its VMI counterpart, as well as the behavior of the VMI flywheel with the maximum, minimum and variable moments of inertia.

4.1. Experimental Setup

The experimental setups for testing the performance of the two-terminal hydraulic prototype with different kinds of flywheels are as follows:

1. Test Machine:
   (1) MTS810 Materials Testing System
   (2) Built-in PID Controller
2. Test Apparatus:
   (1) Two-terminal hydraulic system with the following dimensions:
   22cm (width), 26cm (length), and 57 (height, when fully compressed) and 67cm (height, when fully extended)
   (2) Variable moment of inertia flywheel (VMI flywheel)
   (3) Constant moment of inertia flywheel (CMI flywheel)
3. Data Acquisition Devices:
   (1) Encoder

(2) NI DAQ

(3) Personal computer

4.1.1. Two-terminal Hydraulic-flywheel Prototype and Test Machine

Figure 4.1 shows the MTS810 test machine with the two-terminal hydraulic prototype mounted. There is no flywheel in Figure 4.1 because the MTS810 test machine and the two-terminal hydraulic prototype need to warm up before the tests. Figure 4.2 shows the controller of the test machine and personal computer. The personal computer is used to acquire data from the encoder via the Labview software.

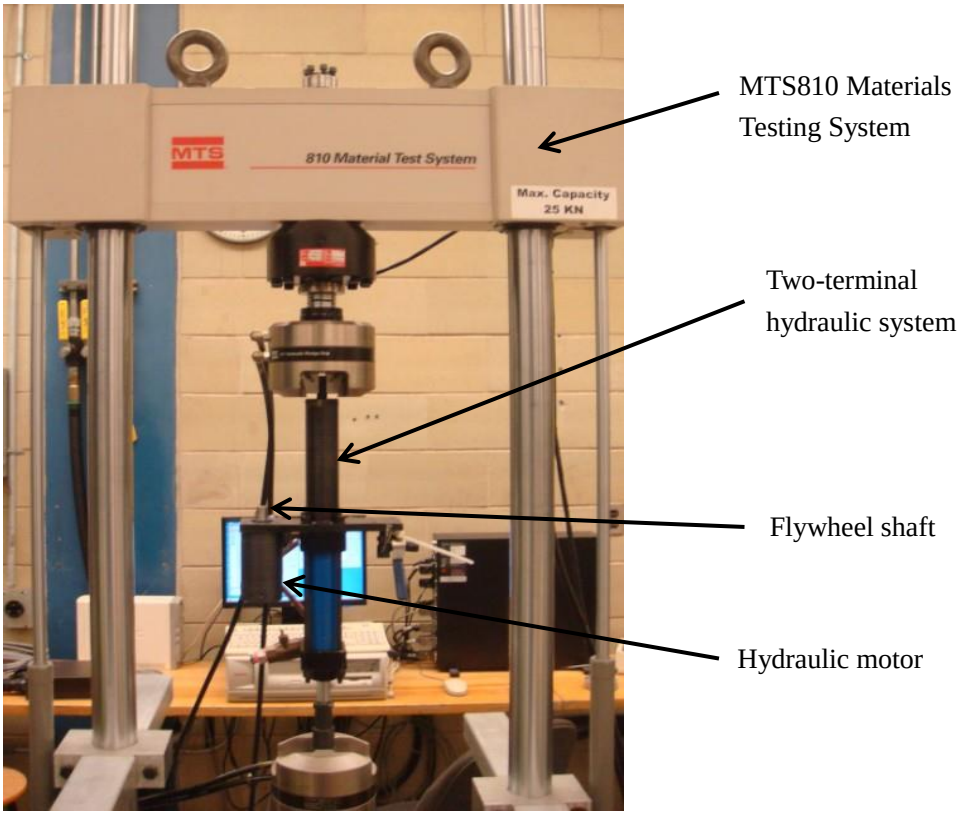

Figure 4.1. MTS810 test machine with the two-terminal hydraulic prototype mounted

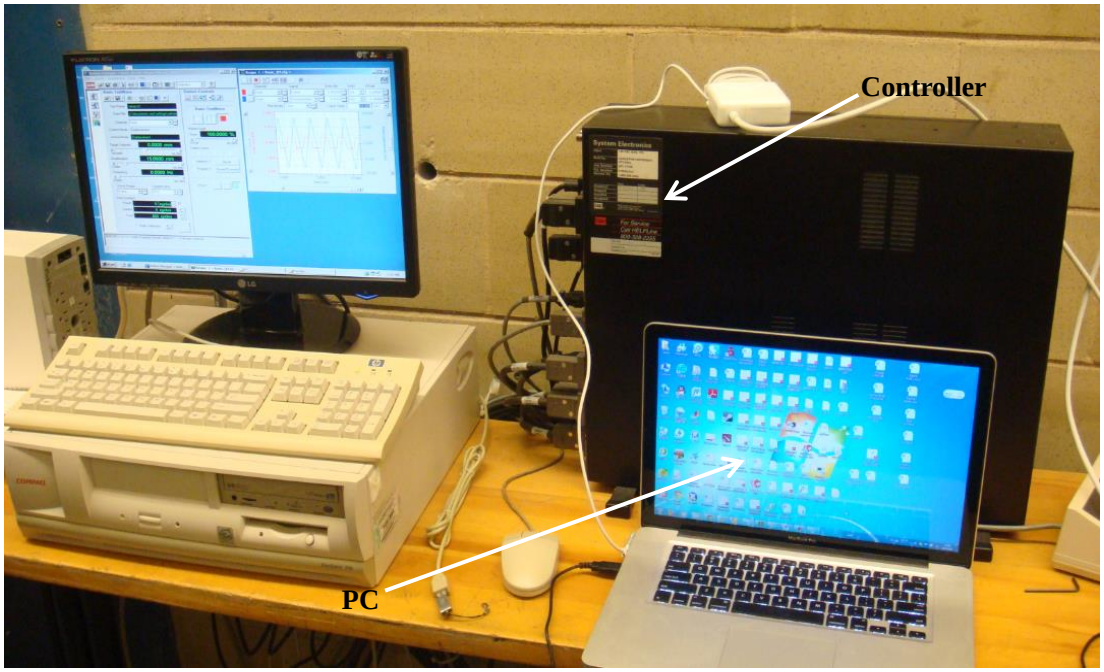

Figure 4.2. Controller of the test machine and personal computer

For our prototype, the parameters shown in Table 3.2 are

$$\begin{cases} A = 0.0009424\text{m}^2 \\ n = 1.30607 \times 10^{-6}\text{m}^3 / \text{rad} \end{cases} \tag{4.1}$$

where A is the cross-sectional area of the cylinder, and n is the displacement of the motor.

4.1.2. Flywheels Used in the Experiment

The CMI flywheel and VMI flywheel shown in Figure 4.3 are used in the tests. The two-terminal hydraulic prototype with the CMI and VMI flywheels will be tested separately and the comparison will be made.

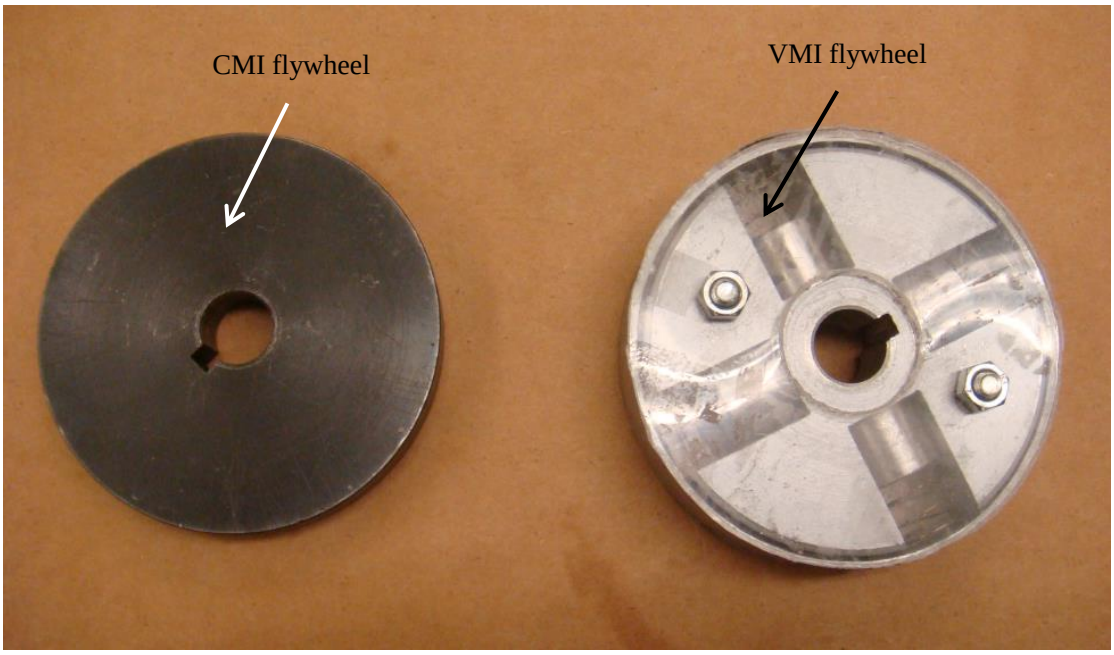

Figure 4.3. CMI flywheel and VMI flywheel

4.1.2.1. VMI flywheel

The VMI flywheel used for the experiment shown in Figure 4.4 is conceptually the same as that discussed in Chapter 3 but slightly different in terms of the slider shape and number of springs. As shown in Figure 4.4, it consists of a support of the track (Figure 4.4. (*b*)), four sliders, four springs, an outer ring (Figure 4.4 (*c*)), two covers and two screws. Each slider now has two flat lateral surfaces (Figure 4.4 (*d*)) to avoid spinning around its axis during the tests. The reduced number of springs is due to the limited space in the tracks. The dimensions of these items are also included in Figure 4.4.

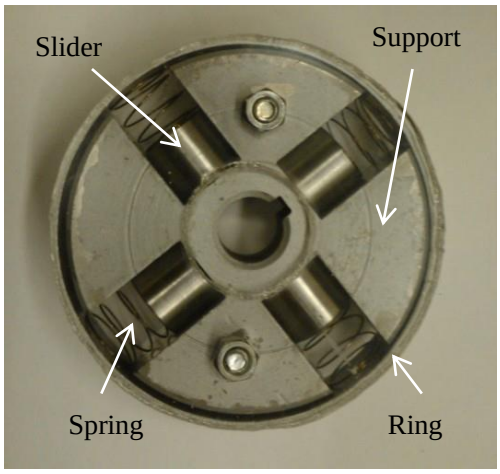

(*a*)

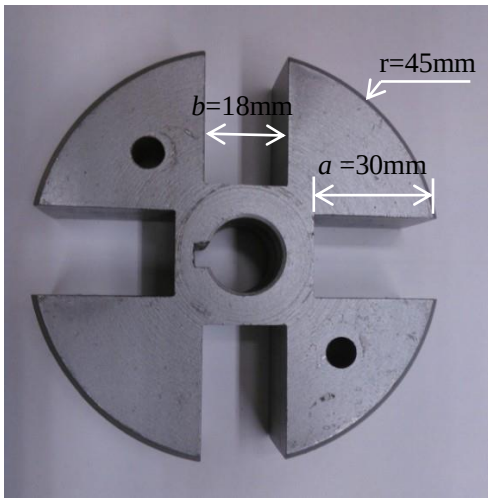

(*b*)

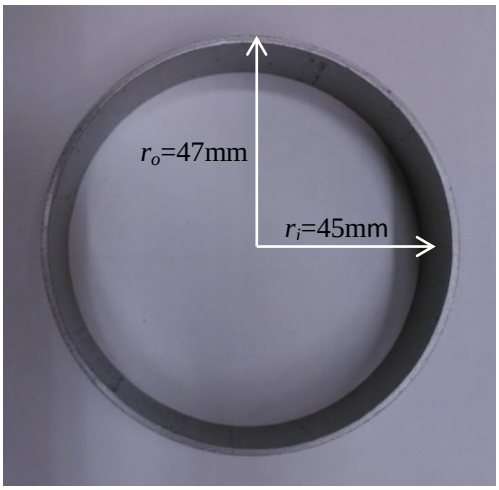

(*c*)

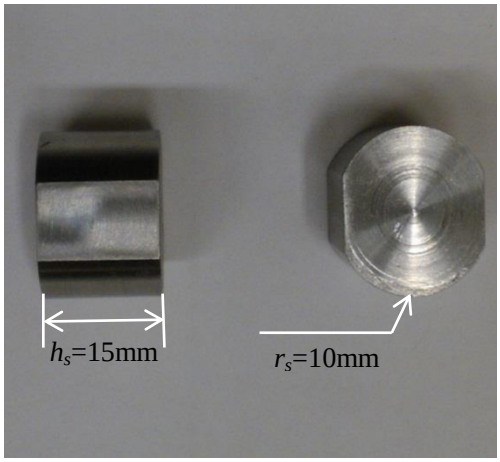

(*d*)

Figure 4.4. Structure of the VMI flywheel: (a) VMI flywheel, (b) support of the tracks, (c) ring, and (d) slider

Before the tests, the mass moment of inertia of the flywheel should be calculated as detailed below.

As the mass of plastic covers, compression springs and screws is very small, their moment of inertia can be neglected. It means that the moment of inertia of the VMI flywheel is mainly contributed from the support of the tracks, the outer ring and four

sliders. The mass of the support, the mass of the ring and the mass of one sliders are respectively m_{su}=0.612kg, m_{ri}=0.077kg, M_s=4m_s=0.140kg (where m_s is the mass of one slider).

Suppose A_{su} is the base area of the support, A_{tr} is the base area of four tracks. After ignoring the base area of two threaded holes, we obtain

$$A_{su} = \pi r^2 - A_{tr} = \pi \times 0.045\text{m}^2 - 4 \times 0.03\text{m} \times 0.018\text{m} = 4.02 \times 10^{-3}\text{m}^2 \qquad (4.2)$$

which leads to

$$V_{su} = A_{su} H = 4.02 \times 10^{-3}\text{m}^2 \times 0.02\text{m} = 8.04 \times 10^{-5}\text{m}^3 \qquad (4.3)$$

where V_{su} is the volume of the support and H the height of the support. Since the height of the support and the tracks, which equal to the height of the flywheel, are identical, H also represents the height of the track and flywheel hereafter.

Therefore the density of the material of the flywheel support ρ is

$$\rho = \frac{m_{su}}{V_{su}} = \frac{0.612\text{kg}}{8.04 \times 10^{-5}\text{m}^3} \approx 7.6 \times 10^3 \text{kg/m}^3 \qquad (4.4)$$

Suppose J_{su} is the mass moment of inertia of the support, J_{tr} the mass moment of inertia of four tracks if they are filled with the same type of material, and J_d the mass moment of inertia of the support without the tracks. Neglecting the two threaded holes and the keyway, it is clear that

$$J_{su} = J_d - J_{tr} \qquad (4.5)$$

In fact, the support without the tracks is a disc and hence

$$J_d = \frac{1}{2} V \rho r^2 = \frac{1}{2} \pi \rho H r^4 \qquad (4.6)$$

Substituting ρ, H, r into Equation (4.6), we obtain

$$J_d = \frac{1}{2} \pi \rho H r^4 = 9.8 \times 10^{-4} \text{kg m}^2 \qquad (4.7)$$

As the shape of the tracks is essentially cuboid, it is easy to obtain their total moment of inertia. Then based on the parallel-axis theorem,

$$J_{tr} = \frac{1}{12} m_{tr}(a^2 + b^2) + m_{tr} d_p^2 \tag{4.8}$$

where a and b are the length and width of the base area respectively as the base area of the tracks is rectangular, d_p the distance between the mass center of the tracks and that of the flywheel. It is known that d_p=0.03m, a=0.03m, b=0.018m. Hence, the value of J_{tr} is given by

$$J_{tr} = 0.32 \times 10^{-3} \text{kg m}^2 \tag{4.9}$$

Therefore, from Equation (4.4), J_{su} is

$$J_{su} = J_d - J_{tr} = 9.8 \times 10^{-4} \text{kg m}^2 - 3.2 \times 10^{-4} \text{kg m}^2 = 6.6 \times 10^{-4} \text{kg m}^2 \tag{4.10}$$

The moment of inertia of the ring shown in Figure 4.1(c) is given by

$$J_{ri} = \frac{1}{2} m_{ri}(r_i^2 + r_o^2) \tag{4.11}$$

Based on the dimension shown in Figure 4.1(c), i.e. r_i=45mm, r_o=47mm,

$$J_{ri} = \frac{1}{2} m_{ri}(r_i^2 + r_o^2) = 0.16 \times 10^{-3} \text{kg m}^2 \tag{4.12}$$

It is clear that the total moment of inertia of the flywheel (J_f) is the sum of that of the support, ring and sliders, i.e.

$$J_f = J_{su} + J_{ri} + J_s \tag{4.13}$$

When the flywheel is rotating at a very low speed shown in Figure 4.5(a), the displacements of the sliders are almost zero. According to the dimensions shown in Figure 4.1, in this case the distance between the mass center of the slider and that of the flywheel is γ=22.5mm. As the sliders are approximately cylindrical, the total moment of inertia of the sliders J_s is given by (Serway 1986)

$$J_s = \frac{1}{12} M_s(\frac{3}{4} d_s^{\,2} + h_s^{\,2}) + M_s \gamma^2 \tag{4.14}$$

where d_s is the diameter of the base area of the sliders and h_s is the height of the sliders.

From Figure 4.1, d_s=20mm, h_s=15mm. Therefore

$$J_s = J_{s\min} = 0.8\times10^{-4}\,\text{kg m}^2 \tag{4.15}$$

When the flywheel is rotating at a very high speed shown in Figure 4.5(b), the displacements of the sliders (γ) is nearly 15mm. According to the dimensions shown in Figure 4.1, the distance between the mass center of the slider and that of the flywheel is γ=37.5mm. Therefore

$$J_s = J_{s\max} = 2\times10^{-4}\,\text{kg m}^2 \tag{4.16}$$

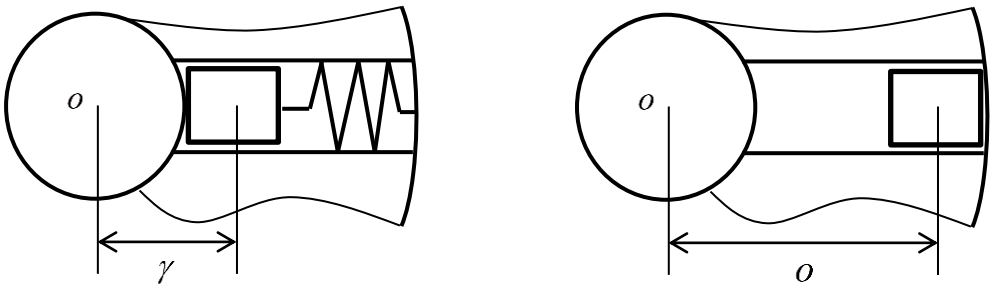

(a) (b)

Figure 4.5. Locations of the sliders in the flywheel at different rotating velocities: (a) low speed, and (b) high speed

Based on Equation (4.13), the moment of inertia of the flywheel varies between the maximum $J_{f\max}$ and minimum $J_{f\min}$ depending the rotational velocity, i.e.

$$J_f = J_{su} + J_{ri} + J_s = J_{su} + J_{ri} + \frac{1}{12}M_s(\frac{3}{4}d_s^{\,2} + h_s^{\,2}) + M_s\gamma^2 \tag{4.17}$$

After substituting J_{su}, J_{ri}, M_s, d_s and h_s into Equation (4.18), J_f becomes the function of γ shown in Figure 4.3, i.e.

$$J_f = (8.2\times10^{-4} + 0.140\gamma^2)\,\text{kg m}^2 \tag{4.18}$$

In our case, $J_{f\max}$ and minimum $J_{f\min}$ are respectively

$$\begin{cases} J_{f\min} = 10.2\times10^{-4}\,\text{kg m}^2 \\ J_{f\max} = 9.0\times10^{-4}\,\text{kg m}^2 \end{cases} \tag{4.19}$$

where the range of γ is from 22.5mm to 37.5mm.

The relationship between the moment of inertia of the VMI flywheel and the distance from the mass center of the sliders to that of the flywheel is shown in Figure 4.6.

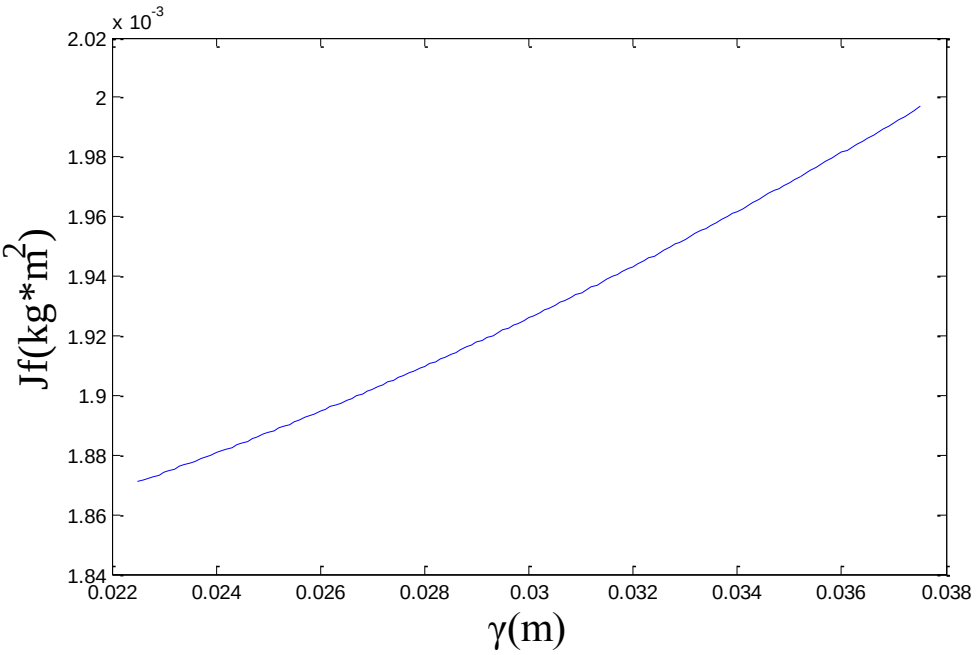

Figure 4.6. Relationship between the moment of inertia of the VMI flywheel and the distance from the mass center of the sliders to that of the flywheel

According to Equation (3.56), the inertance of the system with VMI flywheel is

$$b = J\frac{A^2}{n^2} \tag{4.20}$$

The inertance of the system with the VMI flywheel varies between the maximum and minimum values, i.e. (according to Equations (4-1) and (4-17)),

$$b \in \left(J_{f\min}\frac{A^2}{n^2}, J_{f\max}\frac{A^2}{n^2} \right) \approx (937.2\text{kg}, 1041.3\text{kg}) \tag{4.21}$$

4.1.2.2. CMI flywheel

The mass of the CMI flywheel shown in Figure 4.3 is 0.7kg and the radius is 0.045m. The constant moment of inertia of the flywheel in this case is

$$J_c = \frac{1}{2} m_c r^2 = 7.01 \times 10^{-4} \text{kg m}^2 \tag{4.22}$$

Substituting Equation (4.22) into Equation (4.20), the inertance of the CMI flywheel is given as

$$b = J_c \frac{A^2}{n^2} = 364.7 \text{kg} \tag{4.23}$$

4.2. Experimental Procedure

1. The two-terminal hydraulic prototype was first clamped on the MTS 810 test machine without a flywheel. Then a sinusoidal displacement excitation (200 circles) was input to the system to warm up the text machine and prototype.

2. The encoder was then mounted on the flywheel shaft (without flywheel) (Figure 4.7) to measure the angular velocity of the flywheel shaft to show the backlash of the two-terminal hydraulic system. The encoder was connected to an NI DAQ to collect the data of angular velocity. The data was saved in a PC. The sampling rate for the encoder output is set at 300Hz, the resolution of the encoder is 360/1024 degree, and the theoretical transmission ratio of the prototype is 41degree/mm.

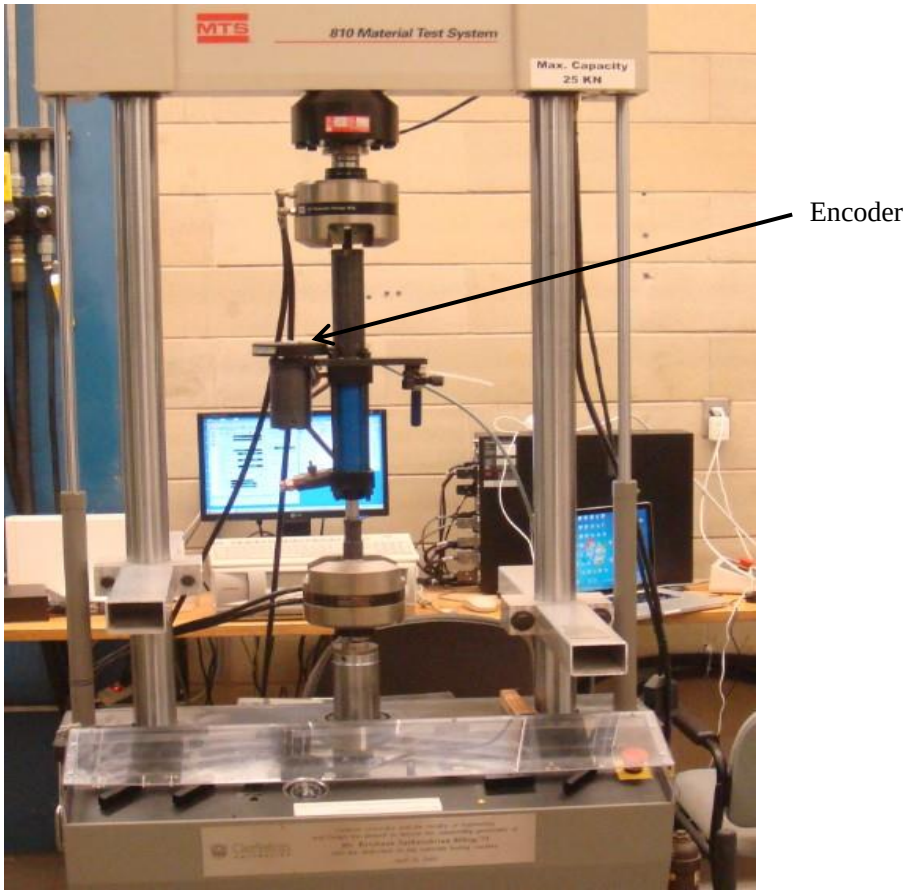

Figure 4.7. Testing setup with the encoder

3. For the CMI tests, the CMI flywheel was installed on the flywheel shaft as shown in Figure 4.8. The aim is to test the performance of the two-terminal hydraulic system with a CMI flywheel. As calculated by Equation (4.23), the inertance of the CMI flywheel is 364.7kg and the sampling rate for the test machine is set at 2048 samples/second.

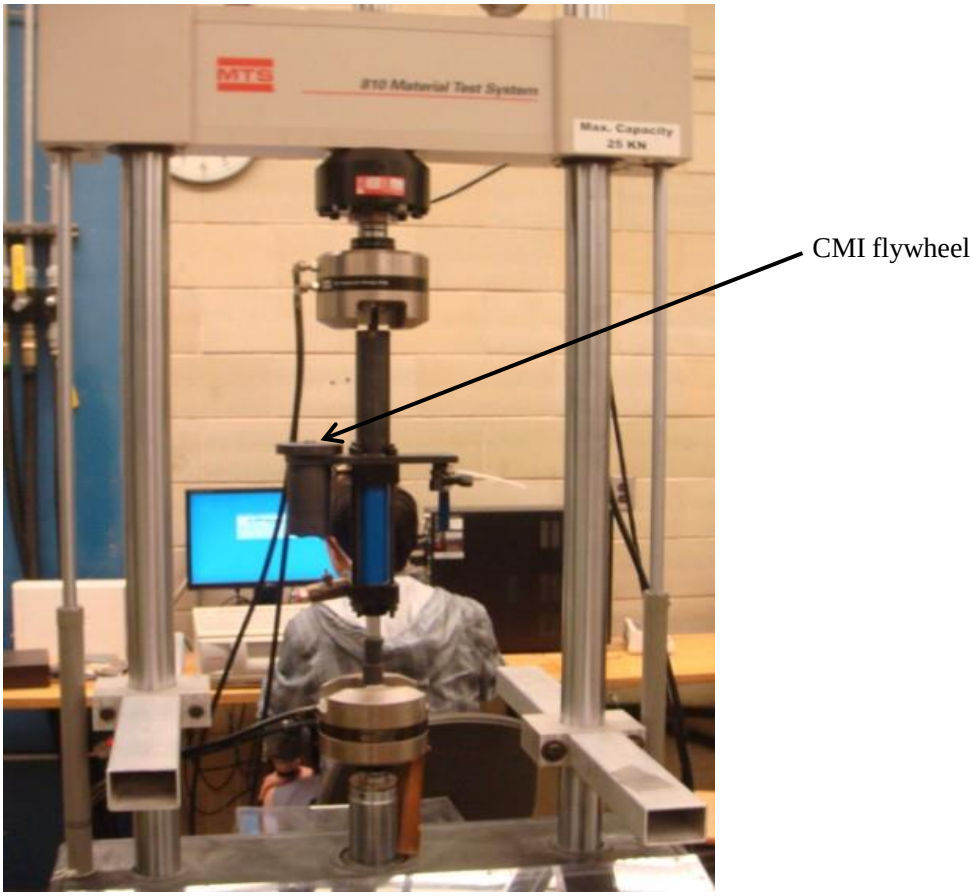

Figure 4.8. Testing setup with the CMI flywheel

4. The variable moment of inertia flywheel was fixed on the flywheel shaft to test the performance of the two-terminal hydraulic system under the following conditions:
    1. System with the VMI flywheel,
    2. System with the VMI flywheel of the maximum moment of inertia, and
    3. System with the VMI flywheel of the minimum moment of inertia

4.3. Experimental Results

4.3.1. One-degree-of-freedom Experimental System

Figure 4.9 shows the one-degree-of-freedom model of the testing system with different

kinds of flywheels shown in Figure 4.3.

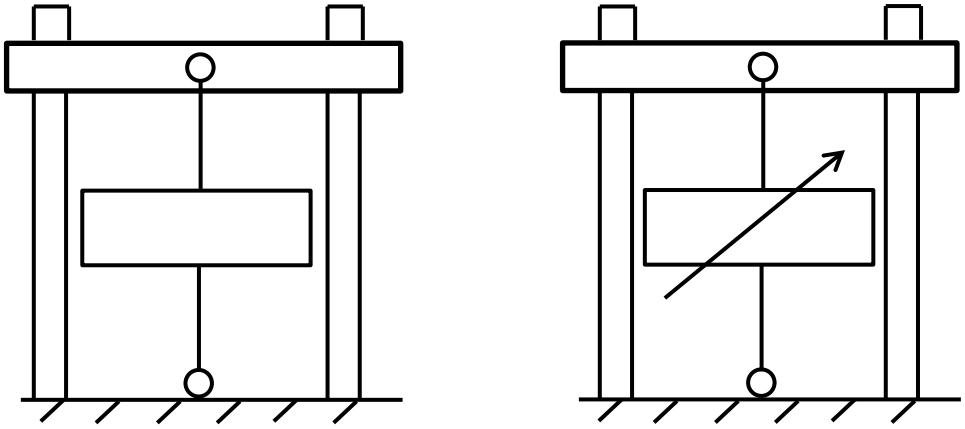

(a) Testing system with CMI flywheel (b) Testing system with VMI flywheel

Figure 4.9. One-degree-of-freedom models of the testing system

4.3.2. Collected data

In this section, the collected data will be presented in five groups. They are corresponding to the tests of the prototype with: (1) CMI flywheel, (2) VMI flywheel (both sinusoidal and triangular inputs), (3) VMI flywheel with the maximum moment of inertia, (4) VMI flywheel with minimum moment of inertia, and (5) encoder (no flywheel). For group (2), both sinusoidal and triangular input excitations are used but for the other four groups only sinusoidal input is used. The reason is that the slider location changes in group (2) tests. The velocity of the triangular excitation is constant in a half cycle. It can help us to determine the displacement range of the sliders in group (2). For the other 4 groups, the slider locations are fixed and hence only the sinusoidal inputs are used. The data files are summarized Table 4.1 to 4.5. All the data are in “txt” format.

The range of amplitudes is from 3 to 15 mm and that of the input frequencies is 0.05 to 10 Hz since the maximum displacement in a typical suspension is from -15 to 15 mm and the MTS 810 machine cannot handle any frequencies that are above 3 Hz if the

amplitude is 15 mm. Some tests beyond this range are also done as shown in bold in Tables 4.1 and 4.5. However, the results are not meaningful because the MTS 810 test machine simply cannot perform properly for tests with such frequencies and amplitudes. Nevertheless, such results could be used to study the backlash effects in future.

The frequency range of the triangular excitations for the VMI flywheel, the VMI flywheel with the maximum and minimum moments of inertia is from 0.1 to 2 Hz because, at such low frequencies, the sliders get sufficient time to move from end to end of the tracks. The amplitude range of the triangular excitations for VMI flywheel is from 10 to 15 mm since for the amplitude lower than 10 mm and frequency lower than 0.1 Hz, the responses are almost the same as that for the sinusoidal excitation.

The frequency of the triangular excitations given to the encoder is only 0.5 Hz because it is only required to calculate the frictional resistance of the hydraulic prototype.

Table 4.1. Data collected from the system with the CMI flywheel (sinusoidal excitation)

A(mm) / *f* (Hz)	3	5	8	10	15
0.05	*CF-sin3-0.05*	CF-sin5-0.05	*CF-sin8-0.05*	CF-sin10-0.05	*CF-sin15-0.05*
0.1	CF-sin3-0.1	CF-sin5-0.1	CF-sin8-0.1	CF-sin10-0.1	CF-sin15-0.1
0.2	*CF-sin3-0.2*	CF-sin5-0.2	*CF-sin8-0.2*	CF-sin10-0.2	*CF-sin15-0.2*
0.5	CF-sin3-0.5	CF-sin5-0.5	CF-sin8-0.5	CF-sin10-0.5	CF-sin15-0.5
1	CF-sin3-1	CF-sin5-1	CF-sin8-1	CF-sin10-1	CF-sin15-1
2	*CF-sin3-2*	CF-sin5-2	*CF-sin8-2*	CF-sin10-2	*CF-sin15-2*
5	**CF-sin3-5**	**CF-sin5-5**	**CF-sin8-5**	**CF-sin10-5**	**CF-sin15-5**
10	**CF-sin3-10**	**CF-sin5-10**	**CF-sin8-10**	**CF-sin10-10**	**CF-sin15-10**

Note: The tests in bold means the cases that the testing system cannot handle.

Table 4.2(a). Data collected from the system with the VMI flywheel (sinusoidal excitation)

A(mm) / *f* (Hz)	3	5	8	10	15
0.1	*VF-sin3-0.1*	VF-sin5-0.1	*VF-sin8-0.1*	VF-sin10-0.1	*VF-sin15-0.1*
0.2	VF-sin3-0.2	VF-sin5-0.2	VF-sin8-0.2	VF-sin10-0.2	VF-sin15-0.2
0.3	VF-sin3-0.3	VF-sin5-0.3	VF-sin8-0.3	VF-sin10-0.3	VF-sin15-0.3
0.4	VF-sin3-0.4	VF-sin5-0.4	VF-sin8-0.4	VF-sin10-0.4	VF-sin15-0.4
0.5	*VF-sin3-0.5*	VF-sin5-0.5	*VF-sin8-0.5*	VF-sin10-0.5	*VF-sin15-0.5*
0.6	VF-sin3-0.6	VF-sin5-0.6	VF-sin8-0.6	VF-sin10-0.6	VF-sin15-0.6
0.7	VF-sin3-0.7	VF-sin5-0.7	VF-sin8-0.7	VF-sin10-0.7	VF-sin15-0.7
0.8	VF-sin3-0.8t	VF-sin5-0.8	VF-sin8-0.8	VF-sin10-0.8	VF-sin15-0.8
0.9	VF-sin3-0.9	VF-sin5-0.9	VF-sin8-0.9	VF-sin10-0.9	VF-sin15-0.9
1	*VF-sin3-1*	VF-sin5-1	*VF-sin8-1*	VF-sin10-1	*VF-sin15-1*
2	*VF-sin3-2*	VF-sin5-2	*VF-sin8-2*	VF-sin10-2	*VF-sin15-2*

Table 4.2(b). Data collected from the system with the VMI flywheel (triangular excitation)

A(mm) / *f* (Hz)	10	15
0.1	VF-tri10-0.1	*VF-tri15-0.1*
0.2	VF-tri10-0.2	VF-tri15-0.2
0.3	VF-tri10-0.3	VF-tri15-0.3
0.4	VF-tri10-0.4	VF-tri15-0.4
0.5	VF-tri10-0.5	*VF-tri15-0.5*
0.6	VF-tri10-0.6	VF-tri15-0.6
0.7	VF-tri10-0.7	VF-tri15-0.7
0.8	VF-tri10-0.8	VF-tri15-0.8
0.9	VF-tri10-0.9	VF-tri15-0.9
1	VF-tri10-1	*VF-tri15-1*
2	VF-tri10-2	*VF-tri15-2*

Table 4.3. Data collected from the system with the VMI flywheel of the maximum moment of inertia (sinusoidal excitation)

A(mm) / *f* (Hz)	3	5	8	10	15
0.1	*VFMax-sin3-0.1*	VFMax-sin5-0.1	*VFMax-sin8-0.1*	VFMax-sin10-0.1	*VFMax-sin15-0.1*
0.2	VFMax-sin3-0.2	VFMax-sin5-0.2	VFMax-sin8-0.2	VFMax-sin10-0.2	VFMax-sin15-0.2
0.3	VFMax-sin3-0.3	VFMax-sin5-0.3	VFMax-sin8-0.3	VFMax-sin10-0.3	VFMax-sin15-0.3
0.4	VFMax-sin3-0.4	VFMax-sin5-0.4	VFMax-sin8-0.4	VFMax-sin10-0.4	VFMax-sin15-0.4
0.5	*VFMax-sin3-0.5*	VFMax-sin5-0.5	*VFMax-sin8-0.5*	VFMax-sin10-0.5	*VFMax-sin15-0.5*
0.6	VFMax-sin3-0.6	VFMax-sin5-0.6	VFMax-sin8-0.6	VFMax-sin10-0.6	VFMax-sin15-0.6
0.7	VFMax-sin3-0.7	VFMax-sin5-0.7	VFMax-sin8-0.7	VFMax-sin10-0.7	VFMax-sin15-0.7
0.8	VFMax-sin3-0.8	VFMax-sin5-0.8	VFMax-sin8-0.8	VFMax-sin10-0.8	VFMax-sin15-0.8
0.9	VFMax-sin3-0.9	VFMax-sin5-0.9	VFMax-sin8-0.9	VFMax-sin10-0.9	VFMax-sin15-0.9
1	*VFMax-sin3-1*	VFMax-sin5-1	*VFMax-sin8-1*	VFMax-sin10-1	*VFMax-sin15-1*
2	*VFMax-sin3-2*	VFMax-sin5-2	*VFMax-sin8-2*	VFMax-sin10-2	*VFMax-sin15-2*

Table 4.4. Data collected from the system with the VMI flywheel of the minimum moment of inertia (sinusoidal excitation)

A(mm) / *f* (Hz)	3	5	8	10	15
0.1	*VFMin-sin3-0.1*	VFMin-sin5-0.1	*VFMin-sin8-0.1*	VFMin-sin10-0.1	*VFMin-sin15-0.1*
0.2	VFMin-sin3-0.2	VFMin-sin5-0.2	VFMin-sin8-0.2	VFMin-sin10-0.2	VFMin-sin15-0.2
0.3	VFMin-sin3-0.3	VFMin-sin5-0.3	VFMin-sin8-0.3	VFMin-sin10-0.3	VFMin-sin15-0.3
0.4	VFMin-sin3-0.4	VFMin-sin5-0.4	VFMin-sin8-0.4	VFMin-sin10-0.4	VFMin-sin15-0.4
0.5	*VFMin-sin3-0.5*	VFMin-sin5-0.5	*VFMin-sin8-0.5*	VFMin-sin10-0.5	*VFMin-sin15-0.5*
0.6	VFMin-sin3-0.6	VFMin-sin5-0.6	VFMin-sin8-0.6	VFMin-sin10-0.6	VFMin-sin15-0.6
0.7	VFMin-sin3-0.7	VFMin-sin5-0.7	VFMin-sin8-0.7	VFMin-sin10-0.7	VFMin-sin15-0.7
0.8	VFMin-sin3-0.8	VFMin-sin5-0.8	VFMin-sin8-0.8	VFMin-sin10-0.8	VFMin-sin15-0.8
0.9	VFMin-sin3-0.9	VFMin-sin5-0.9	VFMin-sin8-0.9	VFMin-sin10-0.9	VFMin-sin15-0.9
1	*VFMin-sin3-1*	VFMin-sin5-1	*VFMin-sin8-1*	VFMin-sin10-1	*VFMin-sin15-1*
2	*VFMin-sin3-2*	VFMin-sin5-2	*VFMin-sin8-2*	VFMin-sin10-2	*VFMin-sin15-2*

Table 4.5. Data collected from the system with the encoder but without flywheel (sinusoidal excitation)

A(mm) / *f* (Hz)	3	5	8	10	15
0.05	Enco-sin3-0.05	Enco-sin5-0.05	Enco-sin8-0.05	Enco-sin10-0.05	Enco-sin15-0.05
0.1	Enco-sin3-0.1	Enco-sin5-0.1	Enco-sin8-0.1	Enco-sin10-0.1	Enco-sin15-0.1
0.2	Enco-sin3-0.2	Enco-sin5-0.2	Enco-sin8-0.2	*Enco-sin10-0.2*	Enco-sin15-0.2
0.5	Enco-sin3-0.5	Enco-sin5-0.5	Enco-sin8-0.5	Enco-sin10-0.5	Enco-sin15-0.5
1	Enco-sin3-1	Enco-sin5-1	Enco-sin8-1.	Enco-sin10-1	Enco-sin15-1
2	Enco-sin3-2	Enco-sin5-2	Enco-sin8-2	Enco-sin10-2	Enco-sin15-2
5	**Enco-sin3-5**	**Enco-sin5-5**	**Enco-sin8-5**	**Enco-sin10-5**	**Enco-sin15-5**
10	**Enco-sin3-10**	**Enco-sin5-10**	**Enco-sin8-10**	**Enco-sin10-10**	**Enco-sin15-10**

4.3.3. Results and observations

For our tests, the test machine is set to displacement control. For a low sinusoidal frequency (below 5 Hz) input, the actual displacement is equal to the ideal input sine wave, but for a sinusoidal input with a higher frequency the PIC control can no longer generate an ideal sine wave. In view of this, all the tests are limited to the range that the test machine can handle. That means the actual displacement is equal to the ideal input displacement excitation. By the way, the backlash only affects the angular displacement of the flywheel instead of the displacement of the terminals.

System with the CMI flywheel

Figure 4.10 displays the excitations and force responses of the prototype with the CMI flywheel from some representative datasets (in italic) the in Table 4.1. Note that none of the datasets with frequency higher than 2 Hz are plotted because the test machine cannot follow the high frequency.

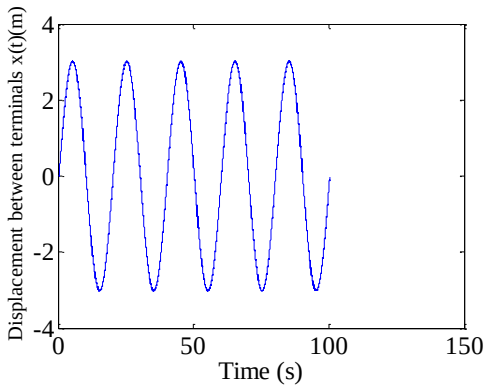

(*a*1) Excitation: 0.003sin(0.1πt)

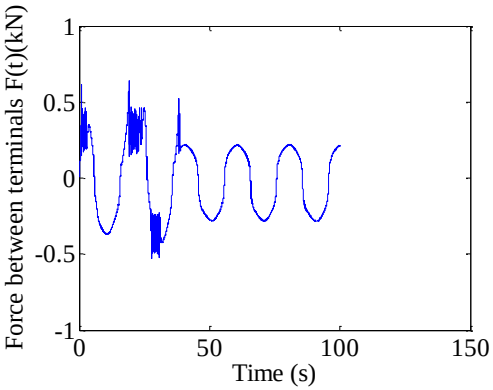

(*a*2) Force *F*(*t*)

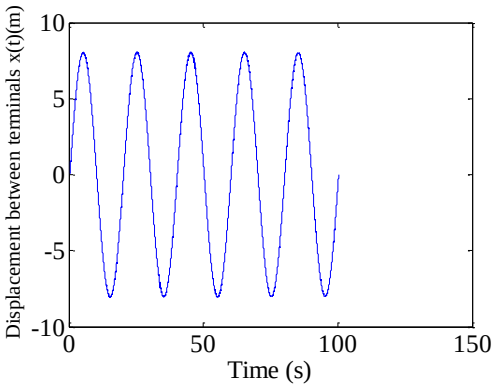

(*b*1) Excitation: 0.008sin(0.1πt)

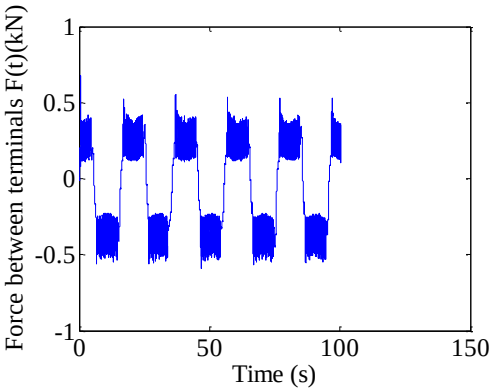

(*b*2) Force *F*(*t*)

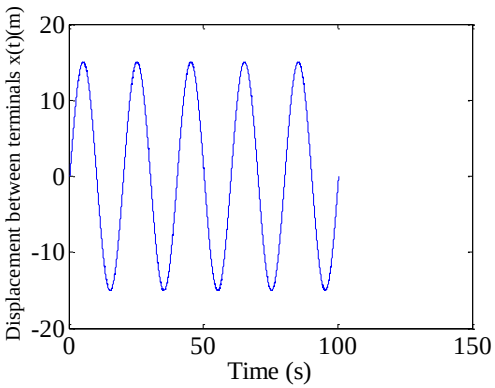

(*c*1) Excitation: 0.015sin(0.1πt)

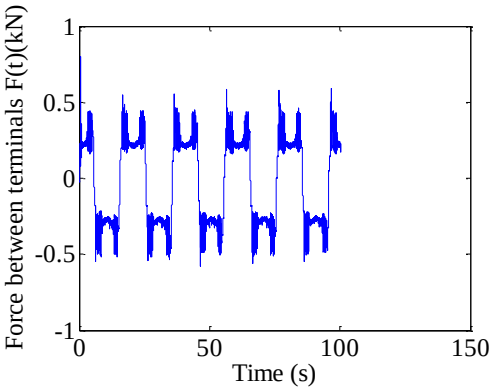

(*c*2) Force *F*(*t*)

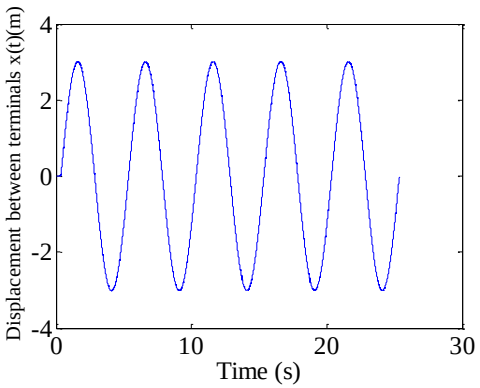

(*d*1) Excitation: 0.003sin(0.4πt)

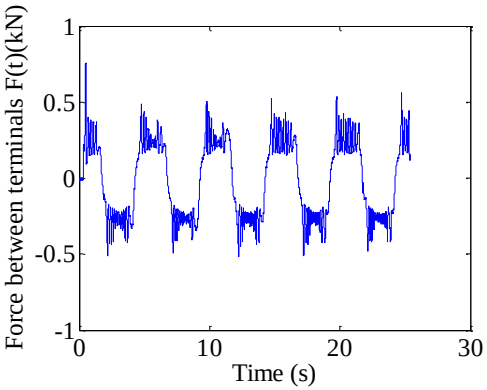

(*d*2) Force *F*(*t*)

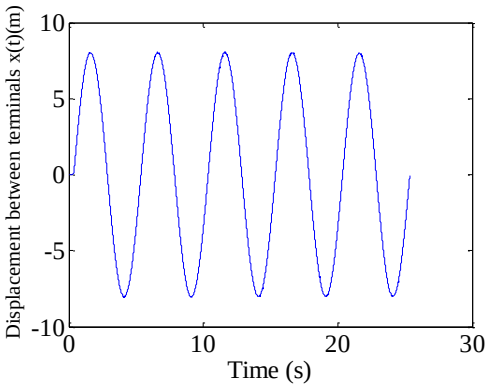

(*e*1) Excitation: 0.008sin(0.4πt)

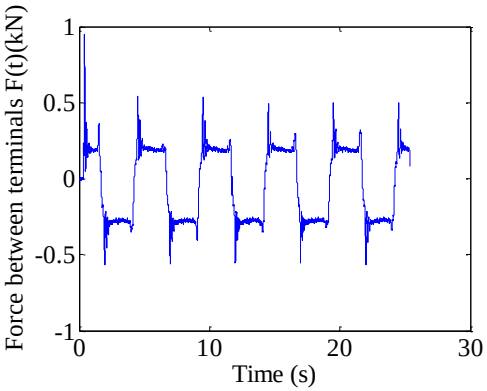

(*e*2) Force *F*(*t*)

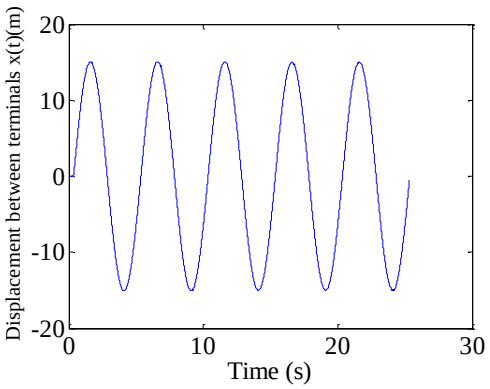

(*f*1) Excitation: 0.015sin(0.4πt)

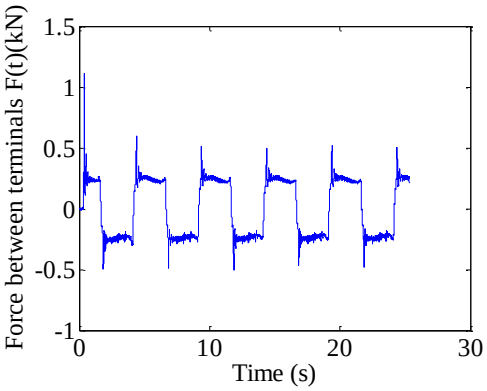

(*f*2) Force *F*(*t*)

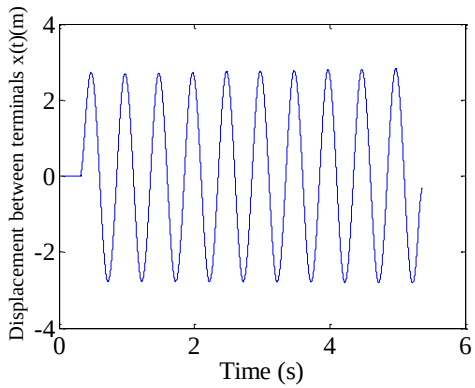

(*g*1) Excitation: 0.003sin(4πt)

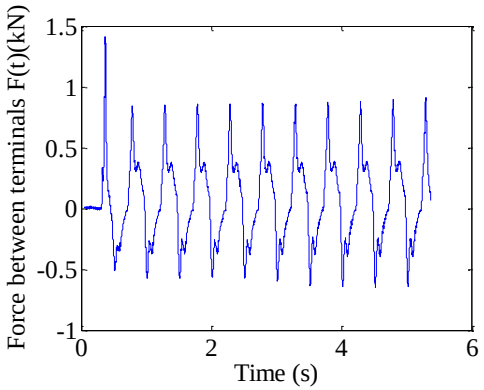

(*g*2) Force *F*(*t*)

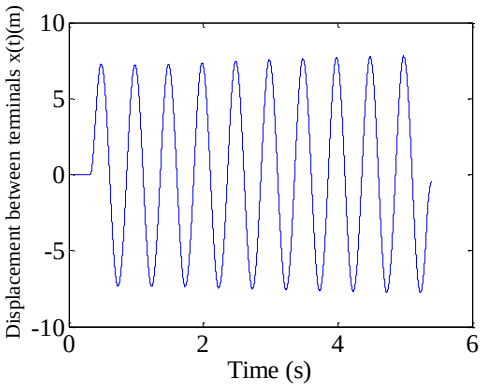

(*h*1) Excitation: 0.08sin(4πt)

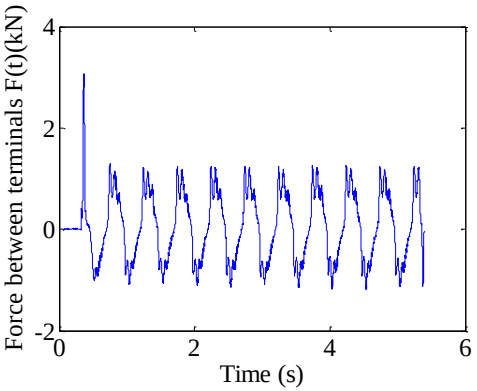

(*h*2) Force *F*(*t*)

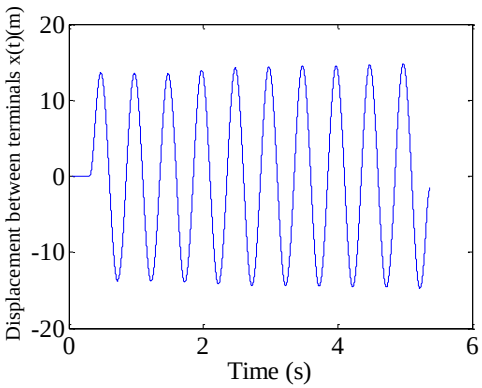

(*i*1) Excitation: 0.015sin(4πt)

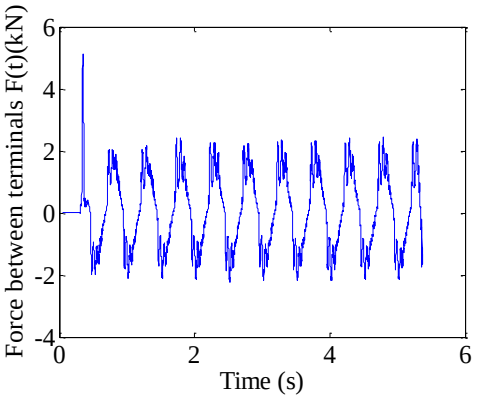

(*i*2) Force *F*(*t*)

Figure 4.10. Force response of the system with the CMI flywheel: *a*1, *b*1, *c*1, *d*1, *e*1, *f*1, *g*1, *h*1, *i*1 are the displacement excitations, and *a*2, *b*2, *c*2, *d*2, *e*2, *f*2, *g*2, *h*2, *i*2 are the associated force responses respectively.

The first force plot (Figure 4.10 *a*2) shows some abnormal behavior in the first two cycles because the test machine was not warmed up. The high spike at beginning of all

the other force plots, i.e., Figures 4.10 *b*2-*i*2 are likely due to the high static friction force. Figures 4.10 *a*2-*i*2 also show that the force between the two terminals increases with the increase in either amplitude or frequency, or in both. The ideal force responses should also be a sinusoidal wave because of the sinusoidal displacement, but the real force responses shown in Figure 4.10 are not. This is likely caused by:

1. The frictional resistance and/or the damping effect in the system,
2. The backlash when the flywheel reverses rotation, and/or
3. The limited stiffness and hence the spring effect of the system.

System with the VMI flywheel

In Figure 4.11, some typical excitations and force responses of the prototype with the VMI flywheel are plotted using several datasets (marked in italic) in Tables 4.2(a) and 4.2(b). Again the plots do not include the data with frequency higher than 2 Hz due to the limited capability of the PID controller.

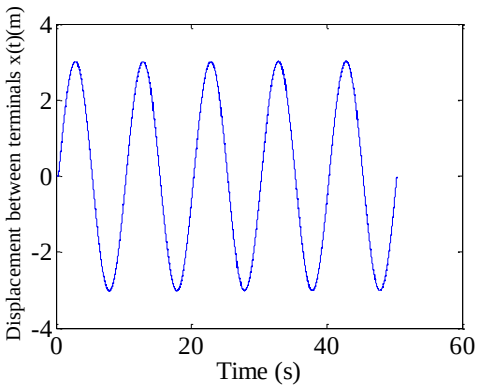

(*a*1) Excitation: $x(t)=0.003\sin(0.2\pi t)$

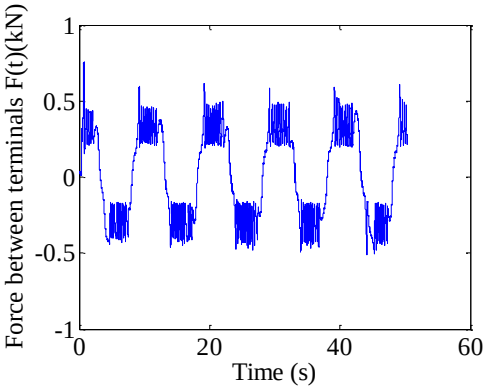

(*a*2) Force $F(t)$

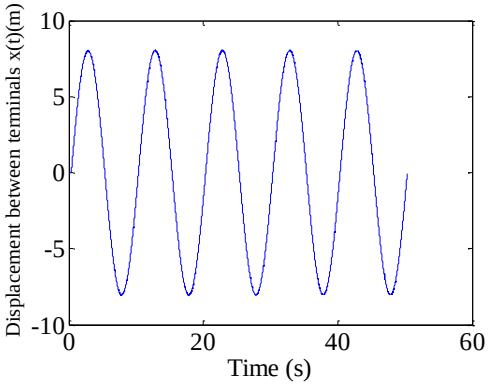

(*b*1) Excitation: $x(t)=0.008\sin(0.2\pi t)$

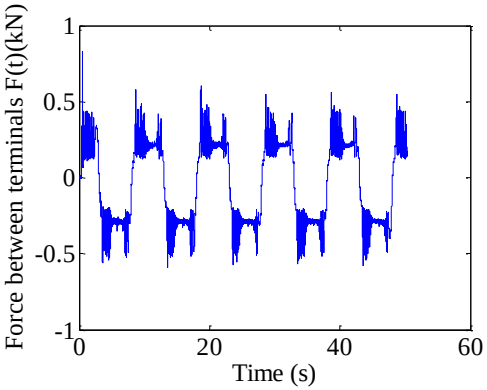

(*b*2) Force $F(t)$

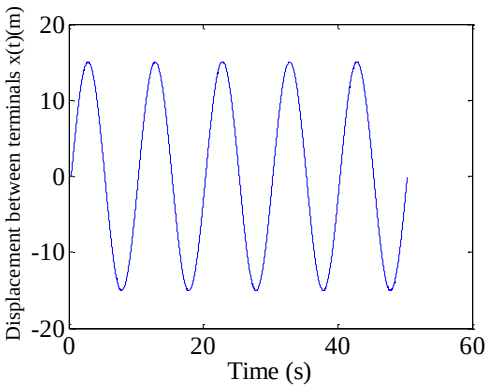

(*c*1) Excitation: $x(t)=0.015\sin(0.2\pi t)$

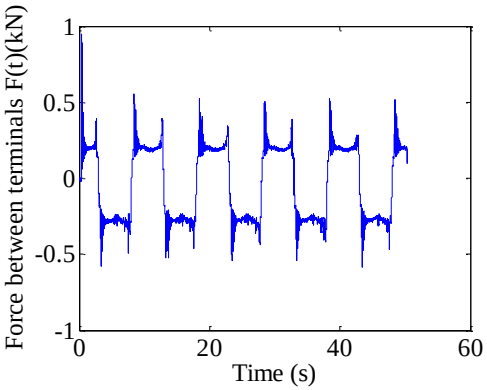

(*c*2) Force $F(t)$

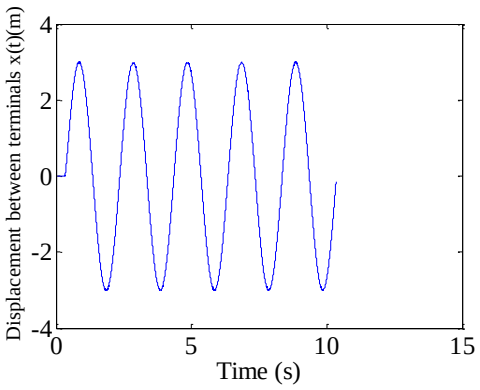

(*d*1) Excitation: $x(t)=0.003\sin(\pi t)$

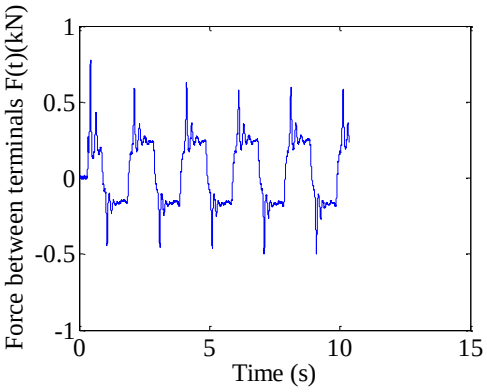

(*d*2) Force $F(t)$

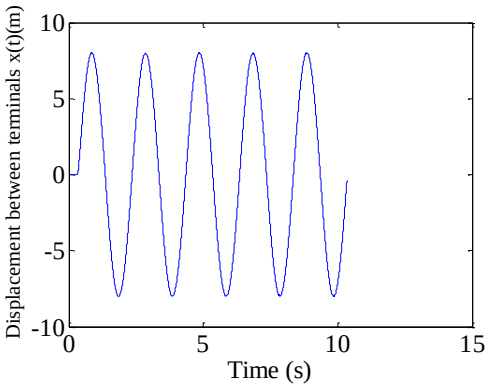

(*e*1) Excitation: $x(t)=0.008\sin(\pi t)$

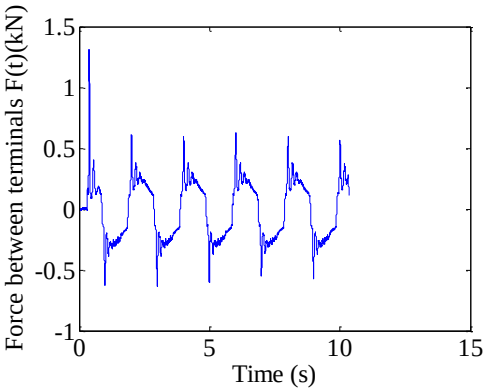

(*e*2) Force $F(t)$

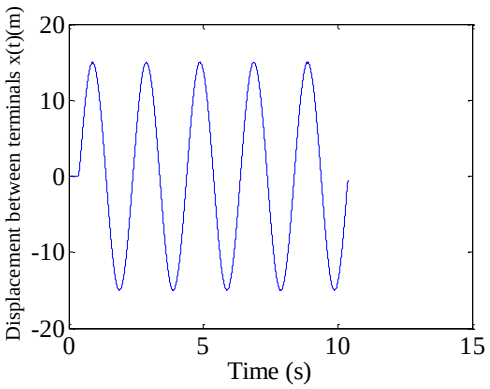

(*f*1) Excitation: $x(t)=0.015\sin(\pi t)$

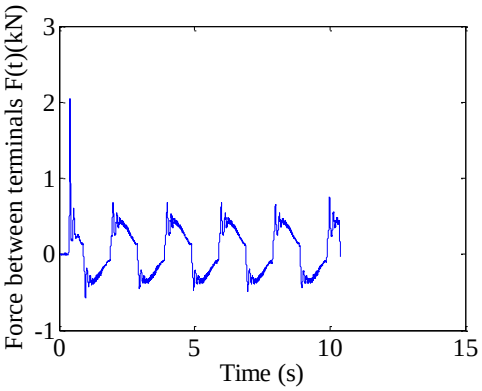

(*f*2) Force $F(t)$

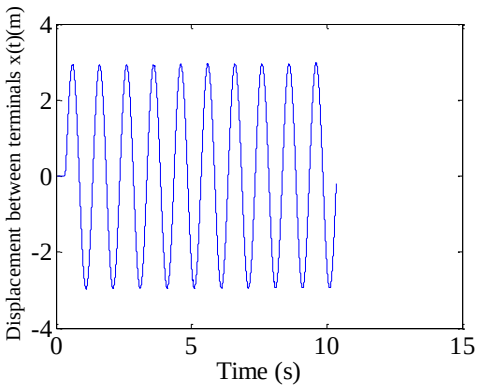

(*g*1) Excitation: $x(t)=0.003\sin(2\pi t)$

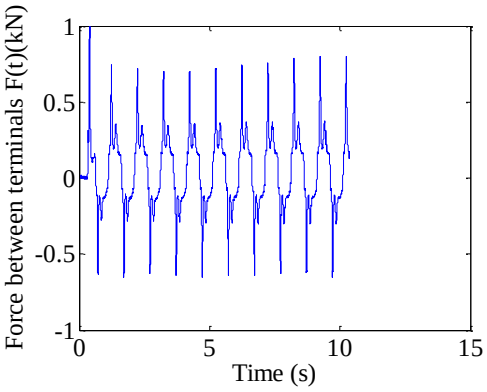

(*g*2) Force $F(t)$

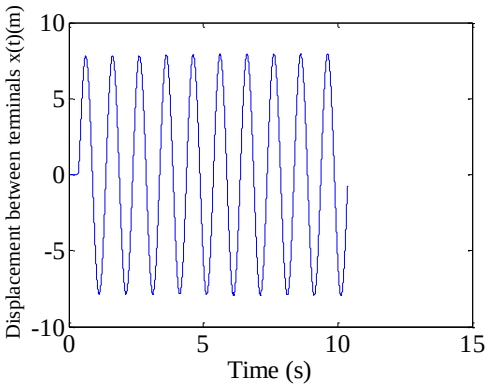

(*h*1) Excitation: $x(t)=0.008\sin(2\pi t)$

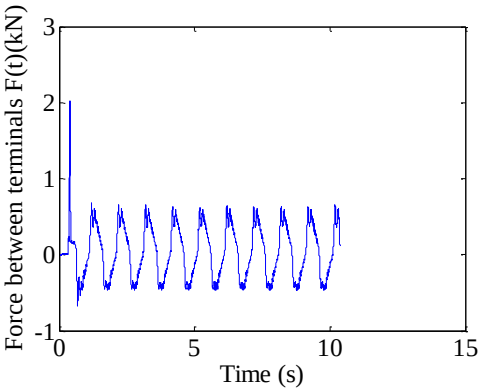

(*h*2) Force $F(t)$

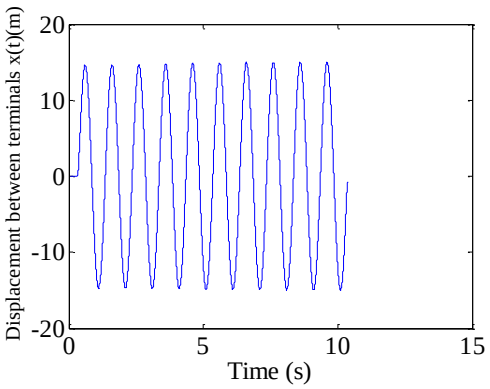

(*i*1) Excitation: $x(t)=0.015\sin(2\pi t)$

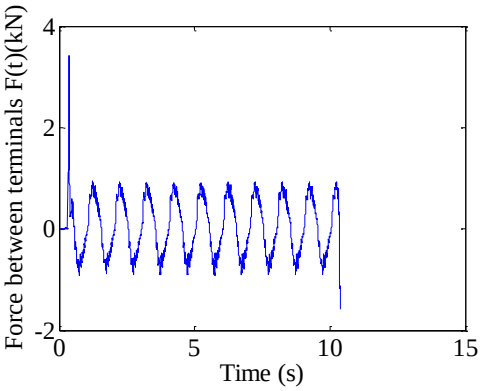

(*i*2) Force $F(t)$

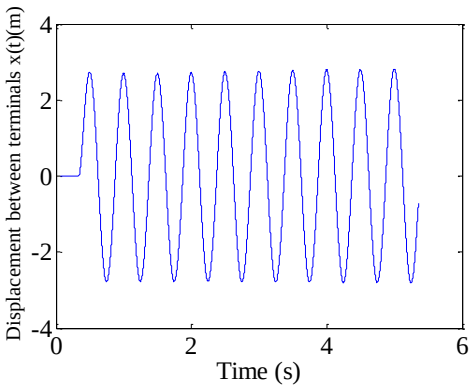

(*j*1) Excitation: $x(t)=0.003\sin(4\pi t)$

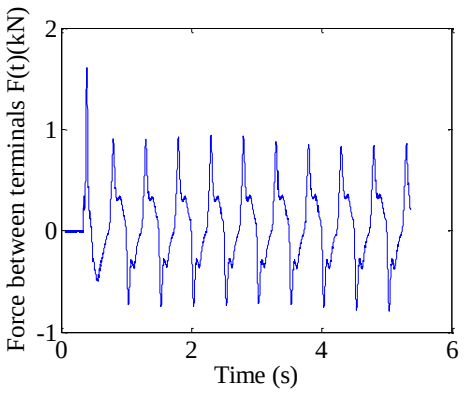

(*j*2) Force $F(t)$

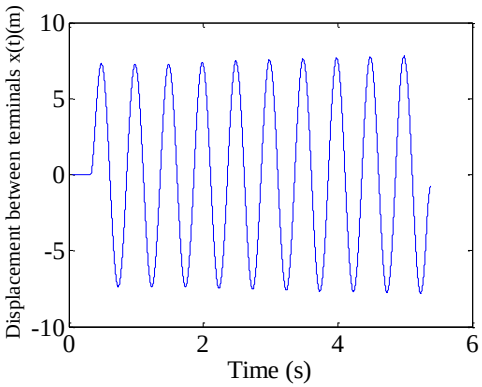

(*k*1) Excitation: $x(t)=0.08\sin(4\pi t)$

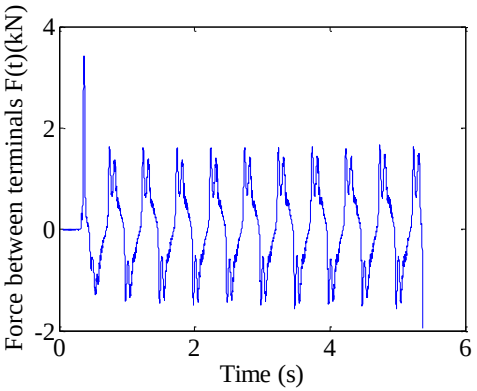

(*k*2) Force $F(t)$

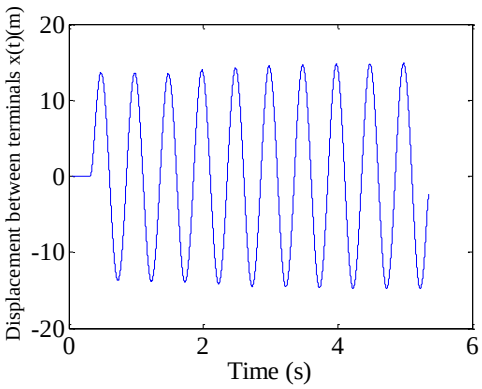

(*l*1) Excitation: $x(t)=0.015\sin(4\pi t)$

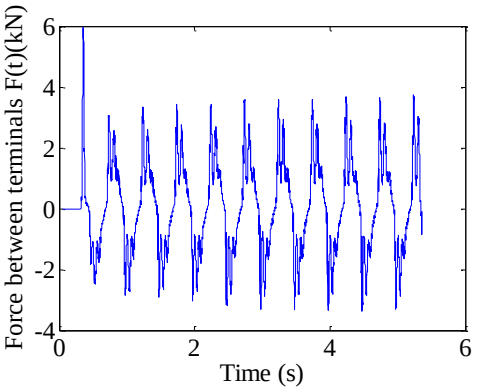

(*l*2) Force $F(t)$

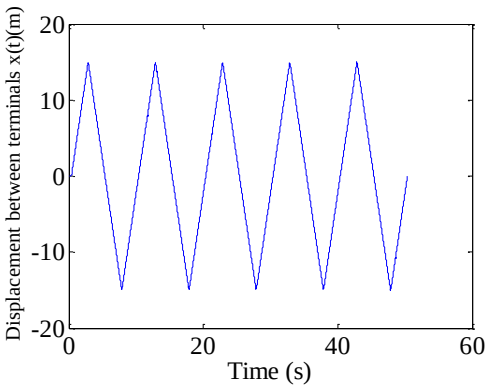

(*m*1)Excitation: Triangular (*A*=0.015m, *f*=0.1Hz)

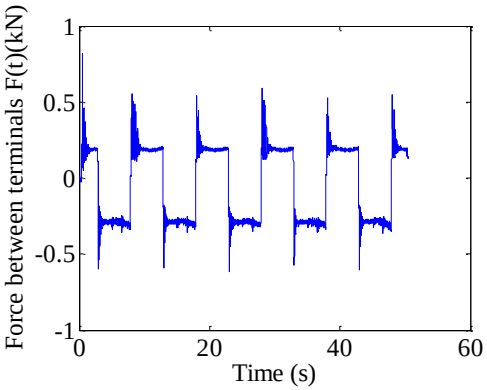

(*m*2)Force *F*(*t*)

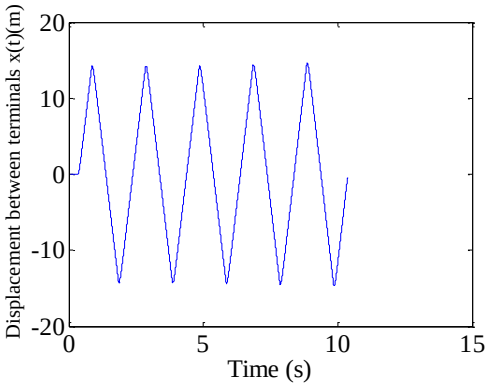

(*n*1)Excitation: Triangular (*A*=0.015m, *f*=0.5Hz)

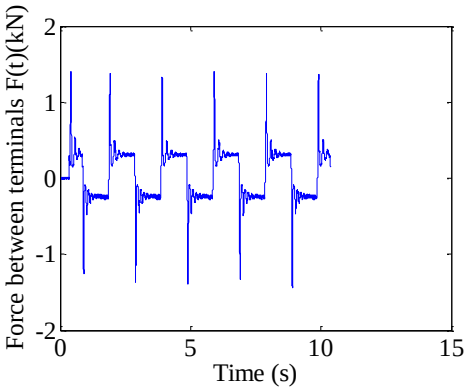

(*n*2)Force *F*(*t*)

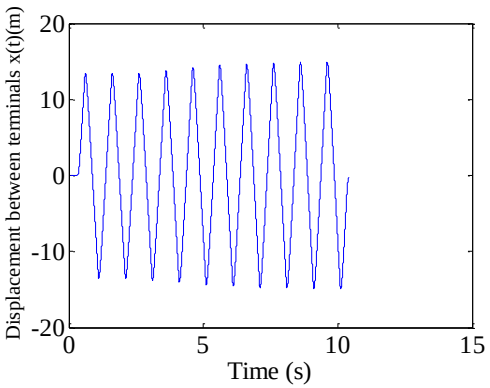

(*o*1)Excitation: Triangular (*A*=0.015m, *f*=1Hz)

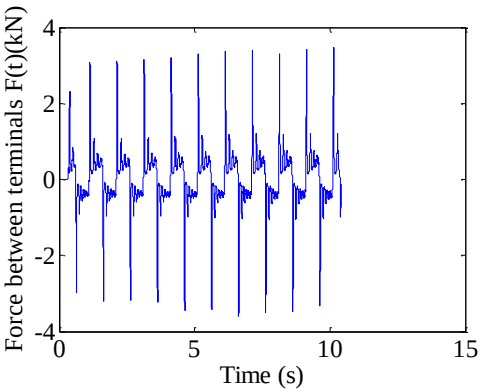

(*o*2)Force *F*(*t*)

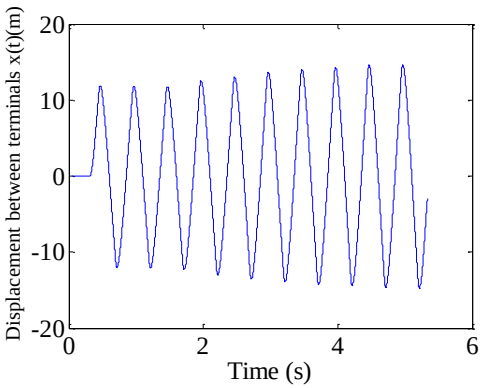

(*p*1)Excitation: Triangular (*A*=0.015m, *f*=2Hz)

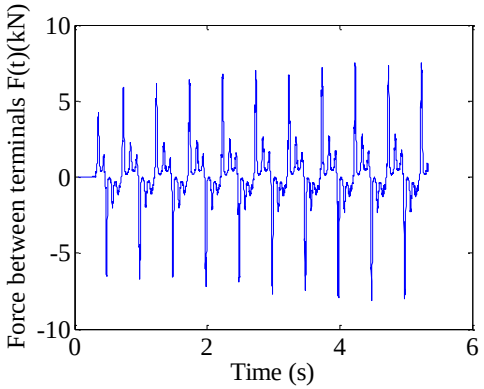

(*p*2)Force *F*(*t*)

Figure 4.11. Force response of the system with the VMI flywheel: *a*1, *b*1, *c*1, *d*1, *e*1, *f*1, *g*1, *h*1, *i*1, *j*1, *k*1, *l*1, *m*1, *n*1, *o*1, *p*1 are the displacement excitations, and *a*2, *b*2, *c*2, *d*2, *e*2, *f*2, *g*2, *h*2, *i*2, *j*2, *k*2, *l*2, *m*2, *n*2, *o*2, *p*2 are the associated force responses respectively.

As mentioned in the tests with the CMI flywheel, the increase in amplitude, or frequency, or both lead to the increased force between the two terminals. For the plots related to sinusoidal inputs, the force responses again do not follow exact sinusoidal pattern due to similar reasons as explained for the CMI cases. Furthermore the force pattern deviates more from sinusoidal pattern because of the variable moment of inertia caused by the moving sliders.

The ideal force responses for the triangular excitations should follow a square pattern because the velocity is constant for each test and the force is determined by the system resistance with slight contribution from damping. The square pattern has been clearly demonstrated when the frequency is low (e.g., 0.1 Hz). When the frequency increases, the force responses to the triangular excitations exhibit greater backlash effect than those to the sinusoidal excitations since the displacement excitation is not a smooth curve at the crest and valley points. It means very high acceleration and high force as shown at the beginning of every half cycle.

The comparisons of the VMI flywheel and the VMI flywheel with maximum and minimum moments of inertia will be discussed next after presenting the force responses of the VMI flywheel with maximum and minimum moments of inertia.

System with the VMI flywheel of the maximum and minimum moment of inertia

Figure 4.12 shows the VMI flywheel with the maximum and minimum moments of inertia.

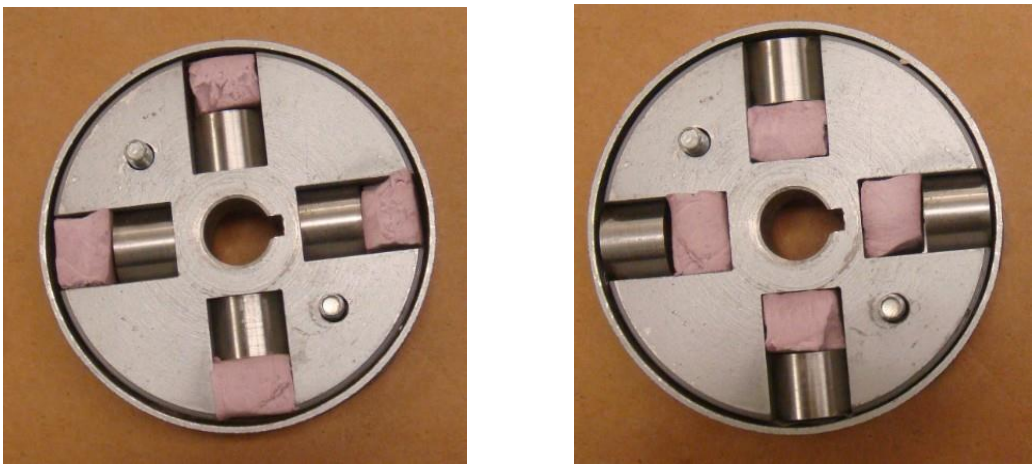

(a) VMI flywheel of the minimum moment of inertia

(b) VMI flywheel of the maximum moment of inertia

Figure 4.12. VMI flywheel with the maximum and minimum moments of inertia

The excitation and force responses of the prototype with the VMI flywheel of the maximum moment of inertia, minimum and variable moment of inertia are presented in Figure 4.13 from representative datasets (marked in italic) in Tables 4.2(a), 4.3 and 4.4.

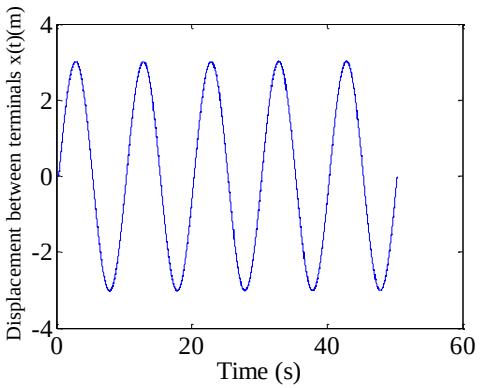

(*a*1) Excitation: $x(t)=0.003\sin(0.2\pi t)$

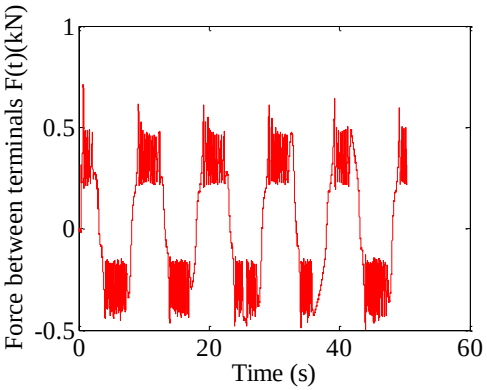

(*a*2) Force response of the VMI flywheel with the maximum MI: $F(t)$

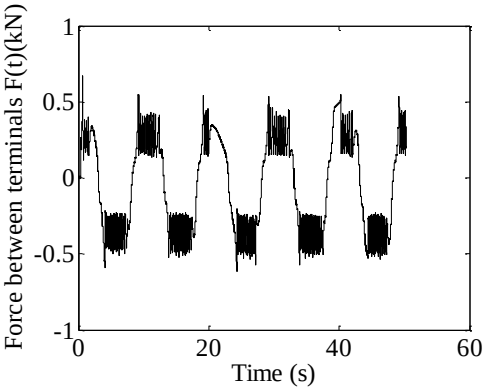

(*a*3) Force response of the VMI flywheel with the minimum MI: $F(t)$

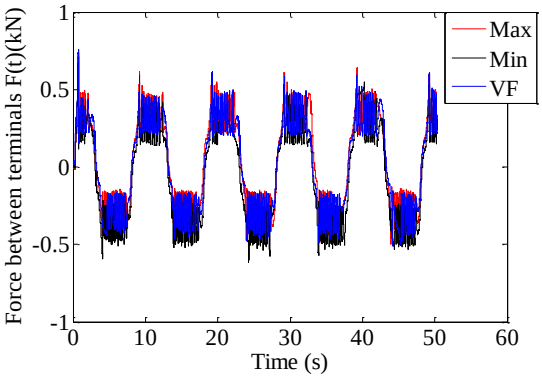

(*a*4)

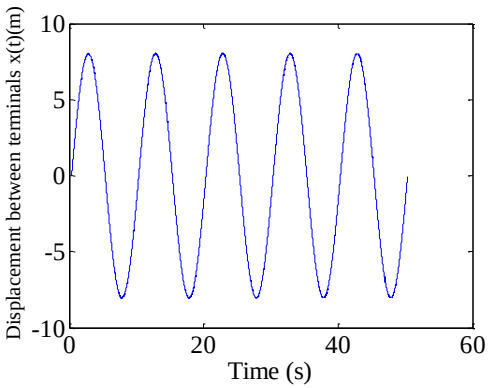

(*b*1) Excitation: $x(t)=0.008\sin(0.2\pi t)$

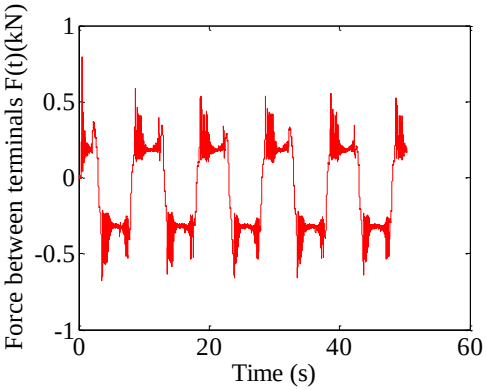

(*b*2) Force response of the VMI flywheel with the maximum MI: $F(t)$

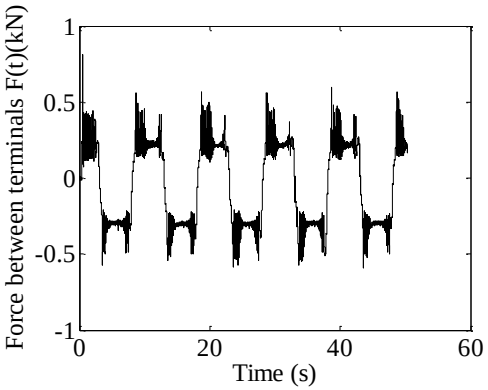

(*b*3) Force response of the VMI flywheel with the minimum MI: $F(t)$

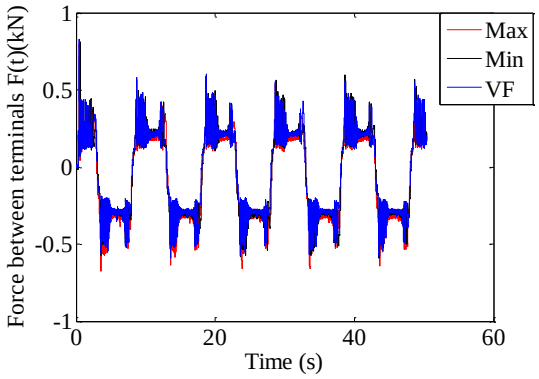

(*b*4)

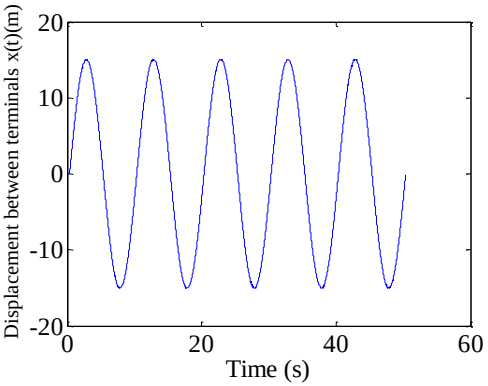

(*c*1) Excitation: $x(t)=0.015\sin(0.2\pi t)$

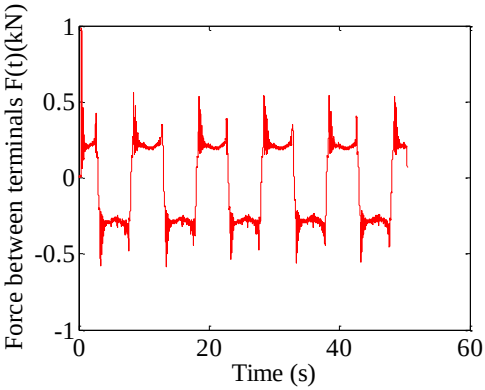

(*c*2) Force response of the VMI flywheel with the maximum MI: $F(t)$

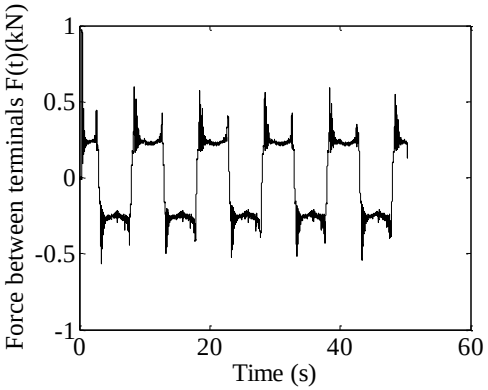

(*c*3) Force response of the VMI flywheel with the minimum MI: $F(t)$

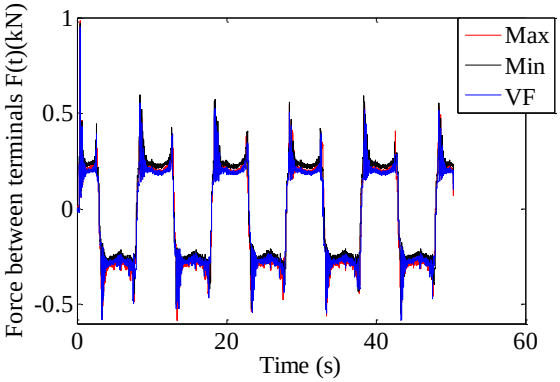

(*c*4)

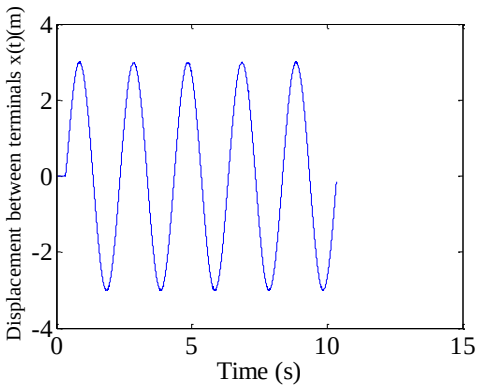

(*d*1) Excitation: $x(t)=0.003\sin(\pi t)$

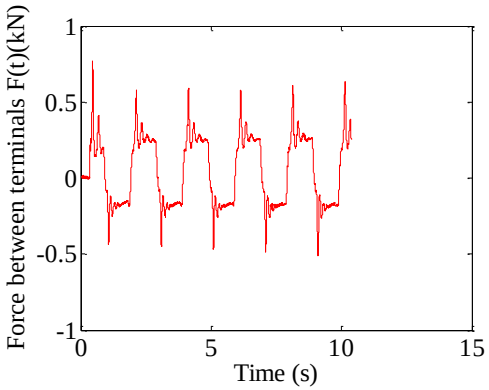

(*d*2) Force response of the VMI flywheel with the maximum MI: $F(t)$

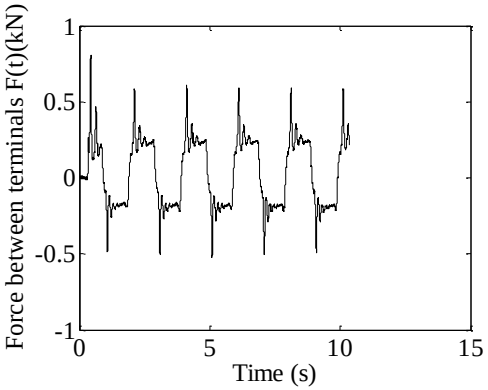

(*d*3) Force response of the VMI flywheel with the minimum MI: $F(t)$

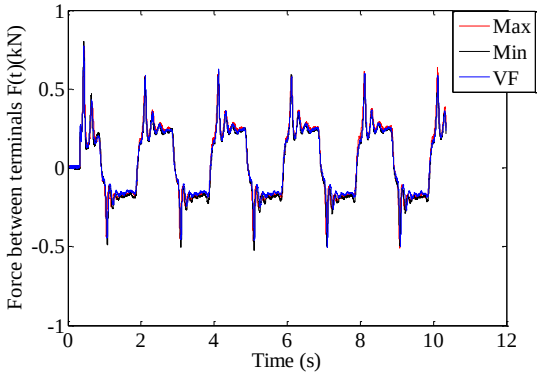

(*d*4)

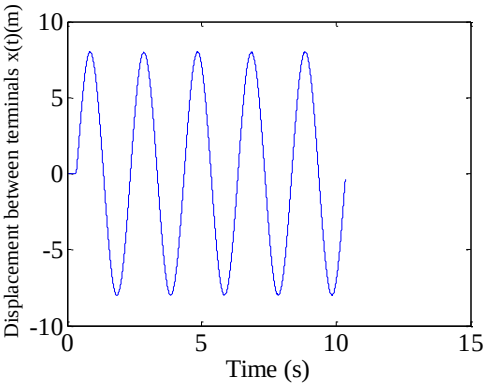

(*e*1) Excitation: $x(t)=0.008\sin(\pi t)$

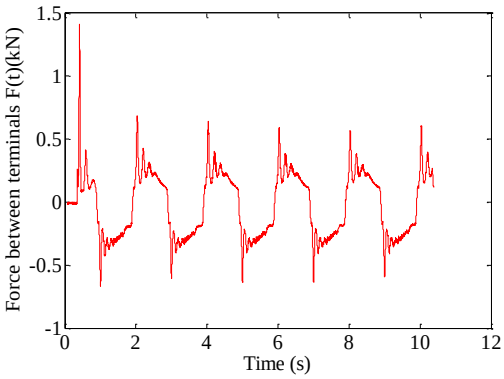

(*e*2) Force response of the VMI flywheel with the maximum MI: $F(t)$

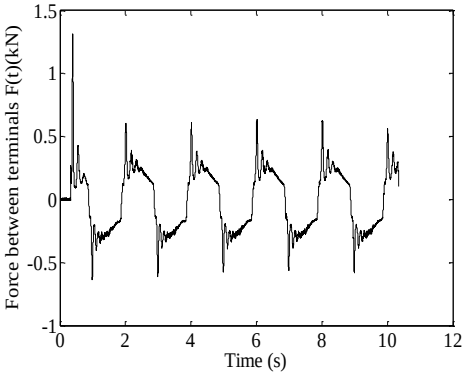

(*e*3) Force response of the VMI flywheel with the minimum MI: $F(t)$

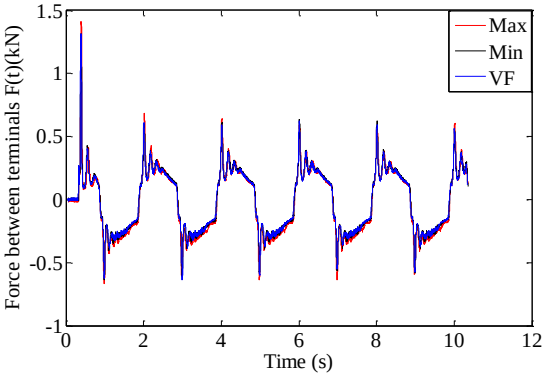

(*e*4)

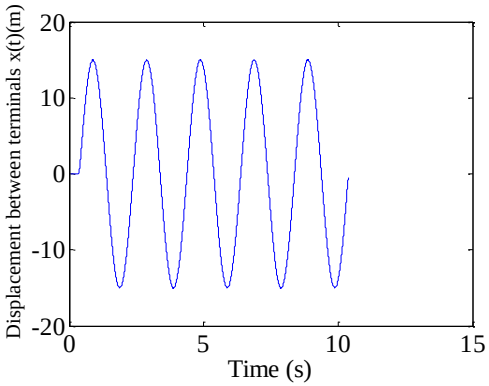

(*f*1) Excitation: $x(t)=0.015\sin(\pi t)$

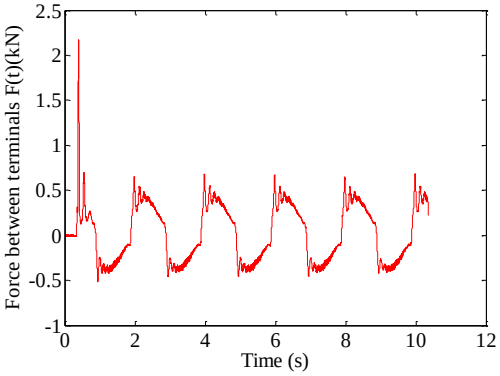

(*f*2) Force response of the VMI flywheel with the maximum MI: $F(t)$

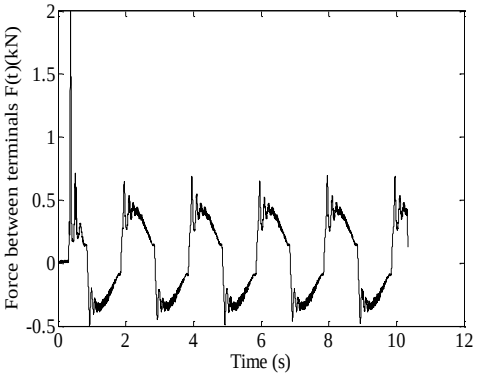

(*f*3) Force response of the VMI flywheel with the minimum MI: $F(t)$

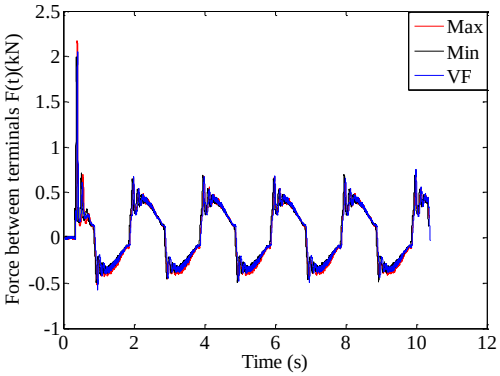

(*f*4)

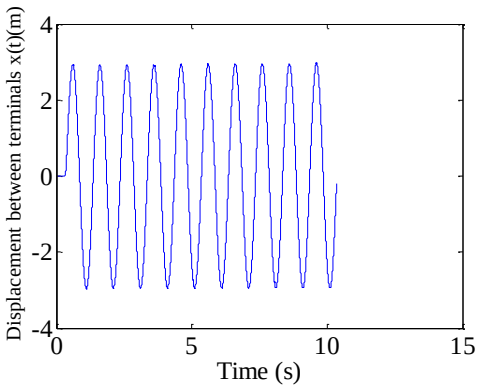

(*g*1) Excitation: $x(t)=0.003\sin(2\pi t)$

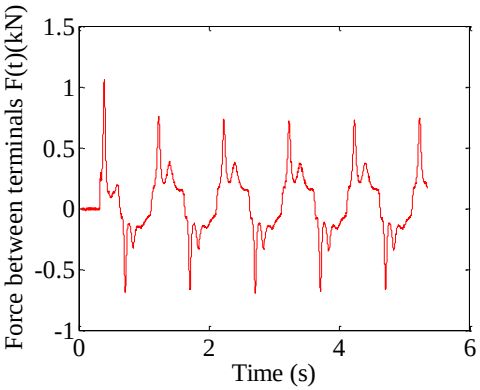

(*g*2) Force response of the VMI flywheel with the maximum MI: $F(t)$

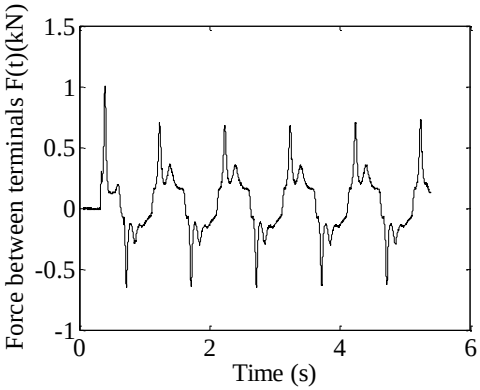

(*g*3) Force response of the VMI flywheel with the minimum MI: $F(t)$

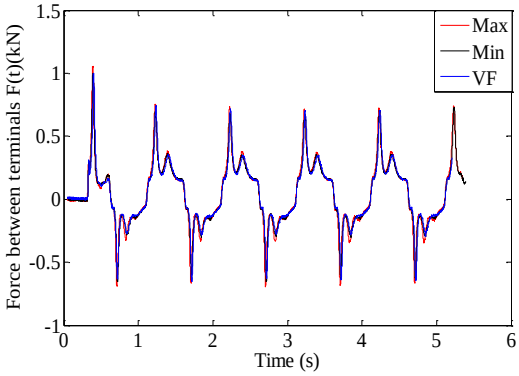

(*g*4)

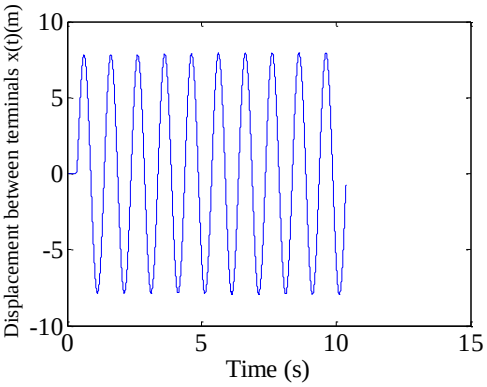

(*h*1) Excitation: $x(t)=0.008\sin(2\pi t)$

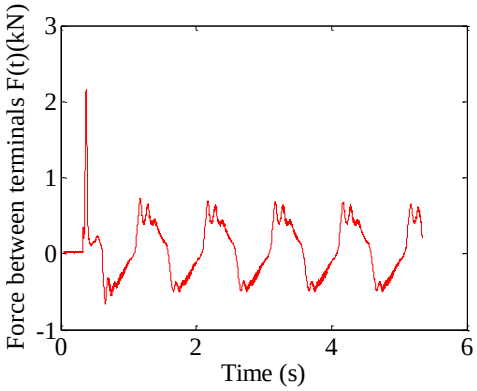

(*h*2) Force response of the VMI flywheel with the maximum MI: $F(t)$

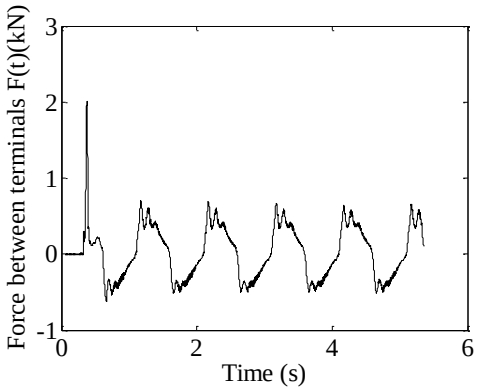

(*h*3) Force response of the VMI flywheel with the minimum MI: $F(t)$

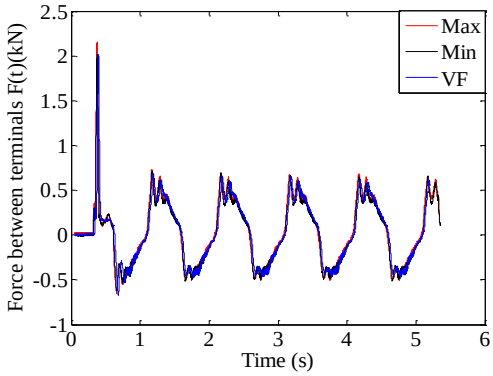

(*h*4)

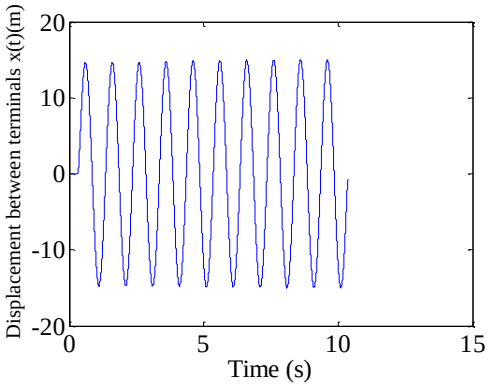

(*i*1) Excitation: $x(t)=0.015\sin(2\pi t)$

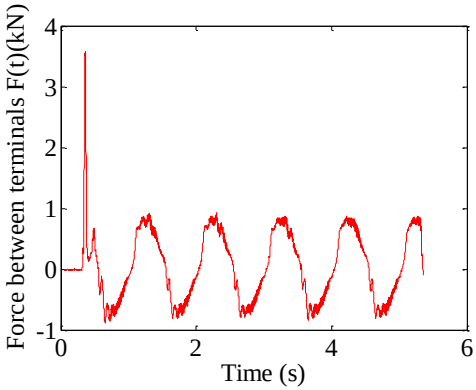

(*i*2) Force response of the VMI flywheel with the maximum MI: $F(t)$

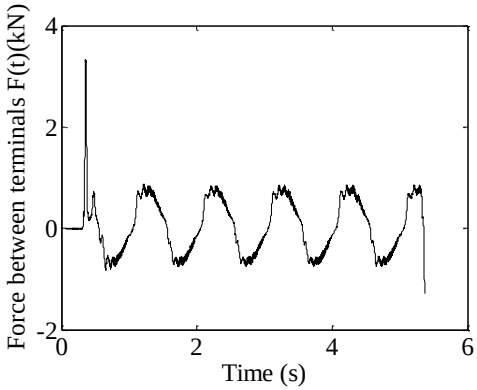

(*i*3) Force response of the VMI flywheel with the minimum MI: $F(t)$

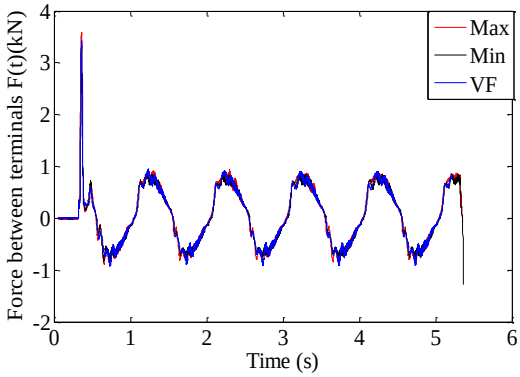

(*i*4)

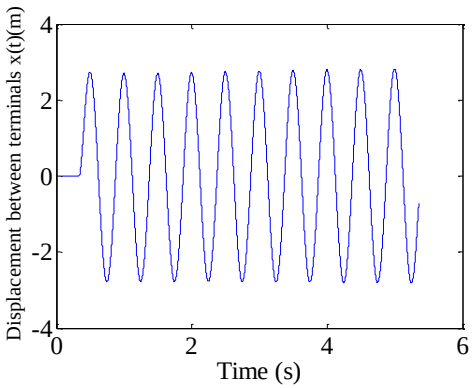

(*j*1) Excitation: $x(t)=0.003\sin(4\pi t)$

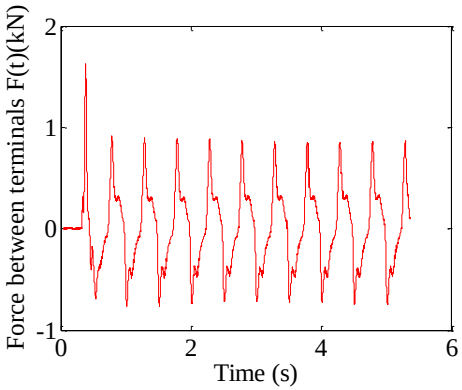

(*j*2) Force response of the VMI flywheel with the maximum MI: $F(t)$

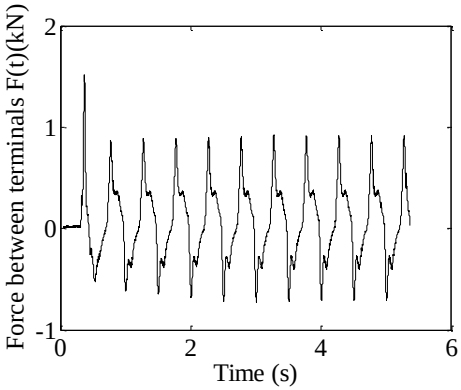

(*j*3) Force response of the VMI flywheel with the minimum MI: $F(t)$

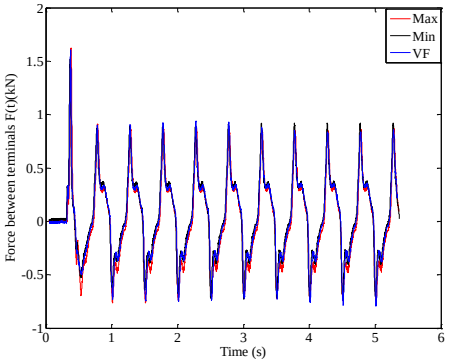

(*j*4)

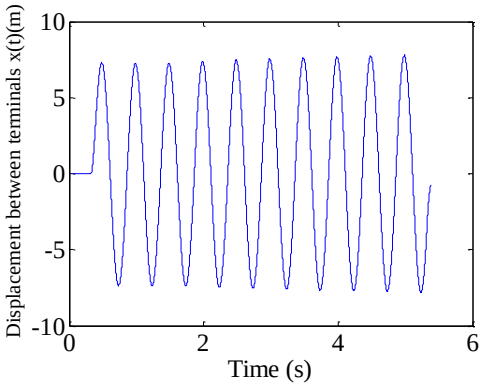

(*k*1) Excitation: $x(t)=0.008\sin(4\pi t)$

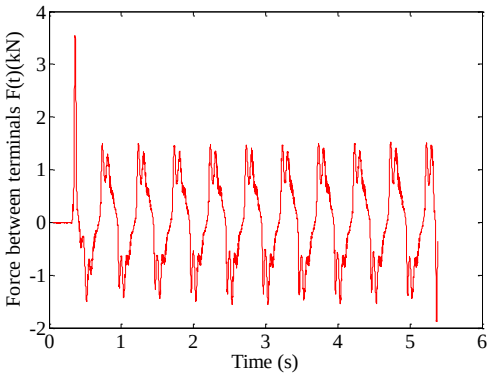

(*k*2) Force response of the VMI flywheel with the maximum MI: $F(t)$

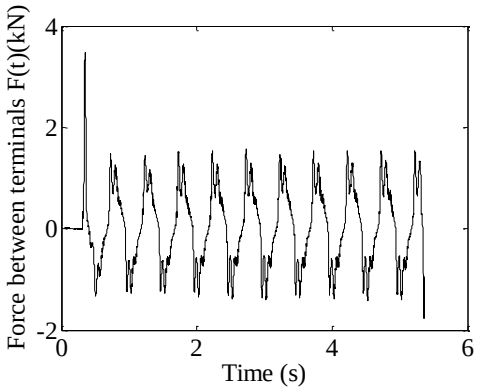

(*k*3) Force response of the VMI flywheel with the minimum MI: *F*(*t*)

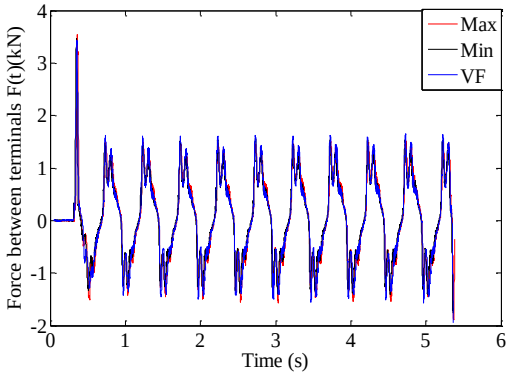

(*k*4)

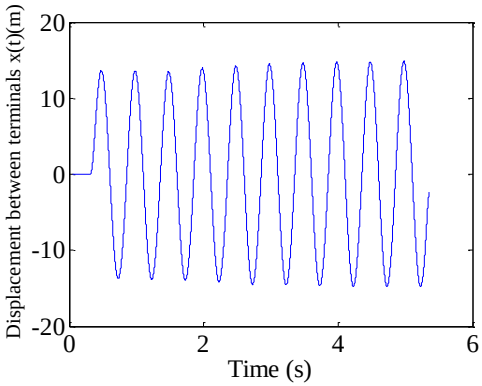

(*l*1) Excitation: $x(t)=0.015\sin(4\pi t)$

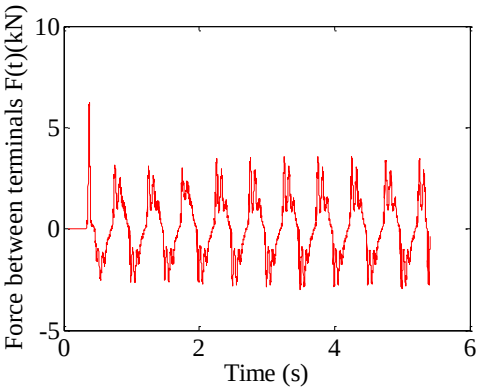

(*l*2) Force response of the VMI flywheel with the maximum MI: *F*(*t*)

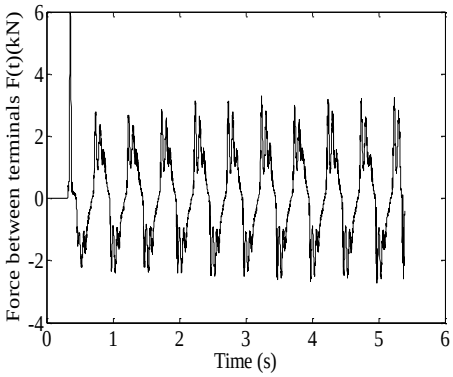

(*l*3) Force response of the VMI flywheel with the minimum MI: *F*(*t*)

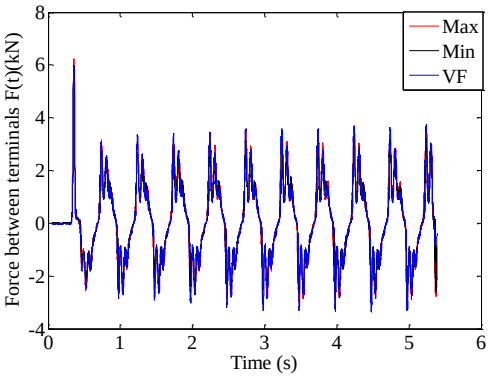

(*l*4)

Figure 4.13. Force responses of the system with the VMI flywheel, VMI flywheel with the maximum moment of inertia and VMI flywheel with the minimum moment of inertia:

*a*1, *b*1, *c*1, *d*1, *e*1, *f*1, *g*1, *h*1, *i*1, *j*1, *k*1, *l*1 are the displacement excitations, and *a*2, *b*2, *c*2, *d*2, *e*2, *f*2, *g*2, *h*2, *i*2, *j*2, *k*2, *l*2 are the associated force responses of the VMI flywheel with the maximum moment of inertia, *a*3, *b*3, *c*3, *d*3, *e*3, *f*3, *g*3, *h*3, *i*3, *j*3, *k*3, *l*3 are those of the VMI flywheel with the minimum moment of inertia, and *a*4, *b*4, *c*4, *d*4, *e*4, *f*4, *g*4, *h*4, *i*4, *j*4, *k*4, *l*4 plot the force responses of the VMI flywheel with variable moment of inertia together with those with maximum and minimum moment of inertia as plotted in *a*2-l2 and *a*3-l3. (Note: Max, Min and VF in Figures *a*4-l4 stand respectively for the VMI flywheel with the maximum, minimum and variable moments of inertia).

Since the maximum variation of the moment of inertia caused by the slider movement is only about 10% of the total moment of inertia of the VMI flywheel, the variation effect is not very pronounced in *a*4-l4 of Figure 4.13. Therefore, the close-up views of three important areas in one of these figures (*l*4 of Figure 4.13) are presented in Figure 4.14. The other figures in Figure 4.13 are almost identical.

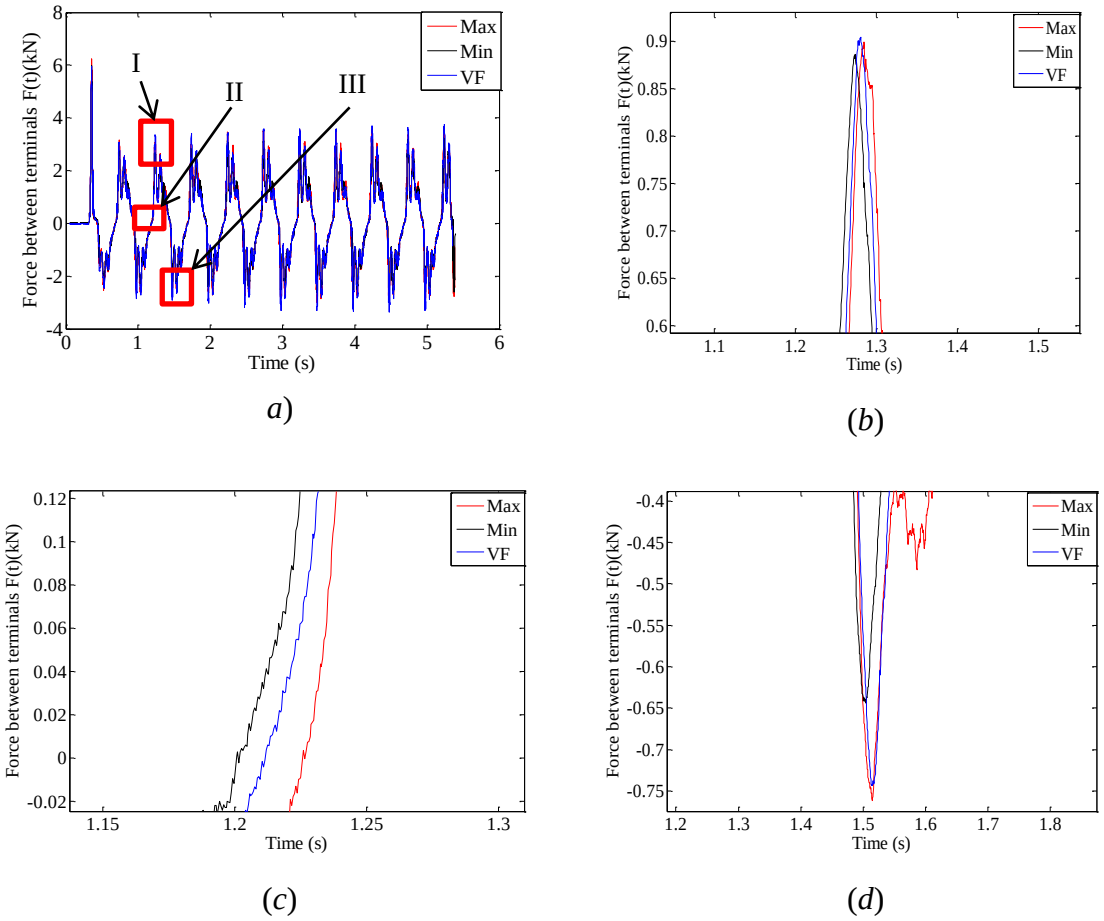

Figure 4.14. Enlarged views of Figure 4.13(*l*4): (*a*) original Figure 4.13 (*l*4) with the three marked zones of interest, (*b*)-(*d*) the close-up views of the peak (i.e., area I), zero-crossing (area II), and valley (area III) areas respectively.

In Figure 4.14, the red, black and blue curves are respectively associated with the forces resulting from the VMI flywheel with maximum, minimum and variable moments of inertia. As shown in Figure 4.14, the force response of the flywheel with variable moment of inertia is between those of VMI flywheel with the maximum and minimum moments of inertia in most of the time. This is expected. It is also observed that in some cases the blue curves are beyond the range of the red ones at the crest and valley locations. This could be caused by the backlash effect when the flywheel changes the rotary motion direction, rendering uncertainty in the force response curve.

System with the encoder

The main purpose of this set of tests, i.e., the system with the encoder without the flywheel, is to clearly show the backlash when the flywheel changes the rotational direction.

Figure 4.15 shows the excitations and force responses for the prototype with the encoder and the angular displacements of the encoder. For this group of tests, the force responses show the frictional resistance of the system without flywheel. It does not affect the comparisons between the VMI flywheel and VMI flywheel with the maximum moment of inertia and minimum moment of inertia. As such, only one test (the one with excitation: $x(t)=0.01\sin(0.4\pi t)$ in Table 4.5) is plotted in Figure 4.15.

It should be noted that, in Figure 4.15, the starting times of excitation and angular displacement response (recorded by the encoder) are not the same because they are recorded by two sets of software (recording software of the test machine for excitation, Labview in PC for the angular displacement response).

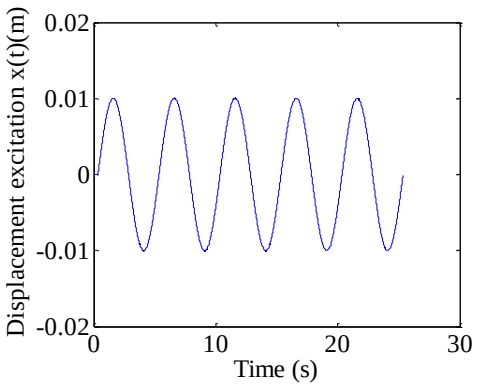

(*a*) Excitation: $x(t)=0.01\sin(0.4\pi t)$

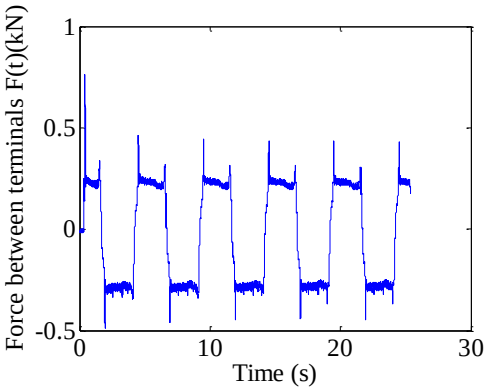

(*b*) Force $F(t)$

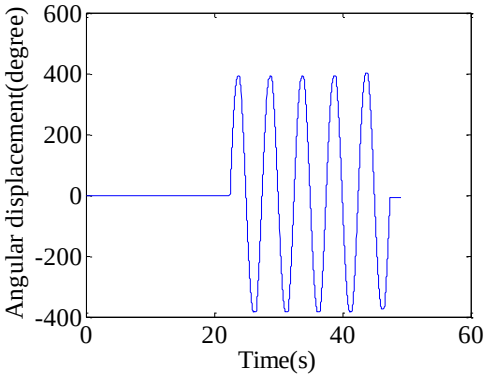

(*c*) Angular displacement $\theta(t)$

Figure 4.15. Response of the system with the VMI flywheel of the minimum moment of inertia: (*a*) excitation, (*b*) force response, and (*c*) angular displacement of the flywheel

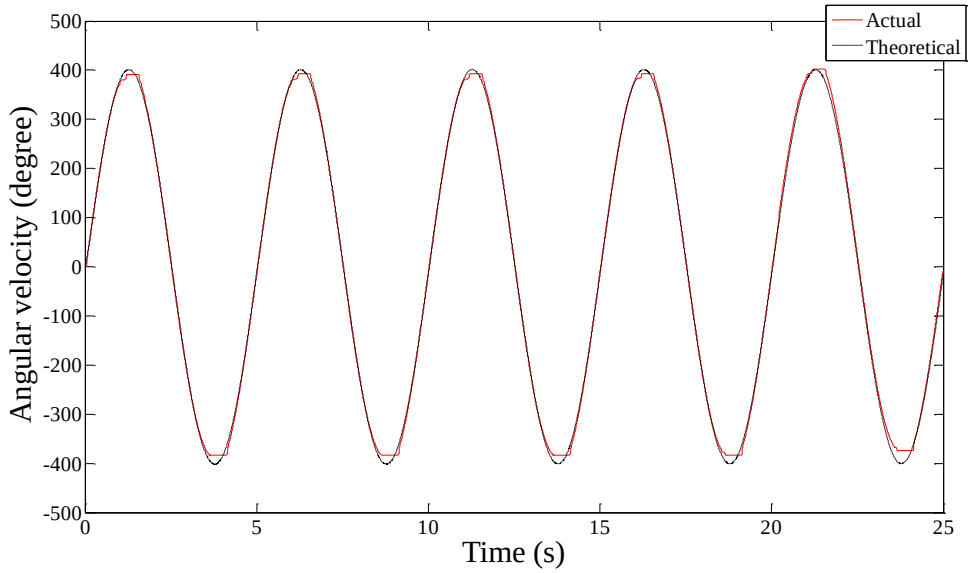

Figure 4.16. Comparison of the theoretical and the actual angular displacements

The actual and the theoretical angular displacements are shown in Figure 4.16. Because of the backlash, the actual angular displacement is different from the theoretical angular displacement when the flywheel changes the rotary direction.

4.3. Conclusion

From the experimental results, the following can be observed:

1. The performance of the VMI flywheel is between those of the VMI flywheel with the maximum moment of inertia and minimum moment of inertia. Therefore, the performance of the passive two-degree-of-freedom VMI suspension system in Chapter 3 should perform better than the CMI suspension in the cases of zero input and impulse excitations (Figures 4.13 and 4.14).

2. Backlash occurs when the flywheel changes the rotational direction. It leads to uncertain performance around this point. Though the backlash can be reduced but

can never be completely eliminated in any inertial mechanical system (Figure 4.16).

3. There is some frictional resistance in the system and hence the force responses are not zero even if the flywheel is not mounted (Figure 4.15).

Chapter 5.Conclusions and Future Research

5.1 Conclusion

The simulation results of the passive two-terminal variable moment of inertia hydraulic-flywheel vehicle suspension in Chapter 3 and the experimental results of one-degree-of-freedom prototype in Chapter 4 indicate:

1. For zero input and impulse input,
   a) The VMI suspension system outperforms the CMI suspension system in terms of all the three criteria, i.e., ride comfort, road handling and safety, and suspension deflection (Figures 3.15, 3.18, 3.22, 3.23, 3.25 and 3.26).
   b) The response time of the VMI suspension system is shorter than that of the CMI suspension system (Figures 3.14 and 3.17).

2. For three different excitations, the average vehicle body displacements of the VMI suspension system are all smaller than those of the CMI suspension system (Figures 3.14, 3.17 and 3.20).

3. For the sinusoidal excitation, the CMI system performs better than the VMI system in terms of ride comfort and suspension deflection, but falls short in terms of road handling and safety (Figures 3.21, 3.24 and 3.27).

4. The performance of the VMI flywheel is between those of the VMI flywheel with the maximum moment of inertia and minimum moment of inertia (Figures 4.13 and 4.14).

5. Backlash occurs when the flywheel changes the rotational direction. It leads to uncertain performance around this point. Though the backlash can be reduced but can never be completely eliminated in any inertial mechanical system (Figure 4.16).

5.2 Future Research

There are still some unsolved problems in the two-terminal mass area. Future research can be carried out in the following directions:

1. In this thesis, the designed suspension system is a passive non-linear system. The linearization for the system needs to be done in the future to obtain the analytic solution of the system. An active system may perform better than the passive system.

2. Backlash control is required even though backlashes cannot be eliminated in any inertial mechanical system. The backlashes may be reduced or even be exploited for industrial applications in the future.

References

Anderson, B.D.O., Vongpanitlerd, S., 1973, *Network Analysis and Synthesis: A Modern Systems Theory Approach*, (Englewood Cliffs: Prentice Hall).

Brune Otto., 1931, *Synthesis of a Finite Two-terminal Network Whose Driving-Point Impedance is a Prescribed Function of Frequency*, 1st, (Cambridge, America: Massachusetts Institute of Technology).

Chuan Li, Jiang Peng, Wang Shilong, Wang Yixian, and Jiao Zaojie, 2011, Design of Novel Hydraulic Flywheels for Vehicle Suspensions. *Advanced Science Letters*, **4**(4-5)**,** 1586 – 1590.

Darlington Sidney, 1984, A History of Network Synthesis and Filter Theory for Circuits Composed of Resistors, Inductors, and Capacitors. *IEEE Transaction on Circuits and Systems—I: Fundamental Theory and Applications*, **46**(1), 1-13.

Evangelou Simos, Limebeer J. N. David, Sharp Robin S., and Smith Malcolm C., 2006, Control of Motorcycle Steering Instabilities. *IEEE Control Systems Magzine*, **26**(5), 78-88.

Firestone Fred A., 1933, A New Analogy Between Mechanical and Electrical Systems. *Journal of Acoustical Society of America*, **4**(3), 249–267.

Fleury Gerared, and Mistrop Pierre, 2006, Numerical Assessment of Fore-and-aft

Suspension Performance to Reduce Whole-body Vibration of Wheel Loader Drivers. *Journal of Sound and Vibration*, **298**(3), 672 – 687.

Inman Daniel J., 2007, *Engineering vibration*, 3rd, (New Jersey: Prentice Hall).

International Standard, 1997, *Mechanical Vibration and Shock—Evaluation of Human Exposure to Whole-body Vibration.* 2nd, 2631-1.

Jiang Zheng, and Smith Malcolm C., 2011, Regular Positive-Real Functions and Five-Element Network Synthesis for Electrical and Mechanical Networks. *IEEE Transactions on Automatic Control*, **56**(6), 1275-1290.

Kuo Franklin F., 1962, *Network analysis and Synthesis*, 2nd, (Tokyo: Wiley Toppan).

Kuznetsov Alexey, Mammadov Musa, Sultan Ibrahim, Hajilarov Eledar, 2011, Optimization of Improved Suspension System with Inerter Device of the Quarter-car Model in Vibration Analysis. *Archives of Applied Mechanics*, **81**(10)**,** 1427-1437.

Li Chuan, Wang Shilong, Kang Ling, Lei Song, Yu Qibing, 2010, Two-Terminal Manipulation of Masses: Application to Vibration Isolation of Passive Suspensions. *Journal of Vibroengineering*, **12**(2), 143-255.

Li Chuan, and Liang Ming, 2011, Characterization and Modeling of a Novel Electro-hydraulic Variable Two-terminal Mass Device. *Smart Materials and Structures*, **20**(2), 025004.

Li Chuan, Liang Ming, and Yu Qibing, 2011, Multi-objective Optimization of Vehicle Passive Suspension with a Two-Terminal Mass Using Chebyshev Goal Programming. *World Academy of Science, Engineering and Technology*, **52**(126), 633-638.

Li Chuan, Liang Ming, Wang Yixian, and Dong Yutao, 2011, Vibration Suppression Using Two-terminal Flywheel Part I: Modeling and Characterization. *Journal of Vibration and Control accepted*, **18**(8), 1096-1105

Li Chuan, Liang Ming, Wang Yixian, and Dong Yutao, 2011, Vibration Suppression Using Two-terminal Flywheel Part II: Application to Vehicle Passive Suspension. *Journal of Vibration and Control accepted*, **18**(9), 1353-1365.

Li Chuan, Deng Juli, Wang Shilong, Zhang Xianming, and Dong Yutao, 2010, Electro-mechanical Analogy Design Theory of Spiral Flywheel Motion Transformation System. *Journal of Mechanical Engineering*, **46**(3), 103-108.

Micheal Z. Q., Chen, and Smith Malcolm C., 2008, Electrical and Mechanical Passive Network Synthesis. V.D. Blondel et al. (Eds.), *Recent Advances in Learning and Control* (London: Springer), 35-55.

Houghton Neil E., and Smith Malcolm C., 2009, Experimental Testing and Analysis of Inerter Devices. *Journal of Dynamic Systems, Measurement and Control*, **131**(1), 1-11.

Olson Harry Ferdinand, 1943, *Dynamical Analogies*, (New York: Van Nostrand).

Rivin E. I., 2003, *Passive Vibration Isolation*, (New York: ASME Press).

Scheibe Frank, and Smith Malcolm C., 2009, Analytical Solutions for Optimal Ride Comfort and Tyre Grip for Passive Vehicle Suspensions. *Vehicle System Dynamics*, **46(**10), 1229-1252.

Smith Malcolm C., 2002, Synthesis of mechanical networks: the inerter. *IEEE Transactions on Automatic Control*, **47**(10), 1648-1662.

Smith Malcolm C., and Smith G. W., 2000, Performance Limitations and Constraints for Active and Passive Suspensions: A Mechanical Multi-Port Approach. *Vehicle System Dynamics*, **33(**3), 137–168.

Smith Malcolm C., and Wang Fucheng, 2004, Performance Benefits in Passive Vehicle Suspensions Employing Inerters. *Vehicle System Dynamics*, **42**(4), 235–257.

Smith Malcolm C., 2003, The Inerter Concept and Its Application. *Proceedings of Society of Instrument and Control Engineers (SICE) Annual Conference*, Fukui, Japan, 1-40.

Smith Malcolm C., 2007, Achievable Dynamic Response for Automotive Active Suspensions, *International Journal of Vehicle Mechanics and Mobility*, **24**(1), 1-33.

Smith Malcolm C.: Force-controlling mechanical device, patent pending, International

Application. No.PCT/GB02/03056 (July 4, 2001).

Serway Raymond A., 1986. *Physics for Scientists and Engineers*, seconded, (Stamford America: Cengage Learning).

Willems Jan C., 2010, Ports and terminals. *Lecture Notes in Control and Information Scienc*es, **398**, 27-36.

Wing Omar, 2008, *Classical Circuit Theory,* (New York: Springer).

Yim S, Park Y and Yi K, 2010, Design of active suspension and electronic stability program for rollover prevention. *International Journal of Automotive Technology* **11**(2), 147 – 153.

Zhu S. J., Lou J. J., He Q. W. *et al*, 2006, *Vibration Theory and Isolation Technology,* (Beijing: National Defense Industry Press).

Zuo Lei, and Zhang Pengsheng, 2012, Energy Harvesting, Ride Comfort, and Road Handling of Regenerative Vehicle Suspensions. *ASME Journal of Vibration and Acoustics*, **135**(1), 14-22.